

Copyright  
by  
Xiaonan Chen  
2008

**The Dissertation Committee for Xiaonan Chen**  
**certifies that this is the approved version of the following dissertation:**

**Photonic Crystal-based Passive and Active Devices  
for Optical Communications**

**Committee:**

---

Ray T. Chen, Supervisor

---

Sanjay K. Banerjee

---

Jack C. Lee

---

Paul S. Ho

---

Shaochen Chen

**Photonic Crystal-based Passive and Active Devices  
for Optical Communications**

**by**

**Xiaonan Chen, B.E.; M.S.E.**

**Dissertation**

Presented to the Faculty of the Graduate School of

The University of Texas at Austin

in Partial Fulfillment

of the Requirements

for the Degree of

**Doctor of Philosophy**

**The University of Texas at Austin**

**August, 2008**

## **Dedication**

Dedicated to my parents

## **Acknowledgements**

I would like to thank my advisor, Dr. Ray T. Chen, for his continuous support and guidance in my doctoral study. I also thank my committee members, Dr. Sanjay K. Banerjee, Dr. Paul S. Ho, Dr. Jack C. Lee, and Dr. Shaochen Chen for serving on my dissertation committee and giving insightful advices on my dissertation research.

I appreciate the help from my fellow group members in the Optical Interconnect Group at University of Texas at Austin. They have been good friends and often provided valuable inputs and stimulating discussions into my doctoral research.

Finally, I would like to express my gratitude to my parents for unconditional support during my doctoral study.

Xiaonan Chen

University of Texas at Austin

August, 2008

# **Photonic Crystal-based Passive and Active Devices for Optical Communications**

Publication No. \_\_\_\_\_

Xiaonan Chen, Ph. D

The University of Texas at Austin, 2008

Supervisor: Ray T. Chen

With the progress of microfabrication and nanofabrication technologies, there has been a reawakened interest in the possibility of controlling the propagation of light in various materials periodically structured at a scale comparable to, or slightly smaller than the wavelength. We can now engineer materials with periodic structures to implement a great variety of optical phenomena. These include well known effects, such as dispersing a variety of wavelength to form a spectrum and diffracting light and controlling its propagation directions, to new ones such as prohibiting the propagation of light in certain directions at certain wavelengths and localizing light with defects in some artificially synthesized dielectric materials. Advances in this field have had tremendous impact on modern optical and photonic technologies. This doctoral research was aimed at investigating some of the physics and applications of periodic structures for building blocks of the optical communication and interconnection system.

Particular research emphasis was placed on the exploitation of innovative periodic structure-based optical and photonic devices featuring better functionality, higher performance, more compact size, and easier fabrication. Research topics extended from one-dimensional periodic-structure-based true-time delay module, to two-dimensional periodic-structure-based silicon photonic-crystal electro-optic modulators. This research was specifically targeted to seek novel and effective solutions to some long-standing technical problems, such as slow switching speed, large device size, and high power consumption of silicon optical modulators, among others. For each subtopic, research challenges were presented and followed by the proposed solutions with extensive theoretical analysis. The proposals were then verified by experimental implementations. Experimental results were carefully interpreted and the future improvements were also discussed.

## Table of Contents

List of Tables .....	x
List of Figures .....	xi
Chapter 1 <i>Introduction</i> .....	1
1.1 overview of 1-D photonic crystals – gratings .....	1
1.2 overview of 2-D and 3-D photonic crystals .....	2
1.3 the superprism and related phenomena in photonic crystals .....	6
1.4 the slow light effect in photonic crystal waveguides and its application in modulators .....	10
1.5 dissertation organization .....	13
Chapter 2 <i>Theoretical study of light propagation in photonic crystals</i> .....	18
2.1 introduction .....	18
2.2 a rigorous theory for solving general three-dimensional photonic crystal refraction problems .....	19
2.3 design on low-index-contrast superprism structure with efficient transmission mode .....	23
2.4 summary .....	32
Chapter 3 <i>Theoretical and experimental study of 1-D photonic crystals for         true-time-delay line applications</i> .....	35
3.1 introduction .....	35
3.2 wavelength dispersion in 1-D photonic crystals – hologram gratings .....	35
3.3 design on structure miniaturization and delay time enhancement .....	38
3.4 fabrication of the hologram module .....	42
3.5 characterization of the hologram module .....	45
3.6 demonstration of optimized hologram module in phase-array antenna system .....	49
3.7 summary .....	52
Chapter 4: <i>Silicon photonic crystal waveguide-based optical modulators</i> .....	55
4.1 introduction .....	55



4.2	brief review of photonic crystal waveguide modulators.....	56
4.3	brief review of diode- and capacitor-based silicon optical modulators ... .....	58
4.4	summary.....	61
Chapter 5: <i>High-speed capacitor-based photonic-crystal silicon electro-optic modulators</i> .....		64
5.1	research motivation.....	64
5.2	passive waveguide components: slot photonic crystal waveguide and mode converter.....	66
5.3	passive waveguide components: device fabrication and characterization .....	72
5.4	active waveguide components: device optical and electrical design ...	75
5.5	active waveguide components: device fabrication and characterization .....	80
5.6	summary.....	84
Chapter 6: <i>Potential applications</i> .....		88
6.1	introduction .....	88
6.2	slotted structure-based optical sensors.....	89
6.3	fabrication of slot photonic crystal waveguide-based optical sensors .... .....	93
6.4	simulation and characterization of waveguide sensitivity of slot photonic crystal waveguide.....	95
6.5	summary.....	98
Chapter 7: <i>Summary</i> .....		101
Bibliography .....		103
Vita .....		113

## **List of Tables**

Table 1.2.1: Direct analogies between electromagnetic wave in photonic crystals and electron in periodic potential.....	6
Table 3.6.1: Time delay requirement for microwave phased array antennas .....	49

## List of Figures

Figure 1.3.1: Superprism phenomena with wavelength sensitivity .....	7
Figure 1.3.2: Superprism phenomena with angular sensitivity.....	8
Figure 1.3.3: Supercollimator phenomena.....	9
Figure 1.3.4: Superlens phenomena.....	9
Figure 1.4.1: A schematic of a photonic crystal waveguide modulator.....	11
Figure 1.4.2: A typical dispersion diagram of a photonic crystal waveguide.....	11
Figure 1.4.3: A typical dispersion diagram of a homogeneous medium .....	12
Figure 2.2.1: A general schematic of a 3D PC structure .....	19
Figure 2.3.1: A schematic of a 3D square-rod structure .....	23
Figure 2.3.2: 3D dispersion surface of the lowest band for the square-rod structure with $a/\lambda = 0.40$ .....	24
Figure 2.3.3: Dispersion contours of all covered bands in $k_z = 0$ plane, normalized frequency $a/\lambda = 0.4$ .....	25
Figure 2.3.4: Dispersion contours in $k_z = 0$ plane, $a/\lambda = 0.35$ .....	26
Figure 2.3.5: Dispersion contours in $k_z = 0$ plane, $a/\lambda = 0.45$ .....	26
Figure 2.3.6: Magnified dispersion contour corner of the lowest band with different normalized frequency $a/\lambda = 0.35$ and $0.40$ .....	28
Figure 2.3.7: Dispersion contours with 20nm wavelength difference.....	29
Figure 2.3.8: Superprism effect at the lowest band of the three-dimensional square-rod photonic crystal.....	30
Figure 2.3.9: The refraction angle (solid curve) and normalized transmission (dotted curve) for a photonic crystal with polymer index changed by up to $10^{-3}$ .....	31
Figure 3.2.1: Vector diagram for Bragg regime diffraction.....	37

Figure 3.3.1: Symmetric structure of the wavelength-tuning hologram waveguide-based true-time delay modules, consisting of input and output collimators with single-mode fiber pigtails, input and output dispersive holographic grating couplers, right angle prism and glass waveguide strip. ....	38
Figure 3.3.2: 3-D symmetric structure of the wavelength-tuning hologram waveguide-based true-time delay modules. ....	39
Figure 3.3.3: A previously proposed structure, in which the final output position was not fixed, which made the coupling to a single-mode fiber much more difficult. ....	40
Figure 3.4.1: Setup for holographic recording: schematic and real setup .....	44
Figure 3.5.1: Block diagram for time delay (phase versus frequency) measurement and system demonstration. ....	46
Figure 3.5.2: Measured (points) and simulated (lines) results of RF phase versus RF frequency. ....	47
Figure 3.5.3: Measured (points) and simulated (lines) results of time delay versus incident wavelength compared with original structure. ....	47
Figure 3.5.4: Comparison of simulated beam scanning angle versus controlled time delay for X-band elements .....	48
Figure 3.5.5: Size comparison between new symmetric structure (left) and previous structure (right). ....	48
Figure 3.6.1: A 4-element sub-array antenna system. The insets show the symmetric hologram grating-based true-time delay module and a schematic of the antenna elements, respectively. ....	50
Figure 3.6.2: Measured and simulated radiation patterns at 18 GHz and 22 GHz with beam steering angle $\alpha = -45^\circ$ . ....	50
Figure 3.6.3: Measured and simulated radiation patterns at 18 GHz and 22 GHz with beam steering angle $\alpha = 0^\circ$ .....	51
Figure 3.6.4: Measured and simulated radiation patterns at 18 GHz and 22 GHz with beam steering angle $\alpha = +45^\circ$ . ....	51
Figure 3.6.5: Cascaded architecture of delay units for large array antennas. Each delay module provides the required delay difference $\Delta T_d$ for adjacent antenna elements .....	52

Figure 4.3.1: Electrical structure of a vertical MOS capacitor-embedded PCW Mach-Zehnder modulator .....	58
Figure 4.3.2: Electrical structure of a horizontal p-i-n diode-embedded PCW Mach-Zehnder modulator .....	59
Figure 5.1.1: Schematic cross section of the MOS capacitor based photonic crystal modulator in (a) vertical configuration, and (b) horizontal configuration.....	65
Figure 5.2.1: Line defect structure with a low-index center slot embedded in a photonic crystal slab .....	66
Figure 5.2.2: Band diagram for a slot photonic crystal waveguide. The thick dashed line is the light line.....	67
Figure 5.2.3: 3D profile of the transverse electric field amplitude of the quasi-TE mode in a slot photonic crystal waveguide .....	68
Figure 5.2.4: Comparison of 2D field amplitude contours between a slot PCW and a single-mode strip waveguide.....	69
Figure 5.2.5: Optimization of the mode overlapping integral between the slot PCW and the multimode section. ....	70
Figure 5.2.6: FDTD Simulation results: A series of $ E_x(x,y) $ profiles on the X-Y plane imaged at different Z positions.....	71
Figure 5.3.1: Top-view SEM picture of a slot PCW integrated with two multimode interference couplers.....	73
Figure 5.3.2: Cross-section views of the slot PCW before and after filling SOG .	73
Figure 5.3.3: Top panel: Enlarged portions of the photonic band structure for both guided and leaky modes. Bottom panel: transmission spectrum of the slot PCW of 320 $\mu$ m length with (solid) and without (dashed) coupling structures .....	74
Figure 5.4.1: Schematic diagrams: top and cross-sectional views of a lateral capacitor-embedded photonic crystal waveguide. ....	77
Figure 5.4.2: Calculated profiles of the hole carriers.....	78
Figure 5.4.3: Calculated profiles of the refractive index changes under different driving voltages.....	79

Figure 5.5.1: Images of the fabricated device. Microscopic image of a capacitor-embedded photonic crystal Mach-Zehnder interferometer, where colored overlays indicate the $p^-$ and $p^+$ regions .....	81
Figure 5.5.2: The setup of optical measurements .....	82
Figure 5.5.3: The optical intensity at the modulator output and the leakage current as a function of the static driving voltage .....	83
Figure 5.5.4: The normalized output optical intensities of the modulator working at 1.6 Gbit /s .....	84
Figure 6.2.1: Schematic diagram of a Mach-Zehnder interferometer with slot PCWs working as the active and reference arms .....	90
Figure 6.2.2: Schematic diagram of cross-sectional view of the active arm .....	90
Figure 6.2.3: Energy band diagram of the capacitor-embedded silicon slab layer .....	92
Figure 6.3.1: Scanning electron microscopy top view of the active region integrated with tapering mode couplers .....	94
Figure 6.3.2: Top view of the SOG-filled slot PCW after focused-ion-beam milling .....	94
Figure 6.4.1: The optical intensity at the output of the slot PCW-embedded interferometer as a function of the static driving voltage .....	95
Figure 6.4.2: The band diagram for a slot photonic crystal waveguide .....	96
Figure 6.4.3: Comparison of effective index change between silicon slot PCW and slotted strip waveguide .....	97

## Chapter 1 *Introduction*

### 1.1 OVERVIEW OF ONE DIMENSIONAL PHOTONIC CRYSTALS – GRATINGS

Dielectric gratings have been subject to extensive studies in the past due to their wide applications in holography, spectroscopy, lasers, and optoelectronics. [1–10] Numerous devices and systems have been conceived and built with dielectric gratings as essential functional parts. Among them, distributed-feedback lasers, optical spectrum analyzers, and wavelength division demultiplexers are wellknown examples. In many applications, one of the most essential performance characteristics of gratings is diffraction efficiency, which has been analyzed by numerous theoretical techniques. During the past two decades, layering approaches [2–6] have gained popularity in numerical modeling of dielectric gratings with arbitrary profiles. Generally, these approaches slice a surface-relief grating into a large number of thin layers, each of which can be considered uniform in the thickness direction. The electromagnetic fields on the front and back surfaces of each layer can be easily related by solving Maxwell's equations. The relation between the fields on the front and back surfaces is commonly expressed in certain matrix form, often called transfer matrices or  $T$  matrices. [6] Once the  $T$  matrices are calculated for each layer, one can, in principle, multiply the  $T$  matrices sequentially to obtain the overall transfer matrix that relates the front and back surfaces of the entire grating. Because it turned out that such multiplication resulted in numerical instability for a large number of layers, a number of alternative formulations, [3–6] including the  $R$ -matrix or  $S$ -matrix approaches as reviewed in Ref. 6, were later devised to overcome the instability issue. These advancements have greatly improved the accuracy and efficiency of calculating the diffraction efficiencies for dielectric gratings with arbitrary profiles.

## **1.2 OVERVIEW OF TWO DIMENSIONAL AND THREE DIMENSIONAL PHOTONIC CRYSTALS**

In recent years, photonic crystal research has further broadened our view of dielectric gratings by introducing the concept of photonic bands and bandgaps. Photonic crystals (PCs) are a new class of artificial optical materials composed of periodic dielectric structures with different permittivity and feature size on the order of optical wavelengths. Photonic crystals have unusual optical properties and promise to provide revolutionary solutions to the miniaturization of photonic devices.

Photonic crystals have the property of preventing light from propagating in certain directions with specified energies, creating a photonic band gap which is analogous to the electronic band gap in semiconductors. The photons are either allowed or non-allowed states of the lattice depending on their energy. The allowed states (or modes) supported by the periodic lattice in a photonic-crystal material are usually known as “Bloch modes,” whereas ranges of non-allowed states are designated as “photonic bandgaps.” To broadly generalize, a given wavelength of light incident on the lattice is thus either transmitted through the lattice or reflected, respectively [11].

Applications for PCs fall into two generic categories based on either the reflective or transmissive attributes of a photonic crystal. The first includes spectral filtering, micron-scale optical interconnects, and high-efficiency microcavity laser devices. All of these applications predominantly make use of the reflective properties of a photonic bandgap to either confine light within a microcavity or line-defect waveguide, or to provide back-reflection over a certain stop band. In a microcavity laser device, for example, light is generated within the gain material, radiating in all directions simultaneously. For this category of application it is desirable to ensure that the



properties of the bandgap are as isotropic as possible, thus helping to reduce the linewidth of the laser emission and to improve the spatial mode profile.

The second set of generic applications includes spatial beam steering, polarization control, and optical time delay. These require the transmission of light directly across the lattice, in which light must couple from the external environment (usually via an input waveguide) into guided Bloch modes that propagate within the PC. Because properties of guided modes in photonic crystals are described by dispersion relations, the greater the curvature, the stronger these effects become [12, 13].

In the past two decades, there has been a great deal of exciting progress in the area of PCs. The concept of PCs was introduced independently in 1987 by Sajeev John [14] and Eli Yablonovitch [15]. At that time, everything was to be proven in three-dimensional (3D) structure. The first structure which exhibited a genuine photonic band gap was the diamond structure predicted from theoretical calculations by Ho, Chan, and Soukoulis [16, 17]. Shortly after this discovery, the first experimental photonic crystal was fabricated by Yablonovitch et al. on a related structure at microwave frequencies [18]. Ho et al. proposed a new dielectric woodpile structure that has a full three-dimensional photonic band gap and which may lift some of the roadblocks towards fabricating crystals with higher frequency photonic band gaps [19]. Photonic crystals become increasingly popular after these successes. Large investigations of these novel structures toward optical frequencies started around 1995. However, the field of 3D PCs is still appearing as essentially academic to the telecommunication and optoelectronic community. Conversely, two-dimensional (2D) PCs have been easier to explore using existing planar technology. The subsequent years rapidly brought to light more complex structures of interest for telecommunications such as microcavities, waveguides, and their various combinations.

For different applications of photonic crystals, the choice of material composition, lattice periodicity and symmetry as well as the deliberate creation of defect structures embedded in PCs allows the control over the properties of this novel class of optical materials.

The fundamental equations of electromagnetic theory for PCs are Maxwell's equation. Time dependent Maxwell's equation in dielectric media can be written as [20, 21]

$$\begin{aligned}
\nabla \cdot \vec{H}(\vec{r}, t) &= 0 \\
\nabla \times \vec{H}(\vec{r}, t) - \epsilon(\vec{r}) \frac{\partial(\epsilon_0 \vec{E}(\vec{r}, t))}{\partial t} &= 0 \\
\nabla \cdot \epsilon \vec{E}(\vec{r}, t) &= 0 \\
\nabla \times \vec{E}(\vec{r}, t) - \frac{\partial(\mu_0 \vec{H}(\vec{r}, t))}{\partial t} &= 0
\end{aligned} \tag{1.2.1}$$

Where  $E$  and  $H$  are the electrical and magnetic fields,  $\epsilon$  is the permittivity,  $\mu$  is the permeability,  $t$  is the time, and  $r$  is the displacement to origin.

The time harmonic mode at the steady state is

$$\begin{aligned}
\vec{H}(\vec{r}, t) &= \vec{H}(\vec{r}) e^{-i\omega t} \\
\vec{E}(\vec{r}, t) &= \vec{E}(\vec{r}) e^{-i\omega t}
\end{aligned} \tag{1.2.2}$$

By substituting Eq. 1.2.2 to Eq. 1.2.1, we can obtain Maxwell equation for the steady state

$$\begin{aligned}
\nabla \times \vec{H}(\vec{r}) + i\omega(\epsilon(\vec{r})\epsilon_0 \vec{E}(\vec{r})) &= 0 \\
\nabla \times \vec{E}(\vec{r}) - i\omega(\mu_0 \vec{H}(\vec{r})) &= 0
\end{aligned} \tag{1.2.3}$$

By expressing the equation in magnetic field  $H$  only, we can get the full-vector wave equation [20, 21]

$$\vec{\nabla} \times \left( \frac{1}{\epsilon} \vec{\nabla} \times \vec{H} \right) = -\frac{\omega^2}{c^2} \vec{H} \tag{1.2.4}$$

Thus, the Maxwell's equation for the steady state can be expressed in terms of an eigenvalue equation, with eigenvalue  $(\omega/c)^2$ .

PCs correspond to a periodic function

$$\varepsilon(\vec{r}) = \varepsilon(\vec{r} + \vec{a}) \quad (1.2.5)$$

for some primitive lattice vector  $a$ . By employing Bloch theorem

$$\bar{H}(\vec{r}) = \exp(i\vec{k} \cdot \vec{r}) \bar{H}_{n,\vec{k}}(\vec{r}) \quad (1.2.6)$$

$$\bar{H}_{n,\vec{k}}(\vec{r} + \vec{R}) = \bar{H}_{n,\vec{k}}(\vec{r})$$

where  $\bar{H}_{n,\vec{k}}$  is the periodic envelope function, to Eq. 1.2.4, we can obtain a full-vector wave equation of Bloch envelope function  $\bar{H}_{n,\vec{k}}$  [20, 21]

$$(\vec{\nabla} + i\vec{k}) \times \frac{1}{\varepsilon} (\vec{\nabla} + i\vec{k}) \times \bar{H}_{n,\vec{k}} = -\frac{\omega_n(\vec{k})^2}{c^2} \bar{H}_{n,\vec{k}} \quad (1.2.7)$$

The eigensolutions are periodic functions of Bloch wavevector  $k$ . The solution at  $k$  is the same as the solution at  $k+G$ , where  $G$  is a *primitive reciprocal lattice vector* defined by  $R_i \cdot G_j = 2\pi\delta_{ij}$ . Owing to this periodicity, we only need to calculate the eigensolutions for  $k$  within the primitive cell of this reciprocal lattice. Generally we choose the first Brillouin zone, inequivalent wavevector closest to the  $k=0$ .

All of the equations described above for PCs are directly analogous to quantum mechanics that governs the properties of electrons, as shown in Table 1.1 [20]. The master eigenvalue equation of electromagnetic wave in PCs is analogy to *Schrödinger* equation of electron in periodic potential. The periodic dielectric material  $\varepsilon$  is analogy to periodic potential  $V$ . The magnetic field  $H$  is analogy to wave function  $\psi$ . The photonic bandgap  $\Delta\omega_g$  is analogy to electronic bandgap  $E_g$ . Also, both have Brillouin zone concept. Thus some simulation methods in solid state physics or semiconductor physics such as plane wave expansion method can be directly implemented into PCs with some modifications.

Electron in periodic potential	EM in periodic dielectric
$[-\frac{\nabla^2}{2m} + V]\psi = E\psi$	$\nabla \times (\frac{1}{\epsilon(\vec{r})} \nabla \times \vec{H}) = \frac{\omega^2}{c^2} \vec{H}$
$V(\vec{r}) = V(\vec{r} + \vec{a})$	$\frac{1}{\epsilon(\vec{r})} = \frac{1}{\epsilon(\vec{r} + \vec{a})}$
$\psi(\vec{r}, t) = \sum_E c_E \psi_E(\vec{r}) e^{iEt/\hbar}$	$H(\vec{r}, t) = \sum_\omega c_\omega H_\omega(\vec{r}) e^{i\omega t}$
$E_g$	$\Delta\omega_g$

Table 1.2.1: Direct analogies between electromagnetic wave in photonic crystals and electron in periodic potential. [20]

### 1.3 THE SUPERPRISM AND RELATED PHENOMENA

PCs attract much attention due to their possible application in light control devices using the photonic bandgap or dispersion characteristics. The strong dispersion effects were first investigated by Lin et al. [22], with the nonlinear frequency dependence of the phase velocity being the source of the large dispersion observed. This angular dispersion is particularly strong if the direction of the incident beam is chosen such that changes in the incident angle or wavelength of the incident beam cause strong variations in the group velocity of the refracted beam. This superprism effect was demonstrated by Kosaka et al. [23, 24] in their “autocloned” 3D silicon based PCs. Wu, et al. observed the superprism effects in 2D GaAs-based PCs [25]. And Lupu, et al. demonstrated the superprism in 2D silicon-on-insulator PCs [26]. All of these structures are based on large refractive index materials. For the low index polymer, J. Serbin, et al. demonstrated the superprism effects in the 3D polymer structure in 2006 [27]. It shows even in the absence of a complete photonic band gap, polymer PCs can possess highly anisotropic and wavelength-dependent dispersion properties.

Superprism effect can find potential applications for wavelength-division-multiplexing (WDM) and superlens. New functionality can be added to these devices by making them tunable. This can be achieved by modulation of the photonic crystal's band structure through electro-optic effects induced by external electric fields or through temperature-induced changes in the PC's refractive index.

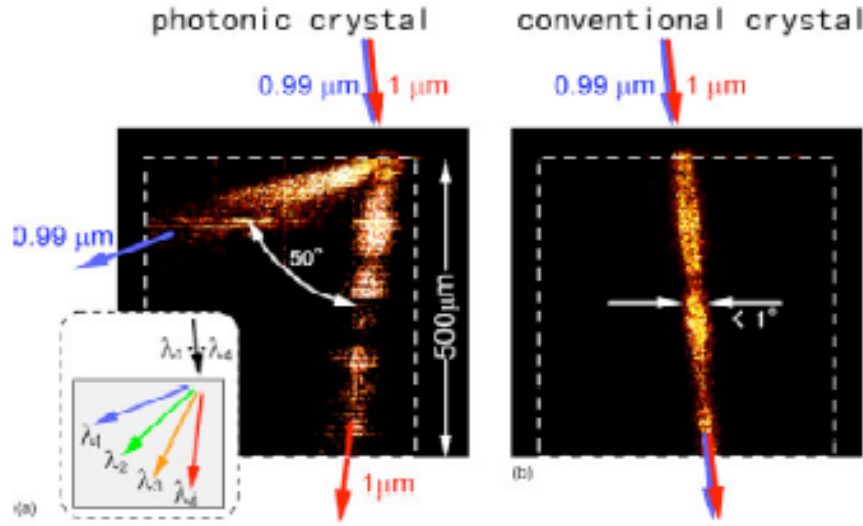


Fig. 1.3.1: Superprism phenomena with wavelength sensitivity. [23]

Prisms made of glass refract sunlight into the familiar rainbow colors. The distribution of this spectrum ranges widely with wavelengths of  $0.4 \mu\text{m}$  for blue to  $0.7 \mu\text{m}$  for red. Despite this wide distribution of wavelength, the dispersion angle obtained is only about  $10^\circ$ . Consequently, about  $0.1^\circ$  of the dispersion angle corresponds to 1% of the wavelength difference. This compares with the refraction behavior in PCs, as shown in Fig. 1.3.1. [23] Consider two light sources with wavelengths of  $0.99 \mu\text{m}$  and  $1 \mu\text{m}$ , which have a wavelength difference of about 1% [23]. When both are injected into a photonic crystal with the same incident angle equal to  $15^\circ$ , the color dispersion for every 1% of wavelength difference in this case is approximately  $50^\circ$ , so that the effective

dispersion is about 500 times that of ordinary optical prisms. For the  $0.99\text{ }\mu\text{m}$  wavelength light, even a  $\pm 7\%$  change of incident angle from the normal to the photonic crystal surface causes a  $\pm 70^\circ$  change of propagation angle, which is a 10 fold amplification of the incident angle shown in Figure 1.3.2 [24].

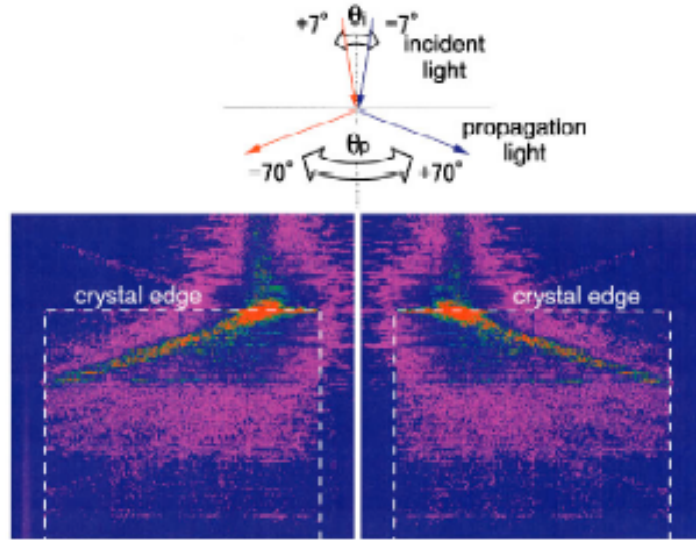


Fig. 1.3.2: Superprism phenomena with angular sensitivity. [24]

Consider a beam of light with a wavelength fixed at  $0.956\text{ }\mu\text{m}$ , a diameter of  $13\text{ }\mu\text{m}$  at the incident edge of the photonic crystal, and an angular divergence of  $6^\circ$ , as shown in Fig. 1.3.3. [25] When this light is incident to PC, the PC behaves like a collimator, because the light maintains its initial beam width for a long propagation distance of  $500\text{ }\mu\text{m}$  within the photonic crystal [25]. The propagation direction is maintained even under conditions of changing positions and incident angles by several degrees. Such an ideal fiber-like light collimator is never generated in ordinary linear crystals where nonlinearity effects like self-focusing are not produced.

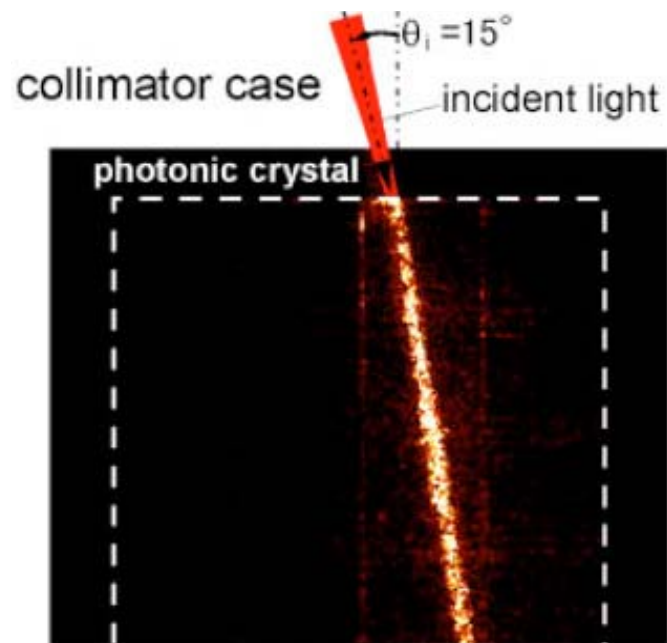


Fig. 1.3.3: Supercollimator phenomena. [25]

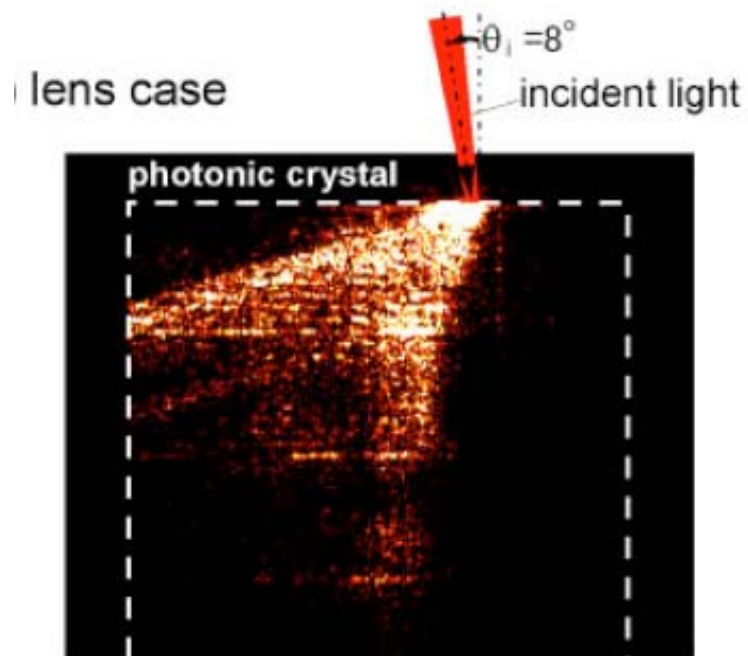


Fig. 1.3.4: Superlens phenomena. [25]

The effect shown in Figure 1.3.4 looks like placing a concave lens on the edge of the crystal. In this case, the incident wavelength and beam divergence angle are fixed at  $0.956\text{ }\mu\text{m}$  and  $6^\circ$ , respectively, and the incident angle is  $8^\circ$ . Under these conditions the condensed light beam with  $6^\circ$  divergence is transformed to a divergent light beam of  $70^\circ$  [25]. However, this lens effect does not depend on the position of the incident light. The numerical aperture (NA) of the light emitted out of the PC reproduces that of incident light, when the PC boundaries are aligned in parallel planes. In this case very thin beam expanders can be produced.

#### **1.4 THE SLOW LIGHT EFFECT IN PHOTONIC CRYSTAL WAVEGUIDES AND ITS APPLICATION IN MODULATORS**

The beginning of 21st century witnesses the pervasive presence of nanostructures and nanofabrication in science and technology. In photonics, nanostructures, particularly photonic crystals [26–43], hold the promise of achieving the same function in a significantly reduced device size with reduced power consumption (e.g. thresholdless lasers based on photonic crystal cavities). Optical waveguides based on photonic crystal line defects, the so-called photonic crystal waveguides (PCWs), have demonstrated the capability of slowing down the speed of light by up to one thousand times [28, 31]. Such a slow light device has a profound impact on the phase change over a segment of photonic crystal waveguide. When incorporated in silicon Mach-Zehnder modulators photonic crystal waveguides may, as first proposed by Soljacic et al. [33], significantly enhance the phase modulation efficiency and thus reduce the modulator electrode length by several orders of magnitude. A schematic of a photonic crystal waveguide modulator is depicted in Fig. 1.4.1.



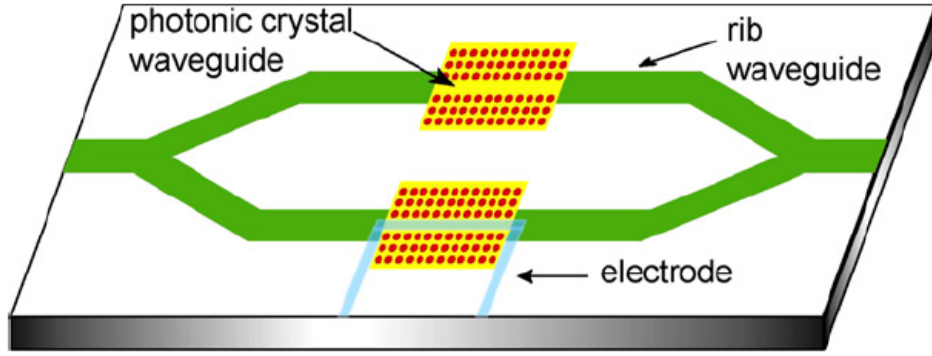


Fig. 1.4.1: A schematic of a photonic crystal waveguide modulator. [43]

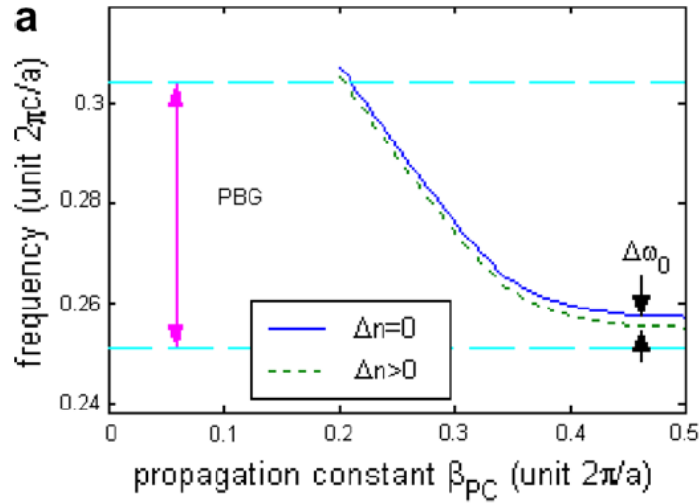


Fig. 1.4.2: A typical dispersion diagram of a photonic crystal waveguide. [36]

To illustrate this effect, consider a typical dispersion relation of a photonic crystal waveguide mode shown in Fig. 1.4.2 [36]. When the refractive index of core material changes slightly, the dispersion curve shifts vertically by an amount of  $\Delta\omega_0 \sim \omega(\Delta n/n)$ . Consider the effect for a fixed frequency (or, equivalently, a fixed wavelength). The change of propagation constant is related to the frequency shift through a factor inversely proportional to the group velocity,

$$\Delta\beta_{\text{PC}} = \Delta\omega_0/v_g, \quad (1.4.1)$$

The phase shift across a segment of PCW of length  $L$  can be expressed by  $\Delta\phi = \Delta\beta_{\text{PC}} \cdot L$ . Therefore, the interaction length required to obtain a  $\pi$  phase shift for a guided mode is

$$L \sim \frac{n}{2\Delta n} \frac{v_g}{c} \lambda_{\text{air}}, \quad (1.4.2)$$

where  $\lambda_{\text{air}}$  is the wavelength in air. Now it is evident that when the group velocity approaches zero near the band edge, the interaction length required to achieve a given phase shift can be reduced significantly.

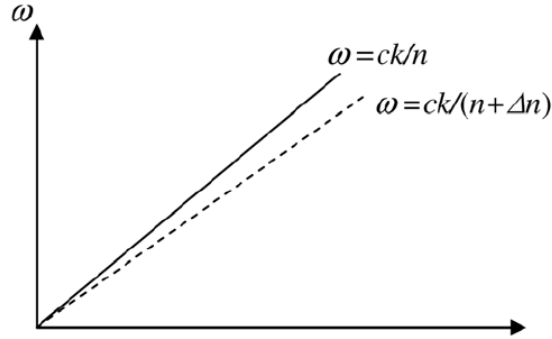


Fig. 1.4.3: A typical dispersion diagram of a homogeneous medium. [43]

To further understand why the change of wavevector (or propagation constant) is not simply  $\Delta k = k_0 \Delta n$  as in a homogeneous medium, we examine the dispersion curvature of a homogeneous medium shown in Fig. 1.4.3. A change of refractive index causes the linear dispersion relation to change its slope, pivoting around the origin of the  $\omega$ - $k$  diagram. For a photonic crystal waveguide, the periodicity of the dispersion relation  $\omega(\beta_{\text{PC}} + 2\pi/a) = \omega(\beta_{\text{PC}})$ , and usual inversion/mirror symmetry along the waveguide axis ensure an extremum (maximum or minimum) of  $\omega(\beta_{\text{PC}})$  at  $\beta_{\text{PC}} = \pi/a$ , where  $v_g = \omega'(\beta_{\text{PC}}) = 0$ . Upon a perturbation of the refractive index, this extremum must stay

at  $\beta_{\text{PC}} = \pi/a$ . Under such a condition, the dispersion curve only has the freedom of shifting vertically and/or changes its “effective mass” (using the terminology of the semiconductor energy bands). The change of the “effective mass” is usually negligible for a small perturbation of the refractive index. Therefore, the change of  $\beta_{\text{PC}}$  is mainly due to the vertical shift of the dispersion curve. A more intuitive interpretation is that light travels slower in a PCW and has more time to interact with electrons. This results in enhanced light-matter interaction and allows for the shrinkage of the interaction length.

## 1.5 DISSERTATION ORGANIZATION

This dissertation is arranged as follows. Chapter 1 gives an introduction of the fundamentals, including physics, theory and applications, of one-dimensional and two dimensional periodic optical structures. Chapter 2 reports our theoretical study of light propagation in photonic crystals. A rigorous theory for solving general three-dimensional photonic crystal refraction problems and the detailed design procedure on low-index-contrast superprism structure are presented. Chapter 3 describes our theoretical and experimental study of 1-D photonic crystals for true-time-delay line applications. Integration of the optimized hologram module in a phase-array antenna system is also presented. Chapter 4 briefly reviews the silicon photonic crystal waveguide-based optical modulators and their advantages. Chapter 5 is focused on the demonstration of a high-speed capacitor-based photonic-crystal silicon electro-optic modulator. A novel lateral capacitor-embedded device structure along with a compact mode coupler to solve the mode mismatch between silicon strip waveguide and slot photonic crystal waveguide is demonstrated. Extensive simulations and experimental implementations are discussed as well. Chapter 6 describes the potential applications of slot photonic crystal waveguides. The benefits and challenges of slot photonic crystal waveguides for sensing applications are presented. Chapter 7 summarizes the entire dissertation.

*Reference:*

- [1] H. Kogelnik, "Coupled wave theory for thick hologram gratings," *Bell Syst. Tech. J.* **48**, 2909–2947 (1969).
- [2] M. G. Moharam and T. K. Gaylord, "Diffraction analysis of dielectric surface-relief gratings," *J. Opt. Soc. Am.* **72**, 1385–1392 (1982).
- [3] L. Li, "Multilayer modal method for diffraction gratings of arbitrary profile, depth, and permittivity," *J. Opt. Soc. Am. A* **10**, 2581–2591 (1993).
- [4] N. Chateau and J. P. Hugonin, "Algorithm for the rigorous coupled-wave analysis of grating diffraction," *J. Opt. Soc. Am. A* **11**, 1321–1331 (1994).
- [5] M. G. Moharam, D. A. Pommet, E. B. Grann, and T. K. Gaylord, "Stable implementation of the rigorous coupledwave analysis for surface-relief gratings: enhanced transmittance matrix approach," *J. Opt. Soc. Am. A* **12**, 1077–1086 (1995).
- [6] L. Li, "Formulation and comparison of two recursive matrix algorithms for modeling layered diffraction gratings," *J. Opt. Soc. Am. A* **13**, 1024–1035 (1996).
- [7] R. T. Chen, H. Lu, D. Robinson, and T. Jannson, "Highly multiplexed graded-index polymer waveguide hologram for near-infrared eight-channel wavelength division demultiplexing," *Appl. Phys. Lett.* **59**, 1144–1146 (1991).
- [8] M. R. Wang, G. J. Sonek, R. T. Chen, and T. Jannson, "Large fanout optical interconnects using thick holographic gratings and substrate wave propagation," *Appl. Opt.* **31**, 236–249 (1992).
- [9] L. Gu, X. Chen, Z. Shi, B. Howley, J. Liu, and R. T. Chen, "Bandwidth-enhanced volume grating for dense wavelength-division multiplexer using a phasecompensation scheme," *Appl. Phys. Lett.* **86**, 181103 (2005).
- [10] L. Gu, X. Chen, W. Jiang, and R. T. Chen, "A solution to the fringing-field effect in liquid crystal based high-resolution switchable gratings," *Appl. Phys. Lett.* **87**, 201106 (2005).
- [11] M. Charlton, J. Lincoln, G. Flinn, "Planar photonic crystals move toward wider use", *Laser Focus World* June, 2005.
- [12] R. B. Wehrspohn, "Applications of silicon-based photonic crystals", 2nd IEEE International Conference on Group IV Photonics, 39 (2005).
- [13] H. Benisty, J. M. Lourtioz, A. Chelnokov, S. Combrie, X. Checoury, "Recent advances toward optical devices in semiconductor-based photonic crystals", *Proceedings of the IEEE*, 94, 5, 997 (2006).
- [14] S. John, "Strong localization of photons in certain disordered dielectric superlattices", *Phys. Rev. Lett.* **58**, 2486 (1987).

- [15] E. Yablonovitch, "Inhibited Spontaneous Emission in Solid-State Physics and Electronics", *Phys. Rev. Lett.*, 58, 2059 (1987).
- [16] K. M. Ho, C. T. Chan, and C. M. Soukoulis, "Existence of a photonic gap in periodic dielectric structures", *Phys. Rev. Lett.* 65, 3152 (1990).
- [17] C. T. Chan, K. M. Ho and C. M. Soukoulis, "Photonic band gaps in experimentally realizable periodic dielectric structures", *Europhys. Lett.* 16, 563 (1991).
- [18] E. Yablonovitch, T. J. Gmitter, and K. M. Lung, "Photonic band structure: The face-centered-cubic case employing nonspherical atoms", *Phys. Rev. Lett.* 67, 2295 (1991).
- [19] K. M. Ho, C. T. Chan, C. M. Soukoulis, R. Biswas, and M. Sigalas, "Photonic band gaps in three dimensions: New layer-by-layer periodic structures", *Solid State Communications*, 89, 5, 413 (1994).
- [20] J.D. Joannopoulos, R.D. Meade, J.N. Winn, *Photonic Crystals*, Princeton University Press, (1995) .
- [21] S. G. Johnson, J. D. Joannopoulos, *Photonic crystals: road from theory to practice*, Kluwer Academic Publishers, (2002).
- [22] S. Y. Lin, V. M. Hietala, L. Wang, and E. D. Jones, "Highly dispersive photonic band-gap prism", *Opt. Lett.* 21 1771 (1996).
- [23] H. Kosaka, T. Kawashima, A. Tomita, M. Notomi, T. Tamamura, T. Sato, and S. Kawakami, "Superprism phenomena in photonic crystals: toward microscale lightwave circuits", *IEEE J. Lightwave Tech.*, 17, 11, 2032 (1999).
- [24] H. Kosaka, T. Kawashima, A. Tomita, M. Notomi, T. Tamamura, T. Sato, and S. Kawakami, "Superprism phenomena in photonic crystals:", *Phys. Rev. B* 58, 16, R10096 (1998).
- [25] H. Kosaka, T. Kawashima, A. Tomita, M. Notomi, T. Tamamura, T. Sato, and S. Kawakami, "Self-collimating phenomena in photonic crystals", *Appl. Physics. Lett.*, 74, 9, 1212 (1999).
- [26] Ogawa S, Imada M, Yoshimoto S, Okano M, Noda S. *Science* 305, 227, (2004).
- [27] Park HG, Kim SH, Kwon SH, Ju YG, Yang JK, Baek JH, et al. "Electrically driven single-cell photonic crystal laser", *Science*, 305, 1444–7, (2004).
- [28] Notomi M, Yamada K, Shinya A, Takahashi J, Takahashi C, Yokohama I. "Extremely large group-velocity dispersion of linedefect waveguides in photonic crystal slabs", *Phys Rev Lett*, 87, 253902, (2001).

- [29] Jiang W, Chen RT. "Multichannel optical add-drop process in symmetrical waveguide-resonator systems", *Phys Rev Lett* 91, 213901, (2003).
- [30] Jiang W, Chen RT, Lu X. "Theory of light refraction at the surface of a photonic crystal", *Phys Rev B* 71, 245115, (2005).
- [31] Gersen H, Karle TJ, Engelen RJP, Bogaerts W, Korterik JP, Van Hulst NF, et al. "Real-space observation of ultraslow light in photonic crystal waveguides", *Phys Rev Lett*, 94, 073903, (2005).
- [32] Shih MH, Kim WJ, Kuang W, Cao JR, Yukawa H, Choi SJ, et al. "Two-dimensional photonic crystal Mach-Zehnder interferometers", *Appl Phys Lett*, 84, 460, (2004).
- [33] Soljacic M, Johnson SG, Fan S, Ibanescu M, Ippen E, Joannopoulos JD. Photonic-crystal slow-light enhancement of nonlinear phase sensitivity. *J Opt Soc Am B*, 19, 2052–9, (2002).
- [34] Camargo EA, Chong HMH, De La Rue RM. "2D photonic crystal thermo-optic switch based on AlGaAs/GaAs epitaxial structure", *Opt Express*, 12, 588, (2004).
- [35] Vlasov YA, O'Boyle M, Hamann HF, McNab SJ. "Active control of slow light on a chip with photonic crystal waveguides", *Nature*, 438, 65–9, (2005).
- [36] Jiang Y, Jiang W, Gu L, Chen X, Chen RT. "80-Micron interaction length silicon photonic crystal waveguide modulator", *Appl Phys Lett*, 87, 221105, (2005).
- [37] Chu T, Yamada H, Ishida S, Arakawa Y. "Thermooptic switch based on photonic-crystal line-defect waveguides", *IEEE Photon Technol Lett*, 17 (10), 2083–5, (2005).
- [38] Notomi M, Shinya A, Mitsugi S, Kuramochi E, Ryu HY. "Waveguides, resonators and their coupled elements in photonic crystal slabs", *Opt Express*, 12, 1551–61, (2004).
- [39] Weiss SM, Ouyang H, Zhang J, Fauchet PM. "Electrical and thermal modulation of silicon photonic bandgap microcavities containing liquid crystals", *Opt Express*, 13 (4), 1090, (2005).
- [40] Gu L, Jiang Y, Jiang W, Chen X, Chen RT. "Silicon-on-insulatorbased photonic-crystal Mach-Zehnder interferometers", *Proc SPIE*, 6128, 261–8, (2006).
- [41] Gu L, Jiang W, Chen X, Wang L, Chen RT. "High-speed silicon photonic crystal waveguide modulator for low-voltage operation", *Appl Phys Lett*, 90, 071105, (2007).

- [42] Gu L, Jiang W, Chen X, Chen RT. "Photonic crystal waveguide based silicon-on-insulator thermo-optic Mach Zehnder interferometers", IEEE Photon Technol Lett, 19, 342, (2007).
- [43] W. Jiang, L. Gu, X. Chen, R. T. Chen, "Photonic Crystal Waveguide Modulators for Silicon Photonics: Device Physics and Some Recent Progress," Solid State Electronics, 51, 1278 (2007).

## **Chapter 2: *Theoretical study of light propagation in photonic crystals***

### **2.1 INTRODUCTION**

Anomalous light refraction, or the superprism effect, has been experimentally demonstrated in three-dimensional (3D) photonic crystal (PC) structures, which are fabricated through self-organization method. [1] Proposed applications for the superprism effect include wavelength demultiplexing, [1] 3D integrated photonics circuits based on self-collimation propagation, [2] sensing and filtering, [3] and 3D functional superlenses based on subwavelength imaging. [4] The refraction angle and transmission intensity of each propagating mode inside the PC are two intrinsic optical properties we must investigate before fabrication. A powerful physical concept for studying light beam directions is the PC dispersion surface, which is commonly calculated using conventional plane wave expansion (PWE) method. [5] For the transmission, the popular finite-difference time-domain (FDTD) technique is often time consuming, particularly for large-volume 3D structure simulations. Li and Ho introduced a PWE-based transfer-matrix method (TMM) to study the transmitted field amplitude through a single photonic crystal surface. [6] Jiang et al. developed the first rigorous theory to analyze light refraction and transmission by a 2D photonic crystal having a general lattice-type and an arbitrary surface orientation that includes both an ordinary Miller-indexed surface and a quasi-periodic surface. [7] However, a general PC refraction theory that can efficiently and reliably predict transmission and reflectivity for light refraction in 3D photonic crystals is rarely seen in the literature. In this chapter we present a full-vectorial refraction theory for electromagnetic (EM) wave propagation in semi-infinite 3D PC structures in Sec 2.2. Furthermore, we discuss in detail how to employ our theory to



design and simulate a 3D PC superprism structure with efficient transmission modes in Sec 2.3.

## 2.2 A RIGOROUS THEORY FOR SOLVING GENERAL THREE-DIMENSIONAL PHOTONIC CRYSTAL REFRACTION PROBLEMS

A general schematic of a 3D PC structure is depicted in Fig. 2.2.1, a unit cell with PC dielectric function  $\varepsilon(\mathbf{x})$  replicates periodically along three independent directions  $\mathbf{a}_1$ ,  $\mathbf{a}_2$  and  $\mathbf{a}_3$ . A planar wave  $e^{i\mathbf{k}_0\mathbf{x}}$  with frequency  $\omega$  is incident upon the interface, defined as  $x-z$  plane, between a uniform medium and a PC region. For convenience, we sometimes refer to the uniform medium region ( $y < 0$ ) as region I and the PC region ( $y > 0$ ) as region II. Consider the equivalent transform of Maxwell equations

$$\begin{cases} i\omega\mu_0\mathbf{H} = \nabla \times \mathbf{E} \\ -i\omega\varepsilon_0\varepsilon(\mathbf{x})\mathbf{E} = \nabla \times \mathbf{H} \end{cases} \quad (2.2.1)$$

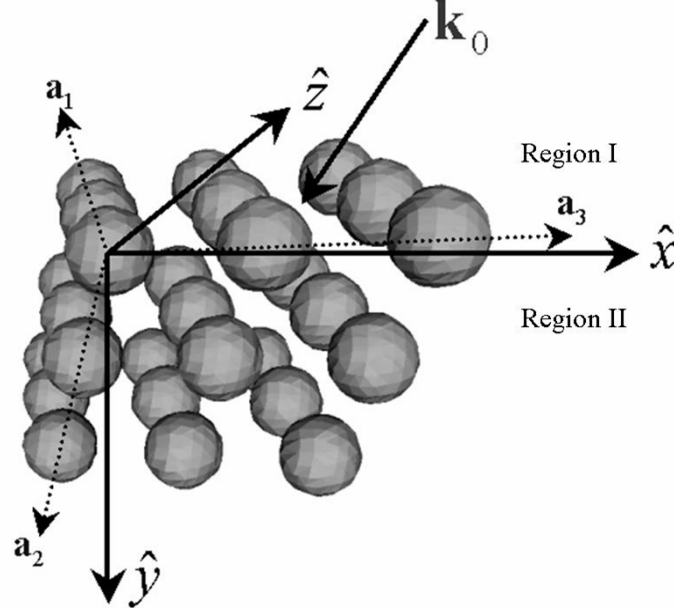


Fig. 2.2.1: A general schematic of a 3D PC structure. [8]

By substitution for  $E_y$  and  $H_y$ , we may obtain the linear equations with reduced field variables

$$\begin{cases} \omega^2 \mu_0 \varepsilon_0 \begin{bmatrix} H_x \\ H_z \end{bmatrix} = i\omega \varepsilon_0 \frac{\partial}{\partial y} \begin{bmatrix} -E_z \\ E_x \end{bmatrix} + \begin{bmatrix} -\partial/\partial z \\ \partial/\partial x \end{bmatrix} \left[ \frac{1}{\varepsilon(\mathbf{x})} \left( \frac{\partial H_x}{\partial z} - \frac{\partial H_z}{\partial x} \right) \right] \\ \omega^2 \mu_0 \varepsilon_0 \begin{bmatrix} E_x \\ E_z \end{bmatrix} = \frac{i\omega \mu_0}{\varepsilon(\mathbf{x})} \frac{\partial}{\partial y} \begin{bmatrix} H_z \\ -H_x \end{bmatrix} + \frac{1}{\varepsilon(\mathbf{x})} \begin{bmatrix} -\partial/\partial z \\ \partial/\partial x \end{bmatrix} \left( \frac{\partial E_x}{\partial z} - \frac{\partial E_z}{\partial x} \right) \end{cases} \quad (2.2.2)$$

In the PC region, the field equations may be expressed with a Fourier expansion in terms of Fourier coefficients

$$\begin{aligned} \omega^2 \mu_0 \varepsilon_0 H_x(\mathbf{G}) &= \omega \varepsilon_0 (k_y + G_y) E_z(\mathbf{G}) \\ &+ \sum_{\mathbf{G}_1} (k_z + G_z) \eta(\mathbf{G} - \mathbf{G}_1) [(k_z + G_{1z}) H_x(\mathbf{G}_1) - (k_x + G_{1x}) H_z(\mathbf{G}_1)] \\ \omega^2 \mu_0 \varepsilon_0 H_z(\mathbf{G}) &= -\omega \varepsilon_0 (k_y + G_y) E_x(\mathbf{G}) \\ &- \sum_{\mathbf{G}_1} (k_x + G_x) \eta(\mathbf{G} - \mathbf{G}_1) [(k_z + G_{1z}) H_x(\mathbf{G}_1) - (k_x + G_{1x}) H_z(\mathbf{G}_1)] \\ \omega^2 \mu_0 \varepsilon_0 E_x(\mathbf{G}) &= -\omega \mu_0 \sum_{\mathbf{G}_1} (k_y + G_{1y}) \eta(\mathbf{G} - \mathbf{G}_1) H_z(\mathbf{G}_1) \\ &+ \sum_{\mathbf{G}_1} (k_z + G_{1z}) \eta(\mathbf{G} - \mathbf{G}_1) [(k_z + G_{1z}) E_x(\mathbf{G}_1) - (k_x + G_{1x}) E_z(\mathbf{G}_1)] \\ \omega^2 \mu_0 \varepsilon_0 E_z(\mathbf{G}) &= \omega \mu_0 \sum_{\mathbf{G}_1} (k_y + G_{1y}) \eta(\mathbf{G} - \mathbf{G}_1) H_x(\mathbf{G}_1) \\ &- \sum_{\mathbf{G}_1} (k_x + G_{1x}) \eta(\mathbf{G} - \mathbf{G}_1) [(k_z + G_{1z}) E_x(\mathbf{G}_1) - (k_x + G_{1x}) E_z(\mathbf{G}_1)] \end{aligned} \quad (2.2.3)$$

where  $\mathbf{G}$  is a reciprocal lattice vector, given by  $\mathbf{G}_{lmn} = l\mathbf{b}_1 + m\mathbf{b}_2 + n\mathbf{b}_3$ ,  $-L \leq l \leq L$ ,  $-M \leq m \leq M$ ,  $-N \leq n \leq N$ . Here  $L$ ,  $M$ , and  $N$  denote the truncations of the Fourier series in three dimensions.  $\mathbf{b}_1$ ,  $\mathbf{b}_2$  and  $\mathbf{b}_3$  are the basis vectors of the reciprocal lattice. For a semi-infinite PC structure with a periodic surface, a set of “primitive” translation vectors can always be chosen to keep  $\mathbf{b}_2$  along the  $\hat{y}$  axis if the

surface is periodic. [7, 8] The Fourier coefficient  $\eta_{\mathbf{G}} = V^{-1} \int_{cell} d^3\mathbf{x} \cdot e^{-i\mathbf{G}\cdot\mathbf{x}} \varepsilon^{-1}(\mathbf{x})$ , where  $V$  is the volume of a unit cell.  $E(\mathbf{G})$  and  $H(\mathbf{G})$  are the Fourier coefficients of electric and magnetic (EM) fields, respectively. The tangential components  $k_x$  and  $k_z$  may be obtained by matching boundary conditions at  $y=0$  plane.

Consider the matrix form of Eq. (2.2.3),  $[\mathbf{K}][\mathbf{F}] = k_y[\mathbf{W}][\mathbf{F}]$ , where the elements of matrices  $[\mathbf{K}]$  and  $[\mathbf{W}]$  are functions of  $\omega, k_x, k_z$  and  $\varepsilon$ . The solutions of the matrix equation are given by  $\det([\mathbf{W}]^{-1}[\mathbf{K}] - k_y\mathbf{I}) = 0$ , where  $\mathbf{I}$  is an identity matrix and  $k_y$  is the eigenvalue of  $[\mathbf{W}]^{-1}[\mathbf{K}]$ . The column vector  $[\mathbf{F}]$  is composed of four sub-column-vectors,  $[E_x(\mathbf{G}_{lmn})]$ ,  $[E_z(\mathbf{G}_{lmn})]$ ,  $[H_x(\mathbf{G}_{lmn})]$  and  $[H_z(\mathbf{G}_{lmn})]$ , given by the eigenvector solutions of  $[\mathbf{W}]^{-1}[\mathbf{K}]$ . The Fourier coefficients of  $E_y$  and  $H_y$  may be further solved from the substitution equations. The total number of the eigenvalues is  $R = 4(2L+1)(2M+1)(2N+1)$ , since both  $[\mathbf{K}]$  and  $[\mathbf{W}]$  are  $R \times R$  square matrices. In each conjugate pair of the complex  $k_y$  roots,  $\text{Im}(k_y) < 0$  results in divergence such that only  $\text{Im}(k_y) > 0$  is allowed inside the PC region. Real  $k_y$  can be partitioned into an equal number of forward- and backward- propagating modes, since half of the real- $k_y$  modes have positive  $y$  component of Poynting vector. [7] In addition, all  $k_y^{(m)} = k_y + mb_2$ ,  $m = -M, -M+1, \dots, M$  may degenerate into one distinct solution due to the periodicity of the Brillouin zones. [7] Therefore the independent mode number is further reduced to  $2(2L+1)(2N+1)$  due to degeneracy. [7]

Next step is to evaluate the properties of each distinct mode. Time-independent Poynting vector may be calculated by  $\mathbf{S} = [\text{Re} \sum_{\mathbf{G}} \mathbf{E}^*(\mathbf{G}) \times \mathbf{H}(\mathbf{G})] / 2$ , which determines the group velocity direction of each mode. Consider the wavevector  $\mathbf{k}_s + \mathbf{G}_{lmn}$  of these modes independently at the interface between the uniform medium and the PC region, where  $s = 1, 2, \dots, 2(2L+1)(2N+1)$ . At  $y=0$  plane, all  $\mathbf{k}_s$  have same tangential

components and all tangential components of  $\mathbf{k}_s + \mathbf{G}_{lmn}$  have no  $\mathbf{b}_2$  included since  $\mathbf{b}_2$  is along  $\hat{y}$  axis. Therefore the wavevectors of the only allowed reflection modes at the incident side are given by

$$\begin{cases} \mathbf{k}_{ln} = k_{lnx}\hat{x} + k_{lny}\hat{y} + k_{lnz}\hat{z} \\ k_{lnx} = k_{0x} + l \cdot \mathbf{b}_{1x} + n \cdot \mathbf{b}_{3x} \\ k_{lnz} = k_{0z} + l \cdot \mathbf{b}_{1z} + n \cdot \mathbf{b}_{3z} \\ k_{lny} = -\sqrt{k_0^2 - k_{lnx}^2 - k_{lnz}^2} \end{cases}, \quad -L \leq l \leq L, \quad -N \leq n \leq N$$

The EM fields at both sides of the interface can be written as,

$$\begin{aligned} E_{x,I}(\mathbf{x}) &= E_{0x} e^{i\mathbf{k}_0 \cdot \mathbf{x}} + \sum_{ln} R_{lnx} e^{i\mathbf{k}_{ln} \cdot \mathbf{x}} \\ E_{z,I}(\mathbf{x}) &= E_{0z} e^{i\mathbf{k}_0 \cdot \mathbf{x}} + \sum_{ln} R_{lnz} e^{i\mathbf{k}_{ln} \cdot \mathbf{x}} \\ H_{x,I}(\mathbf{x}) &= H_{0x} e^{i\mathbf{k}_0 \cdot \mathbf{x}} + \sum_{ln} S_{lnx} e^{i\mathbf{k}_{ln} \cdot \mathbf{x}} \\ H_{z,I}(\mathbf{x}) &= H_{0z} e^{i\mathbf{k}_0 \cdot \mathbf{x}} + \sum_{ln} S_{lnz} e^{i\mathbf{k}_{ln} \cdot \mathbf{x}} \\ E_{x,II}(\mathbf{x}) &= \sum_s \sum_{lmn} T_s E_x(s, \mathbf{G}_{lmn}) \cdot e^{i(\mathbf{k}_s + l \cdot \mathbf{b}_1 + m \cdot \mathbf{b}_2 + n \cdot \mathbf{b}_3) \cdot \mathbf{x}} \\ E_{z,II}(\mathbf{x}) &= \sum_s \sum_{lmn} T_s E_z(s, \mathbf{G}_{lmn}) \cdot e^{i(\mathbf{k}_s + l \cdot \mathbf{b}_1 + m \cdot \mathbf{b}_2 + n \cdot \mathbf{b}_3) \cdot \mathbf{x}} \\ H_{x,II}(\mathbf{x}) &= \sum_s \sum_{lmn} T_s H_x(s, \mathbf{G}_{lmn}) \cdot e^{i(\mathbf{k}_s + l \cdot \mathbf{b}_1 + m \cdot \mathbf{b}_2 + n \cdot \mathbf{b}_3) \cdot \mathbf{x}} \\ H_{z,II}(\mathbf{x}) &= \sum_s \sum_{lmn} T_s H_z(s, \mathbf{G}_{lmn}) \cdot e^{i(\mathbf{k}_s + l \cdot \mathbf{b}_1 + m \cdot \mathbf{b}_2 + n \cdot \mathbf{b}_3) \cdot \mathbf{x}} \end{aligned} \quad (2.2.4)$$

where  $R_{ln}$  and  $S_{ln}$  are the EM field amplitudes of the reflection mode ( $ln$ ) in region I. In the uniform medium, the relationship between  $R_{ln}$  and  $S_{ln}$  is given by

$$\begin{cases} S_{lnx} = [(k_0^2 - k_{lnx}^2)R_{lnz} + k_{lnx}k_{lnz}R_{lnx}]/(\omega\mu_0k_{lny}) \\ S_{lnz} = [-(k_0^2 - k_{lnz}^2)R_{lnx} - k_{lnx}k_{lnz}R_{lnz}]/(\omega\mu_0k_{lny}) \end{cases} \quad (2.2.5)$$

$T_s$  is the amplitude of the transmission modes in region II. At  $y=0$  plane, the distinct modes in region I and region II both reduce to  $2(2L+1)(2N+1)$  such that the mode field amplitudes  $R_{lnx}$ ,  $R_{lnz}$  and  $T_s$  may be solved from the boundary equations.

### 2.3 DESIGN ON LOW-INDEX-CONTRAST SUPERPRISM STRUCTURE WITH EFFICIENT TRANSMISSION MODE

To clarify the theory with an example, we assume the PC region under consideration here is composed of polymer based crossing square rods [9, 10] embedded in an air background. The index contrast is 1.5:1. Here we will demonstrate how to employ our method to choose proper parameters and simulate the optical features of the low-index-contrast based PC structures.

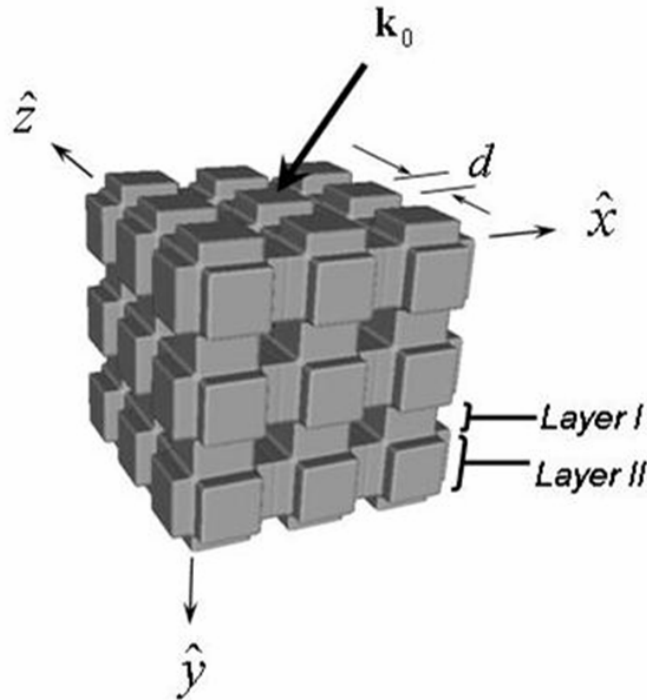


Fig. 2.3.1: A schematic of a 3D square-rod structure. [8]

Our interest in low-index-contrast PC structures stems from a wide variety of easy and inexpensive fabrication techniques available for such structures, including self-assembly, [11] holography, [12] two-photon absorption [13] and nanoimprint [14]. Our aim is to design a 3D PC structure exhibiting the superprism effect around the optical communication wavelengths of 1550 nm. A  $3 \times 3 \times 3$  section of a general square-rod structure is depicted in Fig. 2.3.1. From fabrication point of view, only two types of layers compose one period except the top and bottom ones. Thus it is convenient for fabrication. We set the side length of the square rod  $d = 0.8a$  to achieve high structure strength after fabrication. The interface between PC and air is (100).

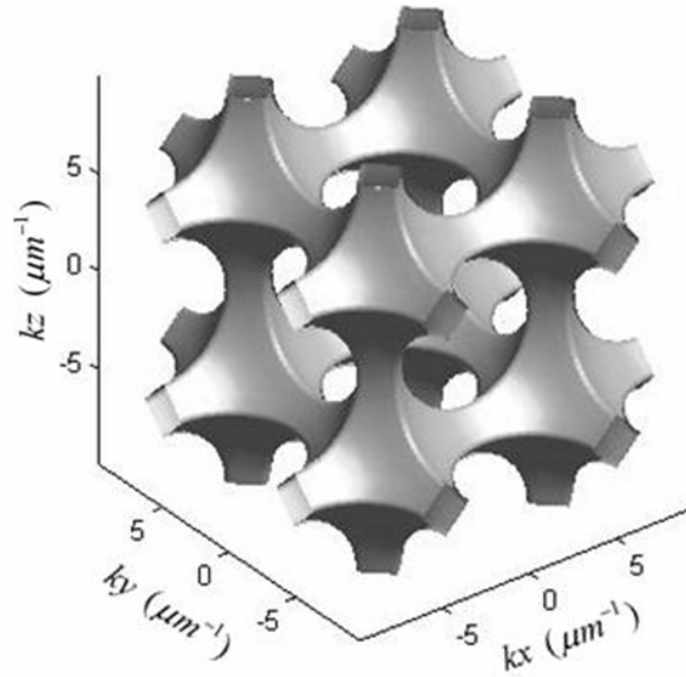


Fig. 2.3.2: 3D dispersion surface of the lowest band for the square-rod structure with  $a/\lambda = 0.40$ . [8]

We have used conventional PWE method to solve the 3D dispersion surface of the lowest band, and the result is plotted in Fig. 2.3.2. Superprism effect caused by PC structures is usually an incidental phenomenon in high dispersion region. In the cross section of dispersion surface with parallel planes, high dispersion happens around the rhombic profiles. Hereby we may choose  $k_z = k_{0z} = 0$  for simplicity.

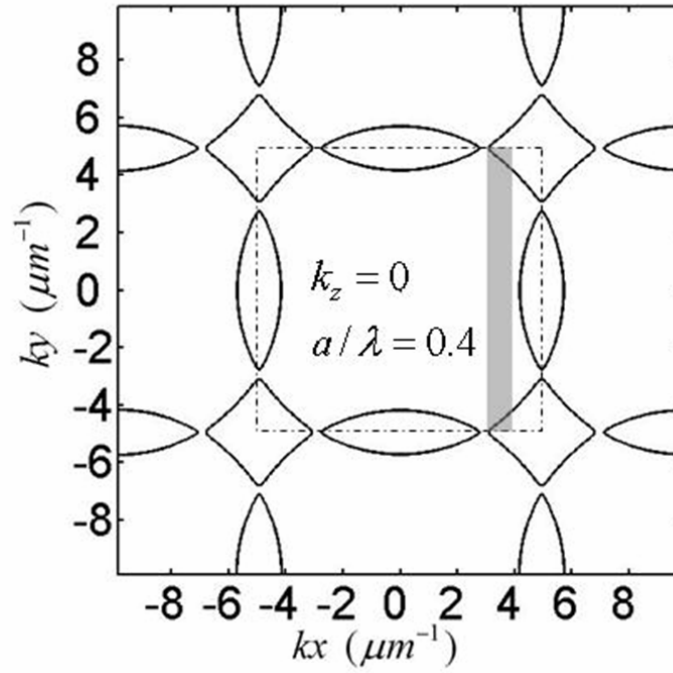


Fig. 2.3.3: Dispersion contours of all covered bands in  $k_z = 0$  plane, normalized frequency  $a/\lambda = 0.4$ . First Brillouin Zone is marked by a square frame. [8]

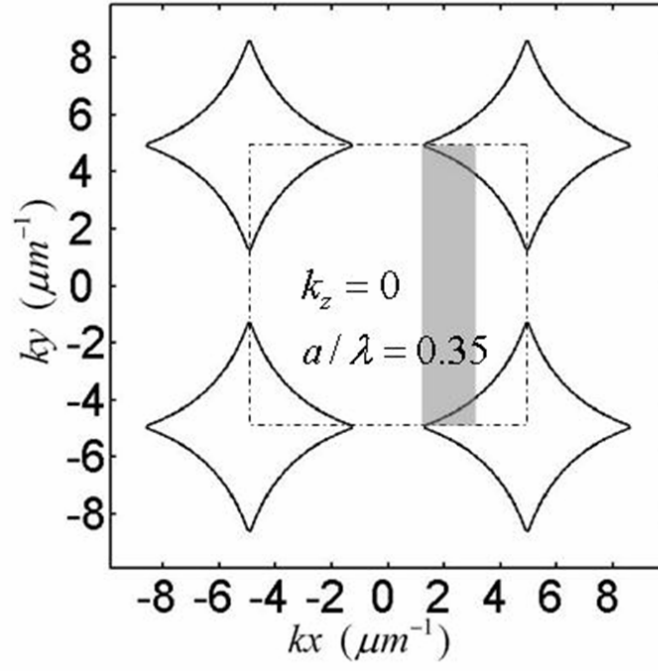


Fig. 2.3.4: Dispersion contours in  $k_z = 0$  plane,  $a/\lambda = 0.35$ . [8]

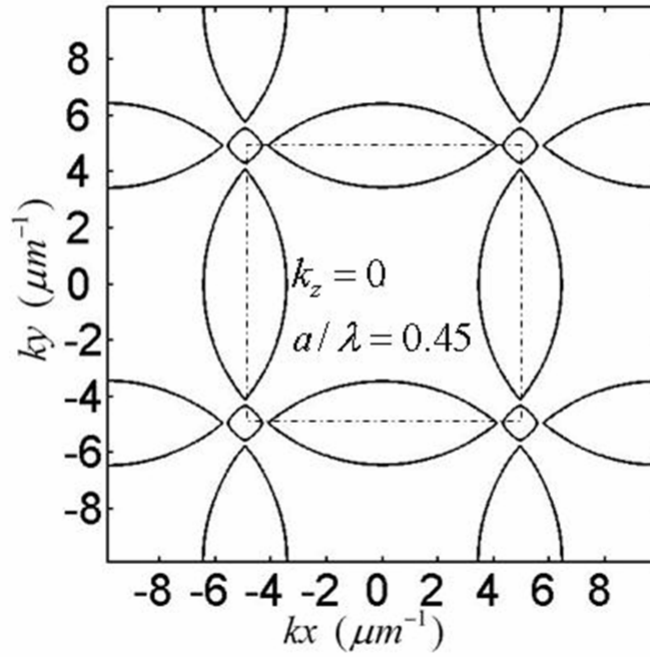


Fig. 2.3.5: Dispersion contours in  $k_z = 0$  plane,  $a/\lambda = 0.45$ . [8]



General PWE method is widely employed to calculate the normalized frequency  $a/\lambda$  of each photonic band. Then the dispersion surface of each band for an exact frequency can be solved by interpolation. Our center of attention is the dispersion contour at several frequency points, by which we can choose high dispersion region and evaluate the group velocity direction. However, for general PWE method, we must find all the bands that have common boundaries with the exact frequency. Our method is to find all  $k_y$  solutions based on given frequencies and tangential components of the incident fields. Therefore, the dispersion contour composed of all these common boundaries can be solved simultaneously. The dispersion surface sections of the square-rod structure computed by our method for three frequency points at  $k_z = 0$  plane are plotted in Fig. 2.2.3-Fig. 2.3.5. The rhombic profiles are part of the lowest-band dispersion surface, which is consistent with the conventional PWE [5] calculation result shown in Fig. 2.3.2. Other curves are common boundaries with higher bands. The rhombic profiles actually include two similar dispersion contours for transverse-electric (TE)-like and transverse-magnetic(TM)-like modes respectively, which exhibit similar optical properties due to rotation symmetry of square-rod structures. We assume the incident plane wave is a TE wave (electric field  $\mathbf{E}_t$  perpendicular to the  $x-y$  plane) and only consider the dispersion contour for TE-like modes during structure parameter design. The gray areas in Fig. 2.3.3 and Fig. 2.3.4 covering the high dispersion region only have intersections with the lowest-band dispersion contour. No intersection with higher band implies the structures have more chance to achieve high transmission. Thus  $k_x$  may be adjusted within the gray areas. The high dispersion regions in both Fig. 2.3.3 and Fig. 2.3.4 are magnified and plotted in Fig. 2.3.6, which may be used to estimate the power flow direction of transmitted modes since the group velocity is perpendicular to the dispersion contour. Arrows in Fig. 2.3.6 show small  $k_x$  change can result in close to  $45^\circ$

refraction angle scanning for both frequencies, while the flatness difference around the contour corner is obvious. Therefore, we have chosen  $a/\lambda = 0.40$  as our working frequency to achieve smooth angular change.

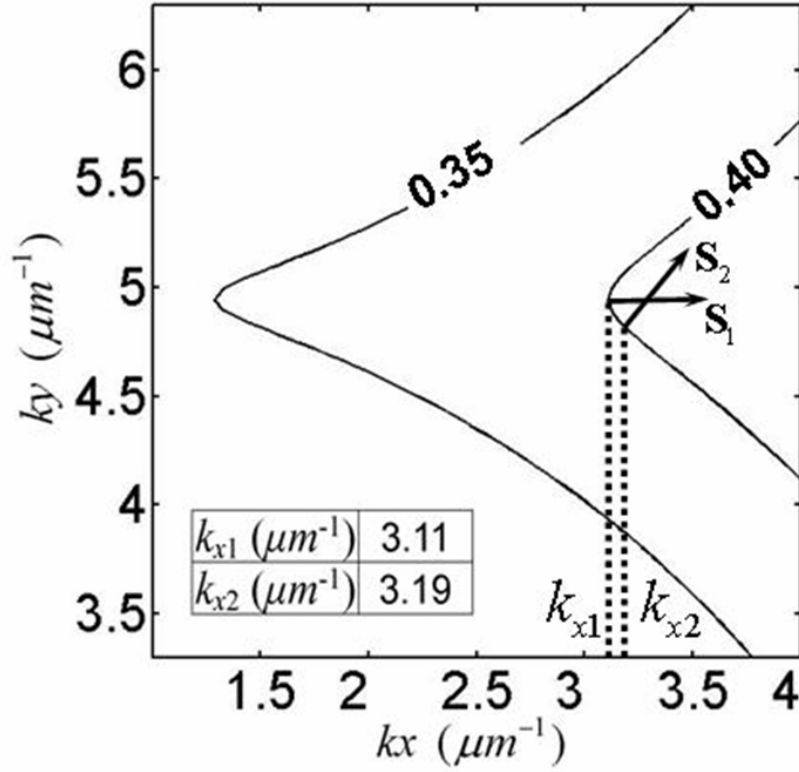


Fig. 2.3.6: Magnified dispersion contour corner of the lowest band with different normalized frequency  $a/\lambda = 0.35$  and  $0.40$ . The Poynting vectors  $S_1$  and  $S_2$  are marked with arrows. [8]

Fig. 2.3.7 shows adjacent dispersion contours with 20nm wavelength difference, where  $k'_x$  is the apex of the contour corner. The incident angle is set at  $60^\circ$  to keep  $k_x$  moving around the high dispersion region. Calculation shows both dispersion contour and

$k_x$  are shifting left when wavelength becomes longer, while the shift distances are different.

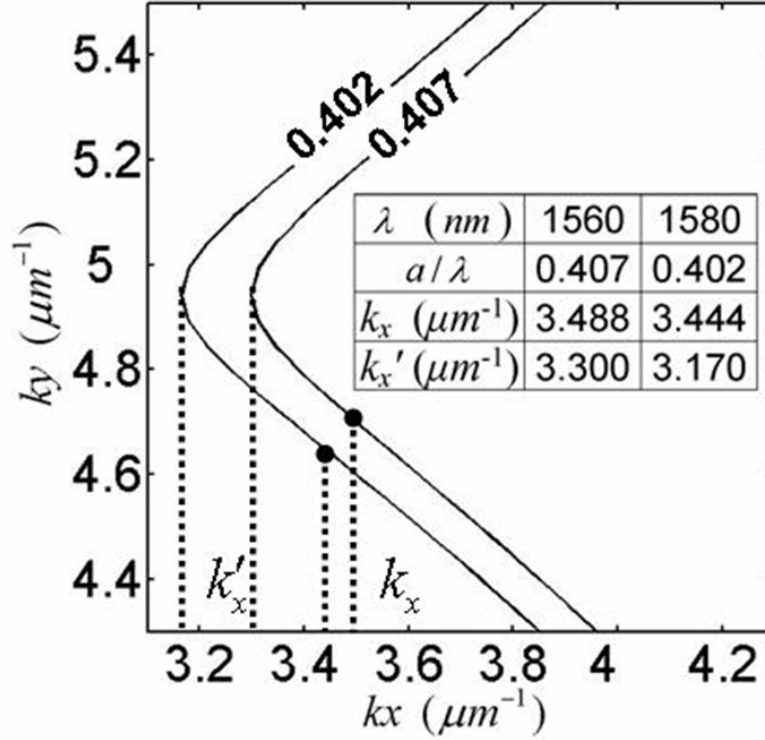


Fig. 2.3.7: Dispersion contours with 20nm wavelength difference. The derived wavevector and contour corner position are marked as  $k_x$  and  $k'_x$ , respectively. Numerical results are listed in the inset tables. [8]

The incident angle in our example has been finely adjusted to  $55.8^\circ$  to achieve superprism effect in this region. The scanning effect of refraction angle and the normalized transmission are illustrated in Fig. 2.3.8. The angular scanning range and high transmission in the designed wavelength range (1550-1580nm) are consistent with our anticipation. Near 100% transmission proves that the PC structures behave differently from homogeneous medium when  $\lambda$  is far away from the long-wavelength limit. [6]

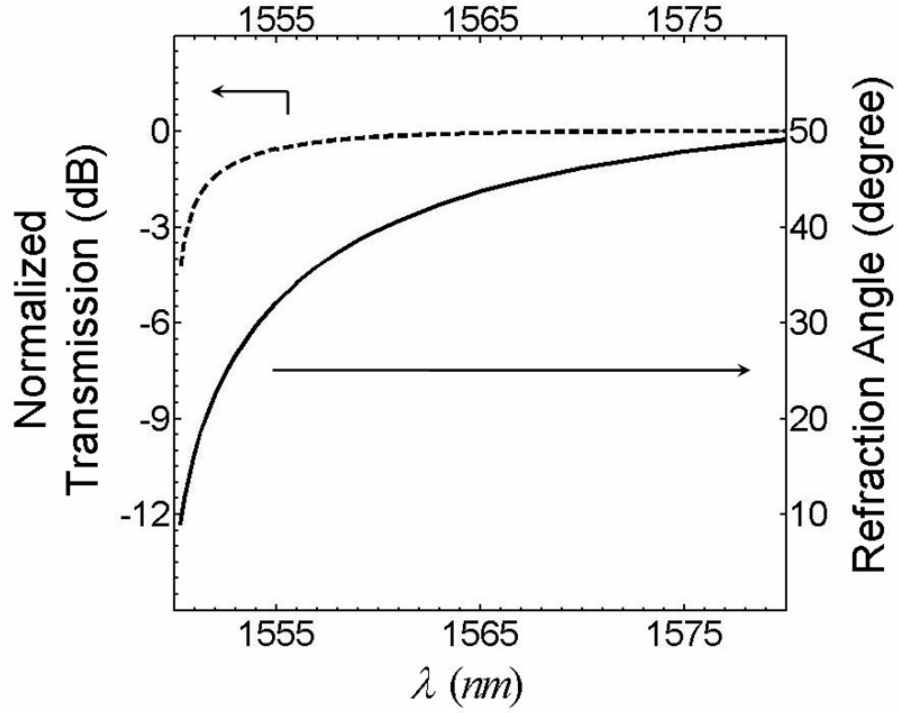


Fig. 2.3.8: Superprism effect at the lowest band of the three-dimensional square-rod photonic crystal. The refraction angle (solid curve) and normalized transmission (dotted curve) for the designed wavelength range (1550 - 1580nm) are indicated respectively. [8]

Figure 2.3.9 indicates the refraction angle and transmission for similar PC structures with polymer index changed by as much as  $10^{-3}$  and  $10^\circ$  angular coverage can be achieved at  $\lambda = 1552\text{nm}$ , which confirmed another feature of superprism effect – high sensitivity to refractive index. [3] Our theory predicts that such a sensitivity is accompanied by less than 3dB transmission loss. Therefore, these structures are highly useful for active laser beam scanning applications, where the laser beam direction can be widely manipulated by slight tuning of the refractive index. 729 planar waves have been

applied to achieve reasonable accuracy in our calculation and the numerical stability has been verified based on energy conservation and solution convergence. Using TMM, Minami et al. also studied the intensity of transmitted and reflected modes in similar square-rod structures. [10] As he pointed out, the eigenvalue solutions of TMM are actually  $e^{ik_y(s)d}$ , which may stretch over a very large scale and result in overflow or underflow during the numerical evaluation. In contrast, our method solves  $k_y(s)$  directly and keeps the numerical distribution of the solved eigenvalues within a comparatively smaller range.

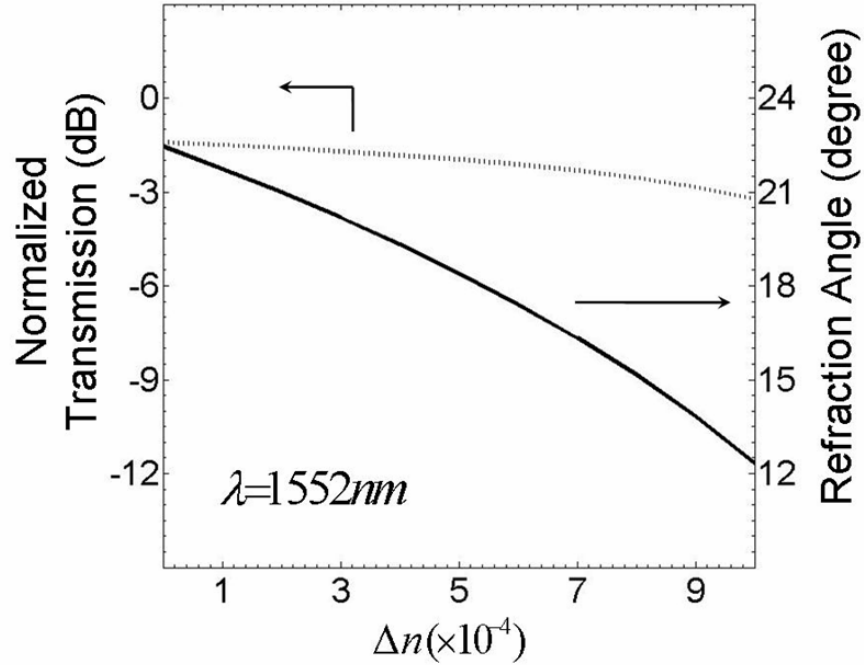


Fig. 2.3.9: The refraction angle (solid curve) and normalized transmission (dotted curve) for a photonic crystal with polymer index changed by up to  $10^{-3}$ . [8]

## 2.4 SUMMARY

A rigorous vector-field theory has been developed to study the anomalous light refraction effect at the interface between a semi-infinite 3D photonic crystal and a homogeneous medium. The light beam direction and optical-field amplitude of both reflected and transmitted modes through photonic crystals are rigorously analyzed and derived as linear equations in matrix form. We have further illustrated how to employ our refraction theory on parameter adjustment to achieve superprism effect by low-index-contrast square-rod structures. Our method can be applied to high-index-contrast PC structures [15-17] as well. Further extending this method to disordered photonic crystals [18] could be another direction to explore. In addition, photonic crystal slabs, with their hybrid approach of in-plane band gap combined with vertical index-confinement, promise a viable route to achieving photonic crystal waveguide effects in real systems.

*Reference:*

- [1] H. Kosaka, T. Kawashima, A. Tomita, M. Notomi, T. Tamamura, T. Sato, and S. Kawakami, "Superprism phenomena in photonic crystals," *Phys. Rev. B, Condens. Matter*, vol. 58, no. 16, pp. R10096–R10099, Oct. 1998.
- [2] J. Shin and S. Fan, "Conditions for self-collimation in three-dimensional photonic crystals," *Opt. Lett.*, vol. 30, no. 18, pp. 2397-2399 Sep. 2005.
- [3] T. Prasad, V. Colvin, and D. Mittleman, "Superprism phenomenon in three-dimensional macroporous polymer photonic crystals," *Phys. Rev. B*, vol. 67, no. 16, p. 165 103, Apr. 2003.
- [4] Z. Lu, J. A. Murakowski, C. A. Schuetz, S. Shi, G. J. Schneider, and D. W. Prather, "Three-dimensional subwavelength imaging by a photonic-crystal flat lens using negative refraction at microwave frequencies," *Phys. Rev. Lett.*, vol. 95, no.15, p. 153 901, Oct. 2005.
- [5] S. G. Johnson and J. D. Joannopoulos, "Block-iterative frequency-domain methods for Maxwell's equations in a planewave basis," *Opt. Express* vol. 8, no. 3, pp. 173-190, Jan. 2001.
- [6] Z. Li and K. Ho, "Application of structural symmetries in the plane-wave-based transfer-matrix method for three-dimensional photonic crystal waveguides," *Phys. Rev. B*, vol. 68, no. 24, p. 155 101, Dec. 2003.
- [7] W. Jiang, R. T. Chen and X. Lu, "Theory of light refraction at the surface of a photonic crystal," *Phys. Rev. B*, vol. 71, no. 24, p. 245 115, Jun. 2005.
- [8] Xiaonan Chen, Wei Jiang, Jiaqi Chen, and Ray T. Chen, "Theoretical Study of Light Refraction in Three-Dimensional Photonic Crystals," *IEEE/OSA Journal of Lightwave Technology*, vol. 25, no. 9, pp. 2469-2474, Sept. 2007.
- [9] H. S. Sozuer and J. W. Haus, "Photonic bands – simple-cubic lattice," *J. Opt. Soc. Am. B*, vol. 10, no. 2, pp. 296-302, Feb. 1993.
- [10] T. Minami, H. Ajiki, K. Cho, "Branching ratio of light incident on a photonic crystal in a multibranch dispersion region," *Physica E-low-dimensional systems & nanostructures*, vol. 13, no. 2-4, pp. 432-436, Mar. 2002.
- [11] Y. A. Vlasov, X.-Z. Bo, J. C. Sturm, and D. J. Norris, "On-chip natural assembly of silicon photonic bandgap crystals," *Nature* vol. 414, no. 6861, pp. 289-293 Nov. 2001.
- [12] J. Chen, W. Jiang, X. Chen, L. Wang, S. Zhang, and R. T. Chen, "Holographic three-dimensional polymeric photonic crystals operating in the 1550 nm window," *Appl. Phys. Lett.*, vol. 90, p. 093 102, Feb. 2007.
- [13] V. Mizeikis, K. K. Seet, S. Juodkazis, and H. Misawa, "Three-dimensional woodpile

- photonic crystal templates for the infrared spectral range,” *Opt. Lett.*, vol. 29, no. 17, pp. 2061–2063, Sep. 2004.
- [14] K. Inoue and K. Ohtaka, *Photonic Crystals: Physics, Fabrication and Applications*, Springer-Verlag, New York, 2004.
- [15] L. Gu, W. Jiang, X. Chen, L. Wang, and R. T. Chen, “High speed silicon photonic crystal waveguide modulator for low voltage operation,” *Appl. Phys. Lett.*, vol. 90, no. 7, p. 071 105, Feb. 2007.
- [16] L. Gu, W. Jiang, X. Chen, and R. T. Chen, “Thermooptically Tuned Photonic Crystal Waveguide Silicon-on-Insulator Mach–Zehnder Interferometers,” *IEEE Photon. Tech. Lett.*, vol. 19, no. 5, pp. 342–344, Mar. 2007.
- [17] Y. Jiang, W. Jiang, L. Gu, X. Chen, and R. T. Chen, “80-micron interaction length silicon photonic crystal waveguide modulator,” *Appl. Phys. Lett.*, vol. 87, no. 22, p. 221 105, Nov. 2005.
- [18] W. Jiang and C. Gong, “Two mechanisms, three stages of the localization of light in a disordered dielectric structure with photonic band gaps,” *Phys. Rev. B*, vol. 60, no. 17, p. 12015, Nov. 1999.



## **Chapter 3: *Theoretical and experimental study of 1-D photonic crystals for true-time-delay line applications***

### **3.1 INTRODUCTION**

As one of the key technologies in modern radar and communication systems, phased-array antennas are desirable for low visibility, high directivity, quick and accurate beam steering, and reduced power consumption. Optical true-time delay techniques have been developed to overcome the frequency squint effect, providing wide bandwidth and low electromagnetic interference compared with electronic phase-shifter approaches [1, 2]. High packaging density and the large delay coverage are considered two critical factors in a practical phased-array antenna system.

In this chapter, we propose a novel symmetric structure for the true-time delay module. It has a more compact package size that is only 5% of the original structure we reported [3]. The miniaturized time delay module was experimentally confirmed to provide continuous time delays from -65 to +65 ps with a  $1 \times 4$  subarray antenna operating at K-band (18-26.5 GHz) frequency. We describe herein the device structure of the optical true-time delay module and the measured delay-wavelength curves.

### **3.2 WAVELENGTH DISPERSION IN 1-D PHOTONIC CRYSTALS – HOLOGRAM GRATINGS**

Volume holographic grating is a “thick” grating that usually works in the Bragg regime. Light diffraction in such a thick holographic grating occurring at or near the Bragg angle leads to efficient wave-front reconstruction, and thus provides important applications in a variety of optical systems. Various approximate theories have been developed to simplify the analysis of gratings with good accuracies under some specific assumptions that apply to the investigated systems. The two-wave first-order coupled-wave theory, which neglects second derivatives, boundary effects and higher orders wave

( $i \neq 0,1$ ), was first applied to holographic grating by Herwig Kogelnik [4]. His paper published in 1969 is widely referenced to analyze the holographic gratings, and this theory is commonly called the “Kogelnik theory” [4]. His theory is based on a few assumptions:

(1) The spatial modulation of the refractive index and the absorption constant is of a sinusoidal form.

(2) The holographic grating is thick and the monochromatic light incident on the grating is at or near the Bragg angle. Therefore, only two waves obeying the Bragg condition at least approximately are retained, other diffraction orders are neglected.

(3) The same average dielectric constant is assumed for the region inside and outside the grating boundaries, which means that all second derivatives of the field amplitudes from the rigorous coupled-wave equations and their correspondent boundary conditions are eliminated from the derivation of this theory.

The substantial recognition received by Kogelnik theory is in part because it provides analytical solutions for a comprehensive coverage of (1) phase, absorption, and mixed gratings; (2) on-Bragg and off-Bragg incidence; (3) pure transmission and pure reflection in general slanted fringe gratings; (4) both TE-mode and TM-mode polarization.

For transmission holographic grating, the analytic expression of the diffraction efficiency of a transmission volume grating for TE-mode is given by

$$\eta = \sin^2(\nu^2 + \xi^2)^{1/2} / (1 + \xi^2 / \nu^2), \quad (3.2.1)$$

$$\nu = \frac{\pi \Delta n d}{(c_R c_S)^{1/2}}, \quad (3.2.2)$$

$$\xi = -\Delta \lambda K^2 d / 8 \pi n c_{S1}, \quad (3.2.3)$$

$$c_R = \cos \theta, \quad (3.2.4)$$

$$c_s = \cos \theta - \frac{K}{\beta} \cos \varphi, \quad (3.2.5)$$

$$K = \frac{4\pi n}{\lambda_0} \cos(\varphi - \theta), \quad (3.2.6)$$

$$\beta = \frac{2\pi n}{\lambda}, \quad (3.2.7)$$

where  $\theta$  is the designed incident angle inside the holographic grating,  $\lambda_0$  is the designed wavelength in air,  $\varphi$  is the slant angle of volume grating,  $d$  is the sickness of the grating,  $K$  is the grating vector,  $n$  is the average refractive index modulation of the recording medium, and  $\Delta n$  is the maximum index modulation of the photopolymer which can be controlled by exposure dosage. All of these parameters are illustrated in Fig 3.2.1. For TM mode, most equations above are valid except a change on  $v$  to  $v'$ , which becomes  $v' = -v \cos 2(\theta - \varphi)$ .

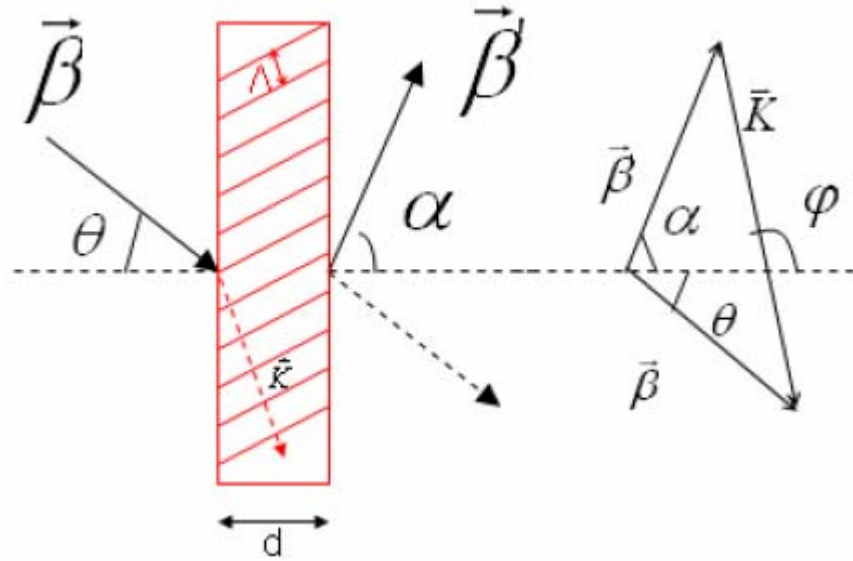


Fig. 3.2.1: Vector diagram for Bragg regime diffraction.

### 3.3 DESIGN ON STRUCTURE MINIATURIZATION AND DELAY TIME ENHANCEMENT

The optical true-time delay modules we describe here are based upon the volume holographic grating effect. The wavelength-dependent diffraction angle out of a volume grating creates different physical paths for different input signals. The input wavelength can be precisely tuned to achieve the accurate time delay required for a continuous beam scanning. The achievable and required time delays for the antenna system are analyzed respectively in later discussion.

A schematic of the true-time delay module is shown in Fig. 3.3.1. A waveguide hologram based volume grating was used to couple an incident beam from a single-mode collimator into a glass substrate. As shown in Fig. 3.3.2, after traveling for a one-bounce distance, the beam was surface normally coupled out by an output holographic grating.

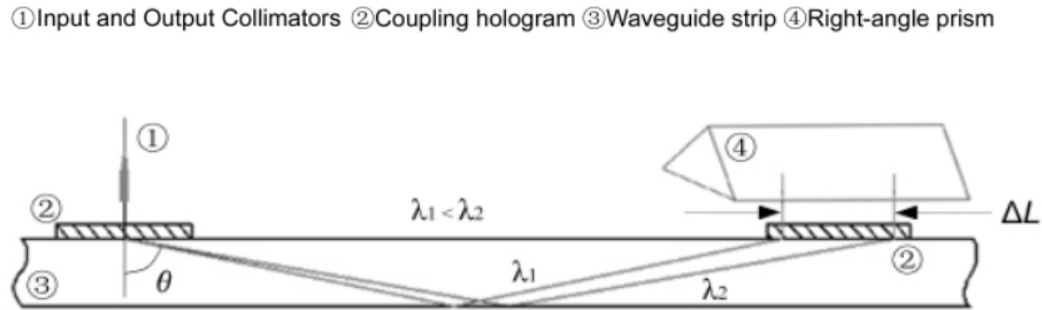


Fig. 3.3.1: Symmetric structure of the wavelength-tuning hologram waveguide-based true-time delay modules, consisting of input and output collimators with single-mode fiber pigtails, input and output dispersive holographic grating couplers, right angle prism and glass waveguide strip. The final output position was fixed while the diffraction angle  $\theta$  changed with the incident wavelength  $\lambda$ . [7]

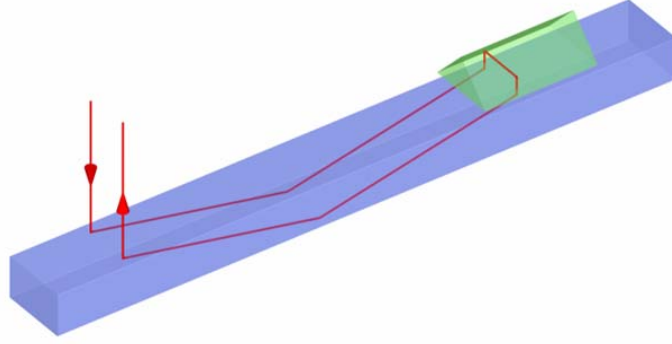


Fig. 3.3.2: 3-D symmetric structure of the wavelength-tuning hologram waveguide-based true-time delay modules. [7]

According to the coupled-wave theory [4], the diffraction angle  $\theta$  is determined by the Bragg condition

$$\theta(\lambda) = 2 \arcsin(\Lambda/2\lambda), \quad (3.3.1)$$

where  $\Lambda$  is the grating period of the dispersive hologram and  $\lambda$  is the incident wavelength. To achieve sufficient dispersive capability of the holographic grating, a large diffraction angle of  $80^\circ$  was chosen at the center wavelength of 1550 nm with the grating period  $\Lambda = 1205.7 \text{ nm}$  [3]. The waveguide holograms were recorded on Dupont photopolymer film (HRF 600x001-20) by the two-beam interference method. A right angle prism was placed on top of the photopolymer to achieve required refraction angles of the recording beams which are larger than the total internal reflection (TIR) angle between the air and photopolymer.

In our previous work [3] shown in Fig. 3.3.3, the beam was designed to be coupled out from the substrate and collected by a collimator directly. This scheme requires a sufficiently large diameter of the collimator to cover the beam position shift due to wavelength tuning.

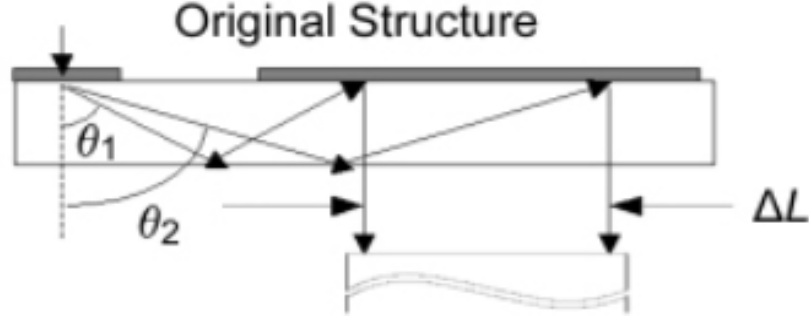


Fig. 3.3.3: A previously proposed structure, in which the final output position was not fixed, which made the coupling to a single-mode fiber much more difficult. [3]

For a single zigzag beam path, the time delay is given by

$$t_{single}(\theta) = 2nh/(\cos \theta \cdot c), \quad (3.3.2)$$

where  $n$  is the refractive index of the glass,  $h$  is the thickness of the substrate and  $c$  is the light speed in free space. The maximum achievable time delay  $\Delta T$  and the variation of the output position  $\Delta L$  are determined by the minimum and maximum diffraction angle  $\theta_1$  and  $\theta_2$ , such that

$$\Delta T = 2nh/c \cdot (1/\cos \theta_2 - 1/\cos \theta_1) \quad (3.3.3)$$

$$\Delta L = 2h(\tan \theta_2 - \tan \theta_1), \quad (3.3.4)$$

where the values of  $\theta_1$  and  $\theta_2$  are limited by the amount of achievable wavelength tuning range as indicated in equation 3.3.1. Similarly, the time delay difference  $\Delta T_d$  achieved by different delay units is derived as

$$\Delta T_d = 2n\Delta h/c \cdot (1/\cos \theta_2 - 1/\cos \theta_1), \quad (3.3.5)$$

where  $\Delta h$  is the thickness difference between the substrates in the time delay units connected to adjacent antenna elements. Combination of Eq. 3.3.3 and Eq. 3.3.5 gives

$$\Delta T = \Delta T_d h / \Delta h . \quad (3.3.6)$$

The time delay required to steer a phased-array antenna operating at microwave frequencies over a given range of scan angles is dependent on the element spacing  $d$  and the number of elements. Specifically, the time delay difference between adjacent antenna elements  $\Delta T_d$  required to achieve beam scanning of  $\pm\alpha$  degree is given by

$$\Delta T_d = 2d \sin \alpha / c , \quad (3.3.7)$$

such that the required time delay of one delay unit is given by

$$\Delta T = 2 \cdot (d \sin \alpha / c) \cdot (h / \Delta h) . \quad (3.3.8)$$

A series of delay units with equal thickness difference ( $h_1 = 1mm$ ,  $h_2 = 3mm$ ,  $h_3 = 5mm$ ,  $h_4 = 7mm$ ) were integrated as a true-time delay system, in order to use a single tunable laser to create the required delay difference  $\Delta T_d$  for multiple elements in the antenna array. For the original delay module described in [3], the achievable wavelength tuning range and the device parameters were designed as  $\lambda_2 - \lambda_1 = 12nm$ ,  $\theta_1 = 77.5^\circ$ ,  $\theta_2 = 82^\circ$ ,  $\Delta T = 128ps$ ,  $\Delta L = 36.5 mm$ , which allowed  $-37^\circ \sim +37^\circ$  beam scanning coverage for the X-band phased-array antenna system. It is seen from the calculation that a collimator with an effective diameter larger than 36.5 mm has to be used in the system to cover the large  $\Delta L$  value. Collimators with such a large numerical aperture introduce a few problems such as large size multimode outputs and low coupling efficiency, which make it impractical for real applications.

In the new delay module described here, the output beam is first coupled into a right-angle prism, which reflected the light beam and formed an additional reversed beam path within the substrate. Having bi-directional, symmetric beam paths causes the final output position to be fixed. Miniaturized collimators with single-mode fiber pigtails could then be used to collect the output signal. Furthermore, in the novel symmetric structure, the time delay is doubled due to the backward bounce of the light beam. With the same

requirement of maximum achievable time delay, the incident wavelength tuning range is reduced compared with the original single-path structure.

### **3.4 FABRICATION OF THE HOLOGRAM MODULE**

We use DuPont's photopolymers for holographic recording since they offer significant advantages over conventional holographic recording medium such as dry-processing capability, long shelf life, good photo-speed, and large index modulation. [5 ,6] These photopolymers are not a single material, but consist of a polymeric binder, photo-initiator, polymerizable monomers, sensitizing dyes, and occasionally other ingredients such as plasticizers and surfactants. These compositions are manufactured by dissolving ingredients in a suitable organic solvent, typically a mixture of methylene chloride and methanol, and casting the solution onto a clear solid film support of polyethylene terephthalate (Mylar) using conventional web coaters equipped with either a doctor knife or extrusion die along with an in-line drier and lamination station. A cover sheet of thin Mylar is laminated to the slightly tacky coatings after drying. The cover sheet protects the soft, tacky photopolymer layer from dust and handling. It can be removed prior to imaging, allowing the material to be laminated to glass, plastic or other substrates.

The formation of the volume holographic gratings in photopolymer films can be briefed as follows. The monomer inside the photopolymer films starts to polymerize in regions exposed to bright interference fringes during the holographic recording. As conversion of monomer to photopolymer occurs, fresh monomer diffuses in from neighboring dark regions, thus setting up concentration and density gradients that result in refractive index modulation. The decrease in molecular volume associated with converting monomer to polymer is probably a major factor in drawing additional unreacted monomer into the polymerization region. As exposure and polymerization proceed, the initial highly viscous composition gels and hardens, diffusion is then



suppressed, and further hologram recording stops. At this point, the hologram image consists of photopolymer-rich regions that monomer diffused into and binder-rich regions that it diffused away from, probably with some residual un-reacted monomer distributed throughout. The hologram is now stable toward further exposures. Sometimes, a final simple heating process can help enhance the index modulation through additional diffusion and distribution of components between the photopolymer-rich and binder-rich regions of the hologram.

DuPont photopolymer HRF 600X001-20 (20  $\mu\text{m}$  thick) made by DuPont (DuPont Holographic Materials, Wilmington, Delaware) was used as the recording medium for volume hologram recording. The hologram was fabricated by a two-beam interference method using the setup shown in Fig. 3.4.1. The 532 nm line from a Verdi laser was used as the light source for exposure. An electrically timed shutter was employed to accurately control the exposure time. The S-polarization (E perpendicular to plane of incidence) laser beam was first split into two beams with equal power by a beam splitter. A halfwave plate in conjunction with a polarizing beam splitter was used to adjust the intensity of one beam and maintain the polarization of the adjusted beam as well. To eliminate the inevitable involved scattering noise, a pinhole was situated at the focal point for an objective lens for each beam to perform the spatial filtering.

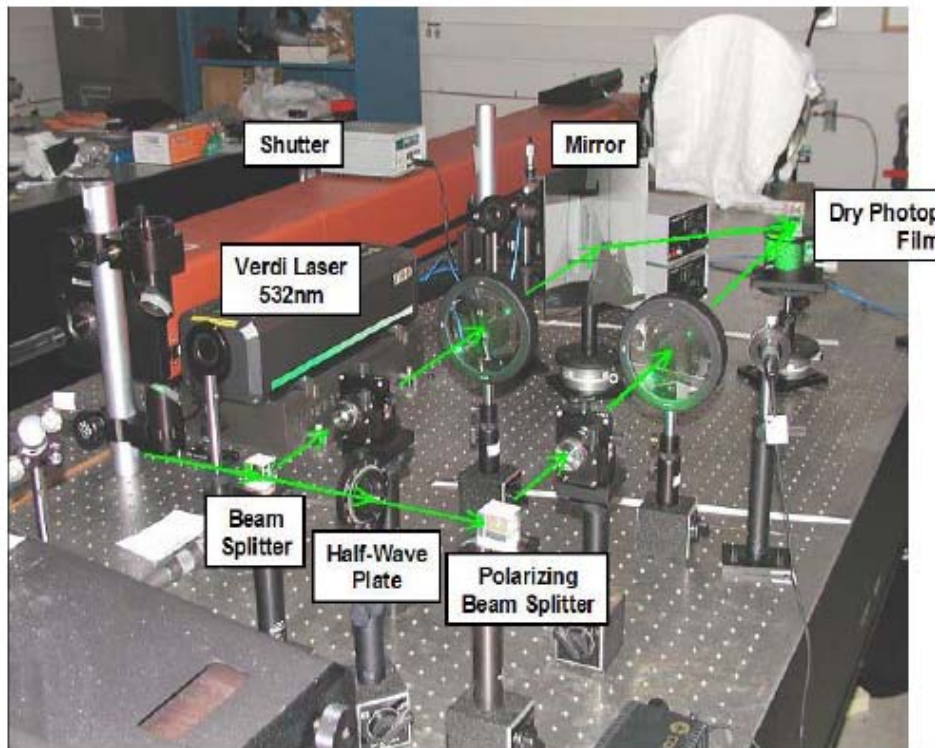
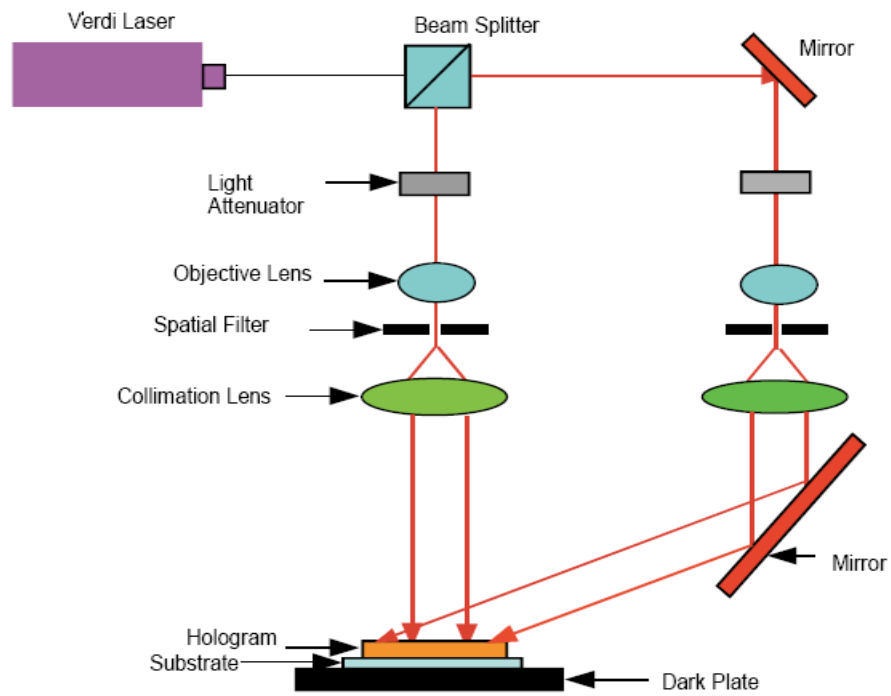


Fig. 3.4.1: Setup for holographic recording: schematic and real setup.

Two collimating objective lenses were employed to collimate the focused laser beams into plane waves, and expand them to be much larger than the recording area, which guaranteed the uniformity of the formed grating structures. A reflection mirror was mounted on a rotational stage to bend one laser beam towards the recording stage. A glass holder was mounted on a 3-D translational/rotational recording stage. The glass was painted dark to reduce the Fresnel reflection that may cause interference noise during the hologram construction. Recording angles of two beams can be adjusted by tuning the rotational angles of the mirror and recording stage. For the fabrication of hologram, dry photopolymer films were laminated onto a substrate (BK-7 or quartz). The protection Mylar cover was removed just prior to the recording. The device substrate was placed against the glass holder with some indexmatching liquid sealing in between. Two finely adjusted laser beams interfered and created an image with a periodic pattern, which in turn exposed the photopolymer and led to an internal spatial index modulation.

### **3.5 CHARACTERIZATION OF THE HOLOGRAM MODULE**

The measurement system used to evaluate the new delay modules is presented in Fig. 3.5.1. An HP network analyzer (8510C) was used to measure radio-frequency (RF) phase as a function of RF frequency, from which we could calculate the experimental time delay. A C-band (1530 - 1560 nm) tunable laser was modulated by an external 40-GHz polymer Mach-Zehnder intensity modulator, which was driven by port 1 of the network analyzer. The modulated signal was fed into the delay device and then converted to an electrical signal by the 40-GHz PIN photodetectors. After amplification, the signal was received by port 2 of the network analyzer. The RF phase versus RF frequency as a function of incident optical wavelength is shown in Fig. 3.5.2. Linearity of the measured phase versus frequency characteristic confirms that the measured time delays are independent of RF frequencies. The corresponding time delays are shown in Fig. 3.5.3.

Compared with the original structure, the new structure provides doubled maximum achievable time delay within the same incident wavelength range that is consistent with the simulation results. The simulated beam scanning angle versus time delay curve for an X-band antenna is shown in Fig. 3.5.4. Figure 3.5.5 confirms that this symmetric structure provides a much more compact packaging size ( $12\text{cm} \times 2\text{cm} \times 1.2\text{cm}$ ) and less coupling loss (2dB) compared with the original single-path design ( $15\text{cm} \times 15\text{cm} \times 3\text{cm}$ , 10dB) where multimode-to-single-mode conversion is required.

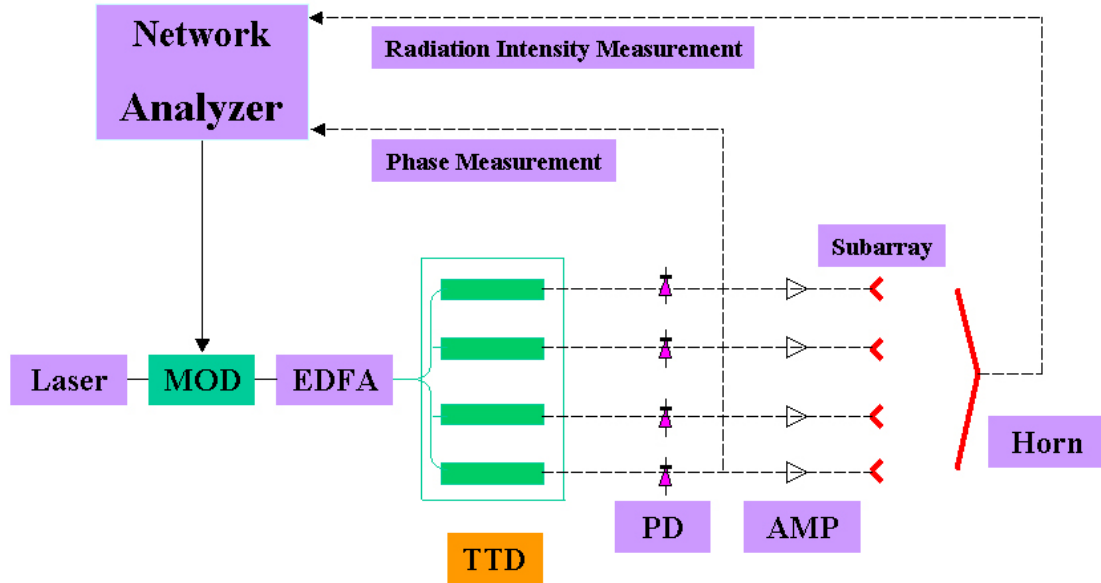


Fig. 3.5.1: Block diagram for time delay (phase versus frequency) measurement and system demonstration. Tunable Laser: used to provide light with wavelength tunable from 1544 – 1556 nm. Network Analyzer: used to measure the phase and intensity of the RF signal. PD: four 40-GHz photodetectors. AMP: four 2-stage RF amplifiers. MOD: 40-GHz polymer Mach-Zehnder intensity modulator. TTD: True-time-delay modules of the type depicted in Fig. 3.3.1. [7]

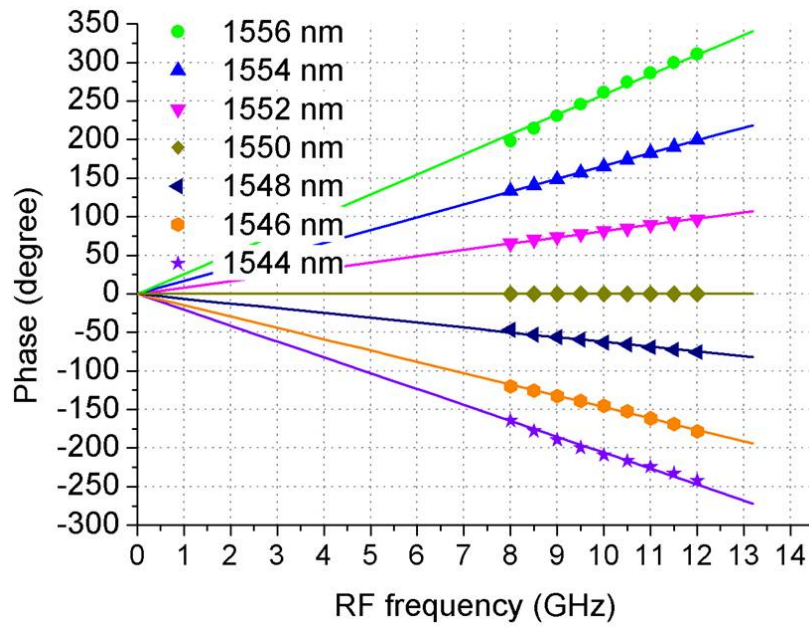


Fig. 3.5.2: Measured (points) and simulated (lines) results of RF phase versus RF frequency. [7]

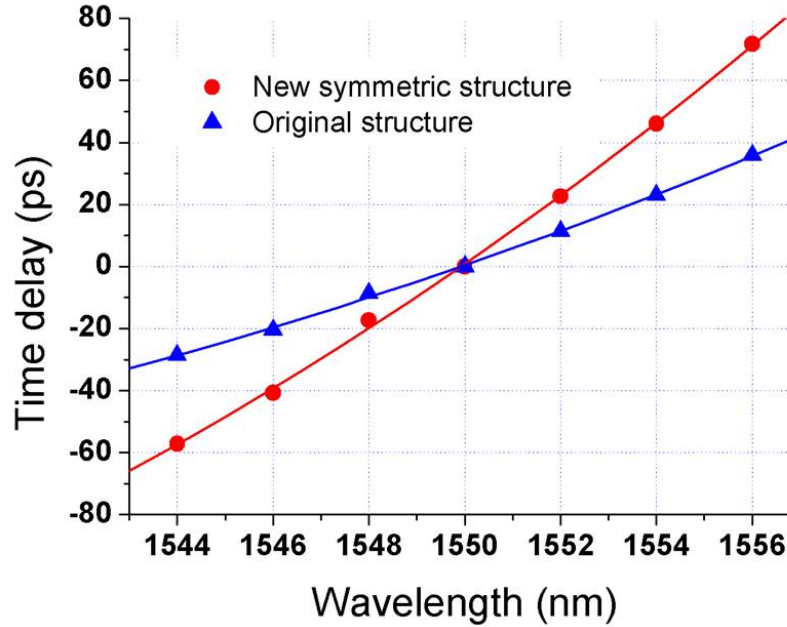


Fig. 3.5.3: Measured (points) and simulated (lines) results of time delay versus incident wavelength compared with original structure. [7]

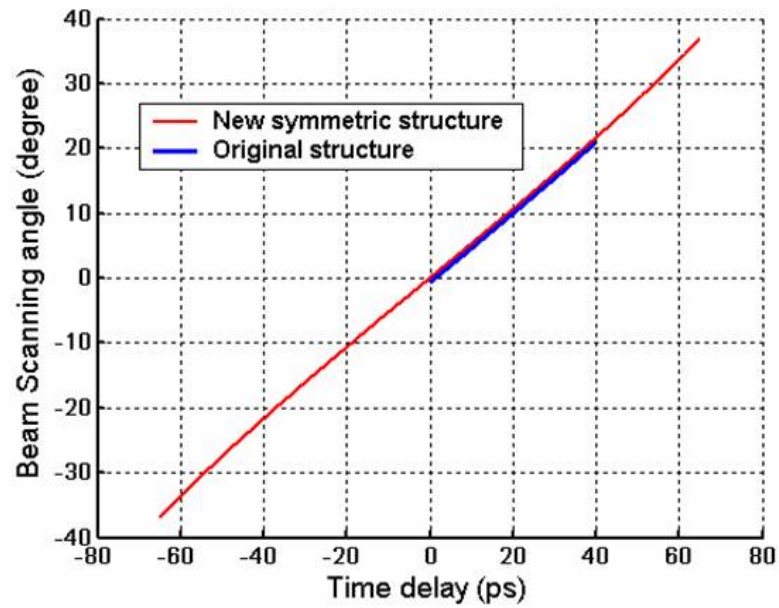


Fig. 3.5.4: Comparison of simulated beam scanning angle versus controlled time delay for X-band elements. [7]

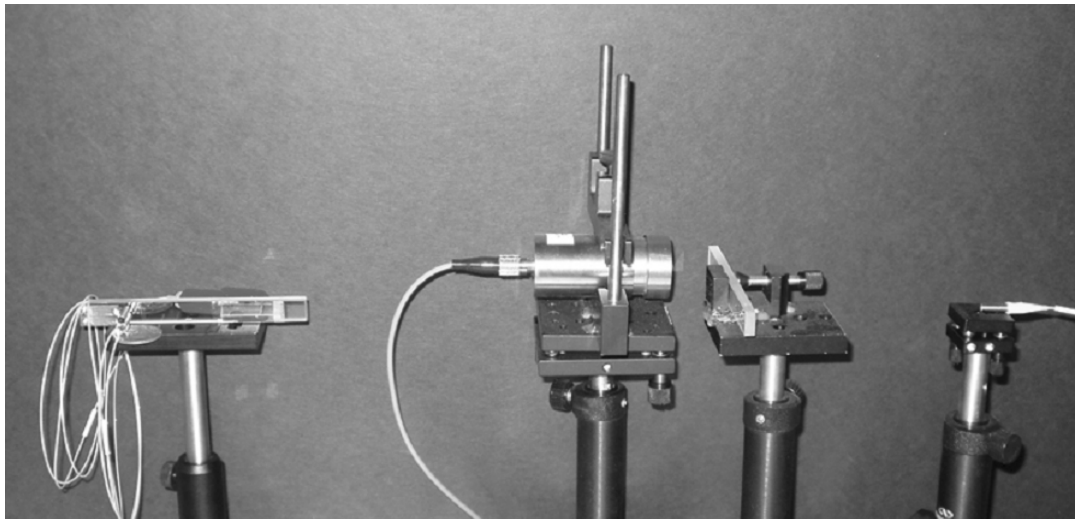


Fig. 3.5.5: Size comparison between new symmetric structure (left) and previous structure (right) described in [3].

### 3.6 DEMONSTRATION OF OPTIMIZED HOLOGRAM MODULE IN PHASE-ARRAY ANTENNA SYSTEM

We integrate the optimized hologram module with a 4-element sub-array antenna system, as shown in Fig. 3.6.1. Calculation based on equation 3.3.8 gives the delay requirements (3.6.1) for K-, Ku- and X-band phased-array antenna systems. With the enhanced delay coverage, the demonstrated 4-element phased-array antenna system can cover a larger beam scanning angle,  $-37^\circ \rightarrow +37^\circ$  for X-band antenna elements ( $d = 13 \text{ mm}$ ) and  $-45^\circ \rightarrow +45^\circ$  for K-band antenna elements ( $d = 7 \text{ mm}$ ). At the receiving end of the system measurement setup, an antenna horn was used to receive the phased-array radiation signal. The broadside radiation axis of the antenna array was precisely rotated and situated at the azimuth angle, relative to the horn's broadside radiation axis.

Operating Band	Antenna Element Spacing (d)	Beam Scanning Angle ( $\alpha$ )	Time Delay Requirement ( $\Delta T$ )
K-band (18-26.5 GHz)	7 mm	$\pm 45^\circ$	82ps
Ku-band (12.5-18 GHz)	10 mm	$\pm 45^\circ$	118ps
X-band (8-12.5 GHz)	13 mm	$\pm 37^\circ$	130ps

Table 3.6.1: Time delay requirement for microwave phased array antennas ( $\Delta h = 2 \text{ mm}$ ,  $h_3 = 5 \text{ mm}$ ). [7]

The measured radiation patterns and corresponding simulation results for  $\alpha = (-45^\circ, 0^\circ, +45^\circ)$  at K-band are shown in Fig. 3.6.2 – 3.6.4. At 18 GHz and 22 GHz, the peaks coincide confirming the beam-squint-free character of the true-time delay modules.

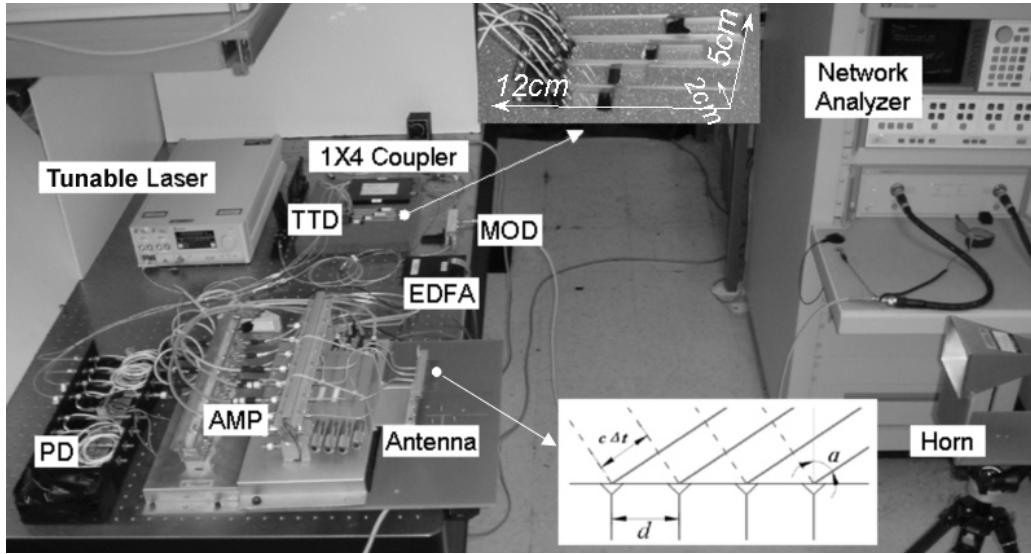


Fig. 3.6.1: A 4-element sub-array antenna system. The insets show the symmetric hologram grating-based true-time delay module and a schematic of the antenna elements, respectively.

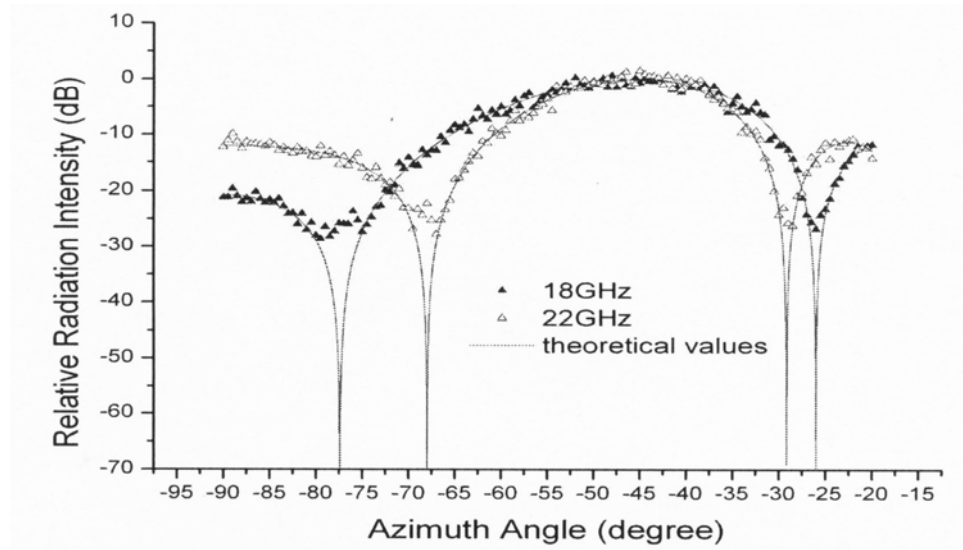


Fig. 3.6.2: Measured and simulated radiation patterns at 18 GHz and 22 GHz with beam steering angle  $\alpha = -45^\circ$ . [7]



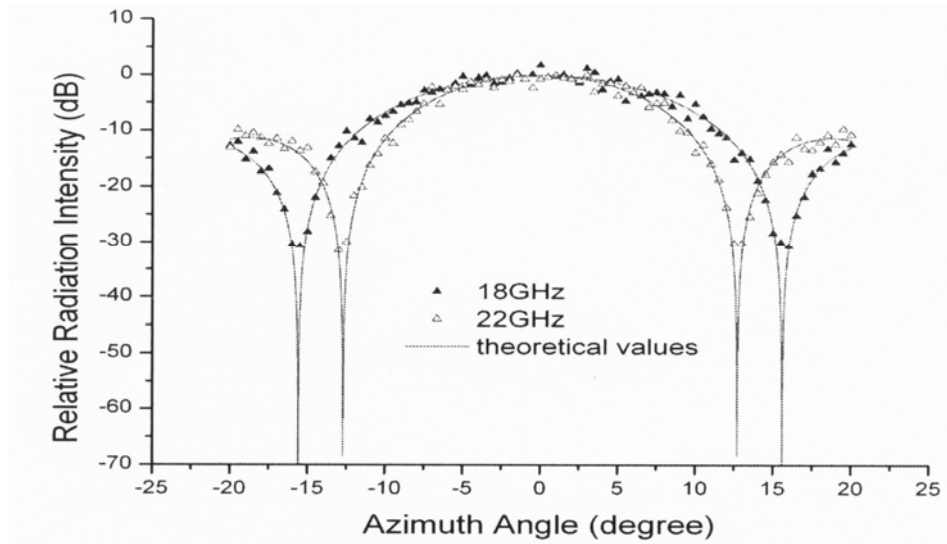


Fig. 3.6.3: Measured and simulated radiation patterns at 18 GHz and 22 GHz with beam steering angle  $\alpha = 0^\circ$ . [7]

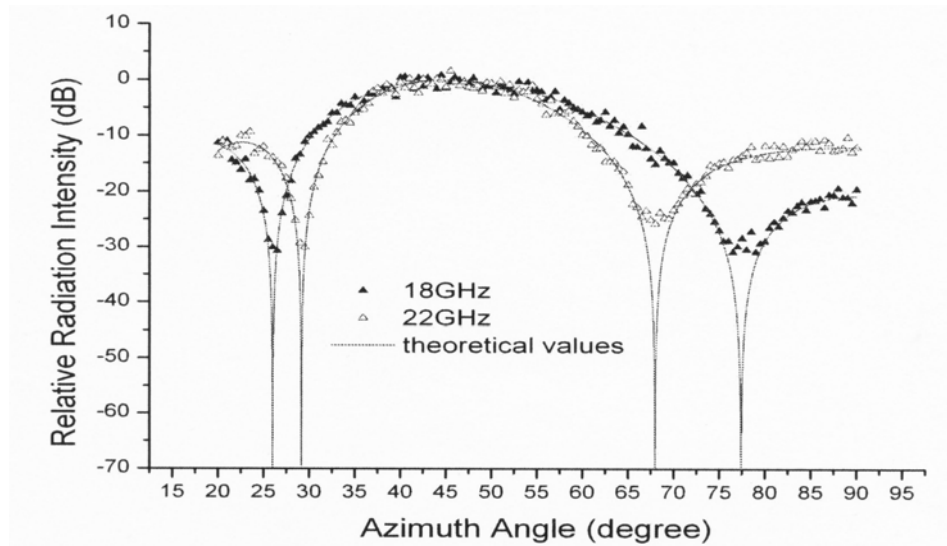


Fig. 3.6.4: Measured and simulated radiation patterns at 18 GHz and 22 GHz with beam steering angle  $\alpha = +45^\circ$ . [7]

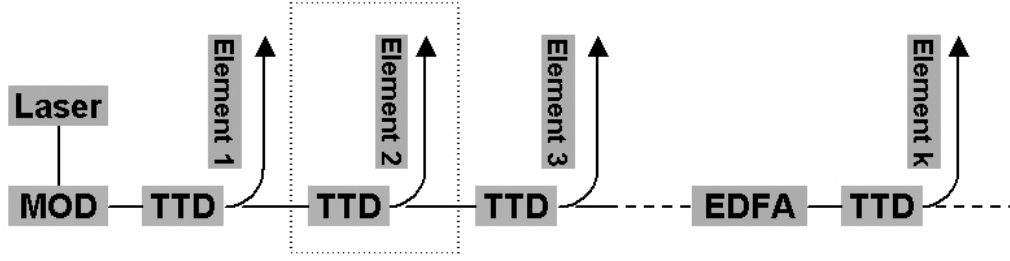


Fig. 3.6.5: Cascaded architecture of delay units for large array antennas. Each delay module provides the required delay difference  $\Delta T_d$  for adjacent antenna elements. [7]

The optical modules proposed in this letter can be cascade-connected to achieve long enough time delay for real-world PAA systems that usually have thousands of elements. The schematic is presented in Fig. 3.6.5. Each delay unit is composed of one delay module and one beam splitter. All delay units are cascade-connected and the output of each splitter is fed into the following delay unit, such that each delay module provides the required delay difference  $\Delta T_d$  for adjacent antenna elements. The splitting ratio of each splitter is designed to achieve equalized output optical power for each antenna element. The wavelength accuracy of the tunable laser (0.001 nm) and the dispersion of delay modules (12.5 ps/nm) determine the delay resolution (0.0125 ps) and beam scanning accuracy ( $0.022^\circ$ ) of the cascaded system.

### 3.7 SUMMARY

A miniaturized, continuously tunable, optical true-time delay module has been fabricated, packaged, evaluated and integrated with a sub-array antenna system. We use a right-angle prism aided structure to record large angle diffraction angle holographic gratings. A novel symmetric structure is introduced to keep the output beam position

fixed and provide doubled maximum achievable time delay. The wavelength dispersion and the time delay formation ability of the fabricated devices are experimentally verified. We also propose a cascaded time delay architecture for the applications of our true-time delay module in large phased-array antenna systems.

*Reference:*

- [1] D. Dolfi, J.P. Huignard, and M. Baril, "Optically controlled true time delays for phased array antenna," *Proc. SPIE*, vol. 1102, pp. 152-161, 1989.
- [2] W. Ng, A. A. Walston, G. L. Tangonan, J. J. Lee, I. L. Newberg, and N. Bernstein, "The first demonstration of an optically steered microwave phased array antenna using true time-delay," *J. Lightwave Technol.*, vol. 9, pp. 1124-1131, Sept. 1991.
- [3] Zhong Shi, Lanlan Gu, Brie Howley, Yongqiang Jiang, QingJun Zhou, Ray Chen, H. R. Fetterman, Charles Lee, George Brost, "True-time-delay modules based on single tunable laser in conjunction with waveguide-hologram for phased array antenna application," *Optical Engineering*, (in press).
- [4] H. Kogelnik, "Coupled wave theory for thick hologram gratings," *Bell Syst. Tech. J.*, vol. 48, pp. 2909-2947, 1969.
- [5] A. M. Weber, W. K. Smothers, T. J. Trout, and D. J. Mickish, "Hologram recording in Du Pont's new photopolymer materials," *Practical Holography IV*, SPIE OE, Laser Conference Proceedings, 1212-04 (1990).
- [6] W. J. Gambogi, W. A. Gerstadt, S. R. Mackara and A. M. Weber, "Holographic transmission elements using improved photopolymer films," *SPIE Computer and Optically Generated Holographic Optics*, 1555, 256-267 (1991).
- [7] Xiaonan Chen, Zhong Shi, Lanlan Gu, Brie Howley, Yongqiang Jiang, and Ray T. Chen, "Miniaturized delay-time-enhanced photopolymer waveguide hologram module for phased-array antenna," *IEEE Photonics Technology Letters*, vol. 17, no. 10, 2182-2184 (2005).

## **Chapter 4: *Silicon photonic crystal waveguide-based optical modulators***

### **4.1 INTRODUCTION**

Silicon, the premium material for the semiconductor industry, has long been excluded from the list of favorable optoelectronic materials owing to some of its intrinsic optical properties. An indirect bandgap results in extremely low radiative recombination efficiency of silicon, which remains the main stumbling block for developing silicon lasers [1]. The intrinsic lattice symmetry prohibits silicon to have second-order optical nonlinearity, which limited the use of silicon in optoelectronic devices such as modulators and switches [2, 3]. Soref and Bennett studied the effect of free carriers in silicon in 1987 [4]. They concluded that the plasma dispersion effect is adequate to produce sufficient change of refractive index with an acceptable optical loss for telecommunication wavelengths. Lorenzo and Soref subsequently demonstrated some switching effect with an integrated silicon device [5]. This opened new avenues to active photonic devices on silicon. However, for over a decade and a half, the speed of silicon modulator never reached the gigahertz mark [6-12], although gigahertz modulation was predicted in a certain resonant structure on silicon [13-14]. The turning point came in 2004 when a research group from Intel abandoned the dominant p-i-n diode configuration for silicon modulators and broke the gigahertz barrier with today's favorite structure for digital electronics: the metal-oxide-semiconductor (MOS) capacitor [15]. In the next year, Lipson's group at Cornell discovered that a p-i-n diode, when integrated into a micro-ring resonator, did have the capability of producing gigahertz modulation [16]. These two milestone works kindled a worldwide pursuit for high speed optoelectronic devices on silicon in the last few years [17-21]. Most recently, Intel reported 30Gb/s transmission through a p-i-n diode modulator [21].

While the speed issue was the major concern in most part of the last two decades, the large size and power consumption of silicon modulators stand out as silicon integrated optoelectronic chips approaches reality. Intel's MOS modulators and p-i-n diode modulators generally require an interaction length of a few millimeters or longer [15, 21]. The ring modulator is capable of delivering high speed with a compact form factor [16]. However, the narrow optical bandwidth of a ring resonator limits its value for high speed applications. In principle, a number of ring modulators can be cascaded to achieve a larger aggregated optical bandwidth, yet the array of rings would occupy a larger area, weakening the size advantage of micro-ring modulators. It also entails engineering issues such as accurate patching in the wavelength domain and the coordination between the cascaded rings under high injection.

#### **4.2 BRIEF REVIEW OF PHOTONIC CRYSTAL WAVEGUIDE MODULATORS**

While the scientific principles of a photonic crystal waveguide modulator have been known since 2002, the design and fabrication of such a modulator proved to be challenging. For a device of any use in communications, high speed modulation well beyond kilohertz is desired. Engineering such a structure requires a combination of the knowledge of the physics and engineering in photonics, electronics, and heat transfer in order to realize its advantages over conventional modulators.

For an optical modulator, the most important performance indexes are modulation depth, optical bandwidth, insertion loss, half-wave voltage  $V_\pi$  (usually measured at DC), electrical bandwidth, driving current or power consumption. In addition, if optical modulators are to be integrated into planar lightwave circuits that can be mass manufactured with today's VLSI technology, the modulator design must be compatible with the prevailing processing and packaging technology. In these regards, the modulator design covers much broader issues beyond the scope of this chapter.

Although it is possible to fabricate a Mach-Zehnder interferometer made of photonic crystal waveguides entirely, such a structure is complicated for a number of reasons. According to the foregoing discussions, the key advantage of introducing photonic crystal waveguides into a Mach-Zehnder modulator is the reduced interaction length, i.e. the length of the waveguide segment that is subject to electrical tuning of the refractive index. As discussed in a later section, it is the interaction length, not the overall length of the MZI, that relates to other critical issues such as voltage, current, and power consumption of a silicon modulator. For initial demonstrations, it is reasonable to use a photonic crystal waveguide only for this electrically controlled segment so as to reduce the design complexity of the device. This idea seems to gain popularity in many early demonstrations [21-23].

One common concern for all photonic crystal waveguide devices is the optical loss. Early demonstrated photonic crystal waveguides suffered high propagation loss in excess of 10 dB/mm. By improving fabrication accuracy and homogeneity, passive photonic crystal waveguides were later demonstrated with low propagation loss, 1.5dB/mm for oxide-clad ones and 0.6dB/mm for air-clad ones [24]. These values are acceptable for many miniaturized photonic crystal waveguide devices including modulators. The short lengths ( $<1$ mm) of photonic crystal waveguides employed in these devices result in a low value of total propagation loss around 1dB. This is also one of the reasons why photonic crystal waveguides were not used to form the entire Mach-Zehnder interferometer in many demonstrated modulators. Direct coupling from a standard telecommunication single-mode fiber to a photonic crystal waveguide may give rise to loss as high as 30dB due to obvious mismatch in mode profiles and effective indices. A mode converter comprising an in-plane adiabatic inverse taper and a core-elevated polymeric waveguide was realized in experiments to lower the coupling loss to 3~4dB

per coupling interface [24]. Detailed characterization of the losses of passive Mach-Zehnder interferometers was also reported [21]. These experiments indicate that with a good mode converter and careful processing, PCW Mach-Zehnder modulators may have an overall insertion loss below 6dB. Further optimization of the coupling structure may help reduce the insertion loss to even lower level.

More critical issues of device physics arise from designing the electrical structure of the modulator. There are many schemes of injecting electrons and holes into such a photonic crystal waveguide. As previously discussed, the early work on silicon modulators highly favored the p-i-n diode configuration whereas the Intel group advanced the MOS capacitor structure. To embed an electrical structure into a photonic crystal waveguide requires thoughtful analysis. Generally, the electrical structures can be divided into two categories, vertical configurations or horizontal configurations.

#### 4.3 BRIEF REVIEW OF DIODE- AND CAPACITOR-BASED SILICON OPTICAL MODULATORS

Here we briefly comment on two structures: a vertical MOS capacitor, and a horizontal pin diode, as depicted in Figs. 4.3.1 and 4.3.2, respectively.

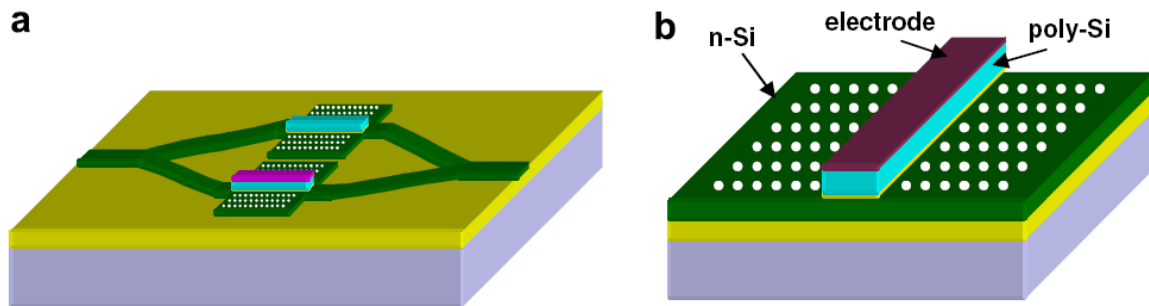


Fig. 4.3.1: electrical structure of a vertical MOS capacitor-embedded PCW Mach-Zehnder modulator. [25]



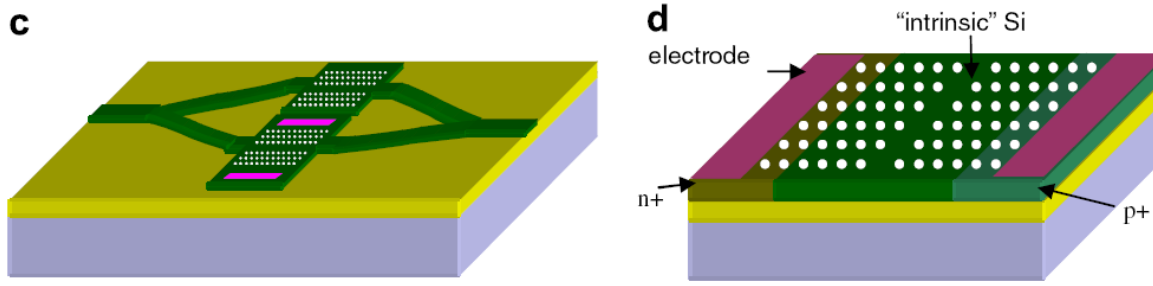


Fig. 4.3.2: electrical structure of a horizontal p-i-n diode-embedded PCW Mach-Zehnder modulator. [25]

The MOS capacitor is a unipolar device. Under accumulation conditions, the fast injection and withdraw of carriers predominates over the slow and weak carrier recombination or generation processes in silicon, thereby providing a fast mechanism for modulating the refractive index of silicon. For the vertical MOS capacitor, the key problem stems from the top electrode. To reduce the optical loss, a thick poly-Si layer must be inserted underneath the top electrode to ensure the tail of the optical mode field is weak enough when it reaches the electrode. Such a thick poly-Si layer causes a W1 waveguide [25] to have multiple modes, which is undesirable for MZI. Although it is possible in principle to reduce the waveguide width and enforce the single mode condition, this generally results in a poly-Si structure with high aspect ratio. Such a structure may cause difficulties in planarization or other processing steps. In addition, the electric current generally flows in the electrode along the longitudinal direction, entering and exiting through the two ends of the metal wire. In such a structure, the effective crosssection for the current flow equals the waveguide width times the metal thickness. As the waveguide width is usually on the submicron scale, the crosssection is too small for a high current to pass through. Note that metal wires can sustain a current density no higher than certain limit due to the electro-migration and other issues [26]. A smaller

current for such a configuration would generally result in low modulation depth. It is possible to design a complicated structure that supplies the carriers into the metal from the sides rather than the two ends. Then the effective cross-section for the electric current in the metal wire becomes equal to the waveguide length times the metal thickness, usually a two-order of magnitude increase. However, the dielectric structure of such a photonic crystal waveguide would be significantly revised from the standard type that has been well documented in literature [24, 21]. Further study is needed in this area.

Horizontal configurations avoid most of the aforementioned problems associated with the vertical configurations and allow us to take advantage of the vast existing knowledge of standard photonic crystal waveguides. The MOS capacitor configuration usually gives to a thin layer of charge carriers that overlap with a very small portion of the optical mode field. This is not conducive to enhancing the interaction between light and electrons. Therefore, we considered the p-i-n diode as the first choice. The p-i-n diode based modulators were considered slower than the MOS based modulators [15]. In most silicon modulators, the carrier generation process has a negligible effect for high speed modulation. The key carrier transport/transition processes that are responsible for producing high speed optical modulation thus include carrier recombination, diffusion, and drift. For moderate to high forward injection levels, the diffusion process provides the main portion of the excess carriers and electric current. Upon a sudden switch to the reverse bias in a modulation cycle, the junction voltage and the internal field remain at relatively small values before the excess carriers stored in the i-region are removed. At this stage, diffusion and recombination are important to expedite the removal of excess carriers in the i-region. Recent simulations and experiments already revealed that the removal of carriers under reverse bias was rapid for compact p-i-n diode modulators whose waveguide cross-sections are less than  $0.5\mu\text{m}\times 0.5\mu\text{m}$  whereas the slow rising time

under forward bias was the primary concern [12, 14, 16]. Finally, we would like to emphasize that a horizontal p-i-n diode is more planarized than a vertical MOS capacitor. The planarization advantage is of critical importance for fabrication and integration of such a modulator with microelectronic circuits, for optical interconnects and other on-chip applications.

#### **4.4 SUMMARY**

We review the basic principles, structural designs, and electrical characteristics of photonic crystal waveguide modulators based on slow light Mach-Zehnder interferometers. A number of structural and electrical configurations of photonic crystal waveguide modulators are discussed. In addition to the advantages associated with the slow group velocity, photonic crystal waveguide modulators are found to exhibit other structural and optoelectronic merits for high speed modulation. We also briefly review past work on silicon modulators and present certain speed scaling of silicon modulators. The scaling is governed by certain intrinsic optoelectronic properties of silicon and fundamental nature of light, and plays a significant role in determining the minimum ac current density and power of silicon modulators as demonstrated in some recent experiments.

*Reference:*

- [1] Pavesi L, Gaponenko S, editors. Towards the first silicon laser (NATO Science Series). Dordrecht, Kluwer, 2003.
- [2] Reed GT, Knights AP. Silicon photonics, an introduction. Chichester, John Wiley, 2004.
- [3] Pavesi L, Lockwood DJ, editors. Silicon photonics. Berlin, Springer, 2004.
- [4] Soref RA, Bennett BR. Electrooptical effects in silicon. IEEE J Quantum Electron 1987,23,123-129.
- [5] Lorenzo JP, Soref RA. 1.3  $\mu\text{m}$  electro-optic silicon switch. Appl Phys Lett 1987,51,6-8.
- [6] Hemenway BR, Solgaard O, Bloom DM. All-silicon integrated optical modulator for 1.3  $\mu\text{m}$  fiber-optic interconnects. Appl Phys Lett 1989,55,349-350.
- [7] Treyz GV, May PG, Halbout J. Silicon Mach-Zehnder waveguide interferometers based on the plasma dispersion effect. Appl Phys Lett 1991, 59,771-3.
- [8] Zhao CZ, Li GZ, Liu EK, Gao Y, Liu XD. Silicon on insulator Mach-Zehnder waveguide interferometers operating at 1.3  $\mu\text{m}$ . Appl Phys Lett 1995,67,2448-2450.
- [9] Tang CK, Reed GT. Highly efficient optical phase modulator in SOI waveguides. Electron Lett 1995,31,451-452.
- [10] Cutolo A, Iodice M, Irace A, Spirito P, Zeni L. An electrically controlled Bragg reflector integrated in a rib silicon on insulator waveguide. Appl Phys Lett 1997, 71,199-201.
- [11] Dainesi P, Kung A, Chabloz M, Lagos A, Fluckiger P, Ionescu A, Fazan P, Declercq M, Renaud P, Robert P. CMOS compatible fully integrated Mach-Zehnder Interferometer in SOI Technology. IEEE Photon Technol Lett 2000,12,660-662.
- [12] Barrios AA, Almeida VR, Lipson M. Low-power-consumption short-length and high-modulation-depth silicon electrooptic modulator. J Lightwave Technol 2003,21,1089-1098.
- [13] Irace A, Breglio G, Cutolo A. All-silicon optoelectronic modulator with 1 GHz switching capability. Electron Lett, 2003,39,232.

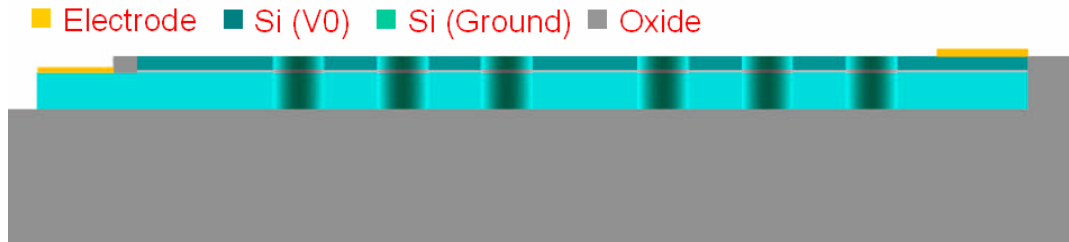
- [14] Barrios CA, Almeida VR, Panepucci RR and Lipson M. Electro-optic modulation of silicon-on-insulator submicron-size waveguide devices IEEE J Lightwave Technol 2003,21,2332.
- [15] Liu A, Jones R, Liao L, Samara-Rubio D, Rubin D, Cohen O, Nicolaescu R, Paniccia M. A high-speed silicon optical modulator based on a metal-oxide-semiconductor capacitor. Nature 2004,427,615-618.
- [16] Xu Q, Schmidt B, Pradhan S, Lipson M. Micrometre-scale silicon electro-optic modulator. Nature 2005,435,325-327.
- [17] Sciuto A, Libertino S, Coffa S, Coppola G. Miniaturizable Si-based electro-optical modulator working at 1.5  $\mu\text{m}$ . Appl Phys Lett 2005,86,201115.
- [18] Kuo YH, Lee YK, Ge K, Ren S, Roth JE, Kamins TI, Miller DAB, Harris JS. Strong quantum-confined Stark effect in germanium quantum-well structures on silicon. Nature 2005,437,1334-1336.
- [19] Liao L, Samara-Rubio D, Morse M, Liu A, Hodge H, Rubin D, Keil UD, Franck T. High-speed silicon Mach-Zehnder modulator. Opt Express 2005,13, 3129-3135.
- [20] Gan F, Kartner FX. High-speed silicon electrooptic modulator design. IEEE Photon Technol Lett 2005,17,1007-1009.
- [21] Liu A, Liao L, Rubin D, Nguyen H, Ciftcioglul B, Chetrit Y, Izhaky N, Paniccia M. High-speed optical modulation based on carrier depletion in a silicon waveguide. Opt Express, 2007, Vol. 15, Issue 2, pp. 660-668.
- [22] Vlasov YA, O'Boyle M, Hamann HF, McNab SJ. Active control of slow light on a chip with photonic crystal waveguides. Nature 2005,438,65-69.
- [23] Jiang Y, Jiang W, Gu L, Chen X, Chen RT. 80-micron interaction length silicon photonic crystal waveguide modulator. Appl Phys Lett, 2005,87,221105.
- [24] Chu T, Yamada H, Ishida S, Arakawa Y. Thermo-optic switch based on photonic-crystal line-defect waveguides. IEEE Photon Technol Lett 2005,17(10) 2083-5.
- [25] Wei Jiang, Lanlan Gu, Xiaonan Chen, and Ray T. Chen, Photonic Crystal Waveguide Modulators for Silicon Photonics: Device Physics and Some Recent Progress, Solid State Electronics, vol. 51, pp. 1278-1286, 2007.
- [26] Gu L, Jiang W, Chen X, Wang L, Chen RT, High-speed silicon photonic crystal waveguide modulator for low-voltage operation. Appl Phys Lett 2007,90,071105.

## **Chapter 5: *High-speed capacitor-based photonic-crystal silicon electro-optic modulators***

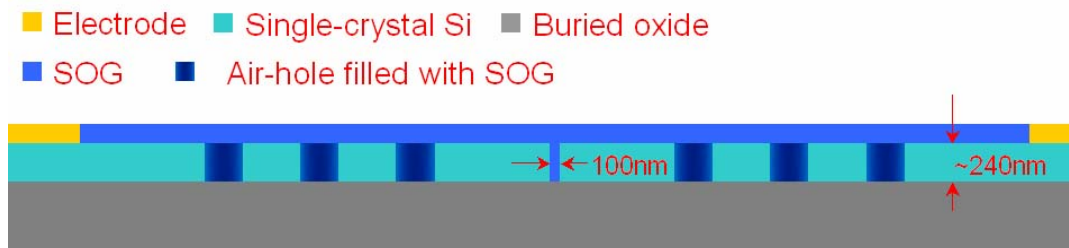
### **5.1 RESEARCH MOTIVATION**

The MOS capacitor is a unipolar device. Under accumulation conditions, the fast injection and withdraw of carriers predominates over the slow and weak carrier recombination or generation processes in silicon, thereby providing a fast mechanism for modulating the refractive index of silicon. For the conventional vertical configuration of a MOS capacitor, shown in Fig. 5.1.1 (a), the key problem stems from the top electrode. To reduce the optical loss, a thick poly-Si layer must be inserted underneath the top electrode to ensure the tail of the optical mode field is weak enough when it reaches the electrode. Such a thick poly-Si layer causes a W1 photonic crystal waveguide [1] to have multiple modes, which is undesirable for MZI. Although it is possible in principle to reduce the waveguide width and enforce the single mode condition, this generally results in a poly-Si structure with high aspect ratio. Such a structure may cause difficulties in planarization or other processing steps. In addition, the electric current generally flows in the electrode along the longitudinal direction, entering and exiting through the two ends of the metal wire. In such a structure, the effective cross section for the current flow equals the waveguide width times the metal thickness. As the waveguide width is usually on the submicron scale, the cross section is too small for a high current to pass through. Note that metal wires can sustain a current density no higher than certain limit due to the electro-migration and other issues. A smaller current for such a configuration would generally result in low modulation depth. It is possible to design a complicated structure that supplies the carriers into the metal from the sides rather than the two ends. Then the effective cross-section for the electric current in the metal wire becomes equal to the waveguide length times the metal thickness, usually a two-order of magnitude increase.

However, the dielectric structure of such a photonic crystal waveguide would be significantly revised from the standard type that has been well documented in literature [1, 2].



(a)



(b)

Fig. 5.1.1: Schematic cross section of the MOS capacitor based photonic crystal modulator in (a) vertical configuration, and (b) horizontal configuration.

Further study is needed in this area. In contrast, the horizontal configuration, shown in Fig. 5.1.1 (b), avoid most of the aforementioned problems associated with the vertical configurations and allow us to take advantage of the vast existing knowledge of standard photonic crystal waveguides. Pros and cons of fabrication techniques for both configurations were discussed in the previous progress report. As a final decision after

thoughtful technical evaluations, the horizontal configuration is selected to develop capacitor based photonic crystal modulators.

## 5.2 PASSIVE WAVEGUIDE COMPONENTS: SLOT PHOTONIC CRYSTAL WAVEGUIDE AND MODE CONVERTER

Slotted photonic crystal waveguide (PCW) is an essential component to construct horizontal capacitor based photonic crystal modulators. A schematic of the slotted waveguiding structure is depicted in Fig. 5.2.1.

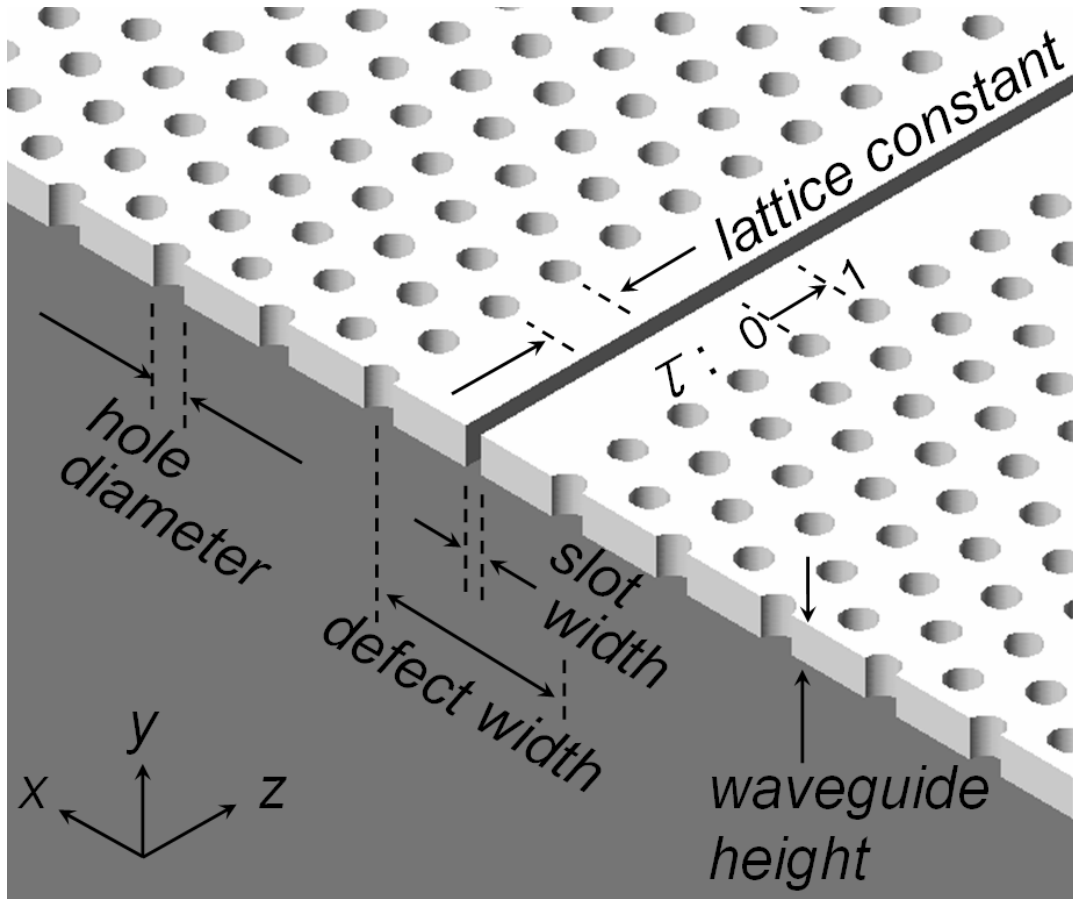


Fig. 5.2.1: Line defect structure with a low-index center slot embedded in a photonic crystal slab.



The slotted photonic crystal slab, with high refractive index  $n_{\text{Si}}=3.48$ , is sandwiched between two low-index regions with  $n_{\text{SiO}_2}=1.46$ . With a high index contrast in the vertical direction, such a photonic crystal waveguide supports an in-plane photonic band gap that lies below the light line [3]. Defect modes within the gap region can be created by a great diversity of line defects [4].

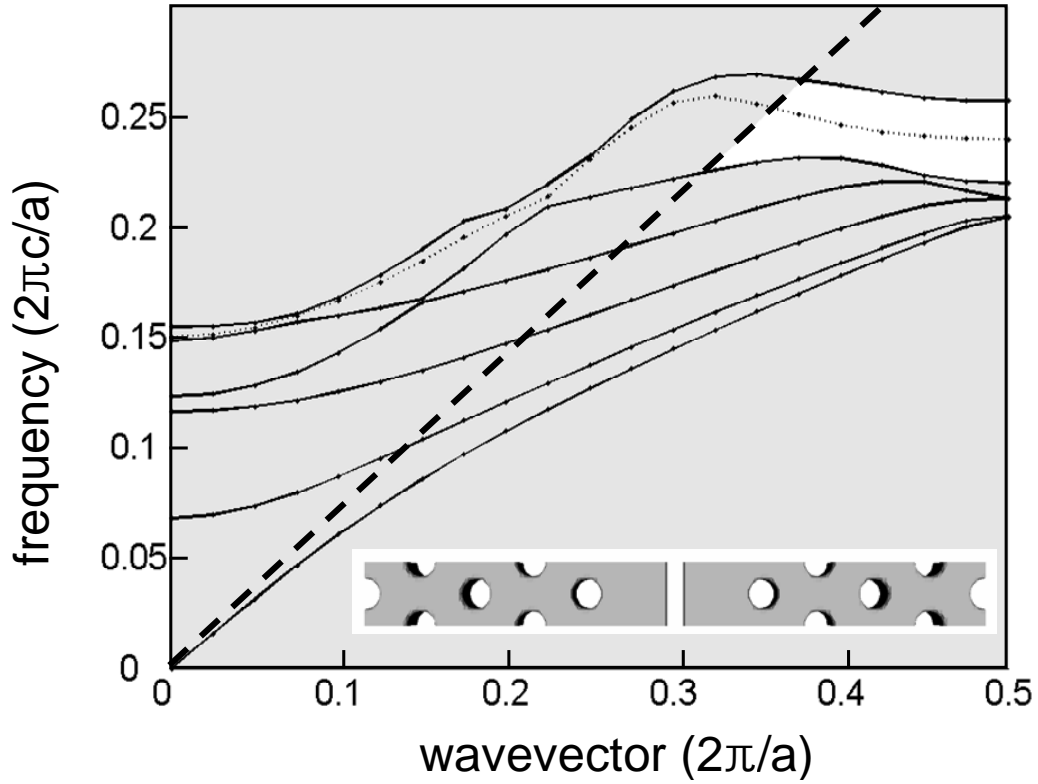


Fig. 5.2.2: Band diagram for a slot photonic crystal waveguide. The thick dashed line is the light line. The gray regions represent the continuum of extended modes. The dotted curve indicates the defect mode. The inset shows the supercell defined in PWE simulation.

Here we introduce the line defect into the photonic crystal slab by replacing a single row of holes with a narrow slot. In addition, we enlarge the width of the defect region to

ensure that the guided mode appears near the mid-gap for robustness against the propagation loss. As a wider defect region may induce multiple bands into the gap region, care must be taken to design the enlarged defect width while maintaining the single-mode operation [5]. We use the 3D fully vectorial plane-wave expansion (PWE) method to calculate the dispersion diagram of the slot PCW. We assume the hole diameter  $d=0.5a$  and the waveguide height  $h=0.6a$ , where  $a=380\text{nm}$  is the lattice constant of the photonic crystal. The dispersion diagram plotted in Fig. 5.2.2 indicates that the slot photonic crystal waveguide retains a single-mode region even when the defect width is enlarged to  $1.6W$ , where  $W = \sqrt{3}a$ , as shown in Fig. 5.2.1. The guided mode is a quasi-transverse electric (TE) mode with slow light effect near the band edge.

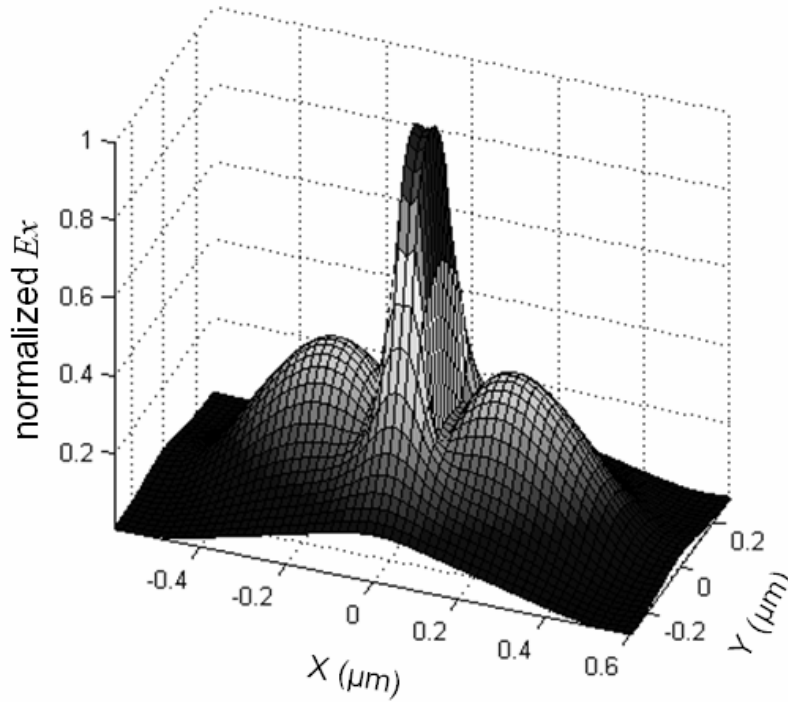


Fig. 5.2.3: 3D profile of the transverse electric field amplitude of the quasi-TE mode in a slot photonic crystal waveguide, where  $a=380\text{nm}$ ,  $d=190\text{nm}$ ,  $h=228\text{nm}$ , slot width= $95\text{nm}$ , defect width= $1053\text{nm}$ ,  $n_{\text{Si}}=3.48$  and  $n_{\text{SLOT}}=n_{\text{SiO}_2}=1.46$ .

Simulation of the mode field of the slot PCW, shown in Fig. 5.2.3, is based on the 3D finite-difference time-domain (FDTD) method. Comparing the mode contour plot of a slot PCW with that of a single-mode silicon strip waveguide in Fig. 5.2.4, one can identify the evident mode-size and mode-shape mismatch, which will induce significant loss for direct coupling. A conventional solution would be to introduce waveguide taper structures. However, a taper structure generally requires a taper length of more than several hundred of microns to reduce the propagation loss due to the requirement of adiabatic tapering. In order to implement a more compact mode converter, we integrate multimode interference-based coupling structures in our devices. The basic idea stems from the multimode power splitter structure that has been used to achieve equi-phase, balanced power partition from one single-mode input waveguide [6].

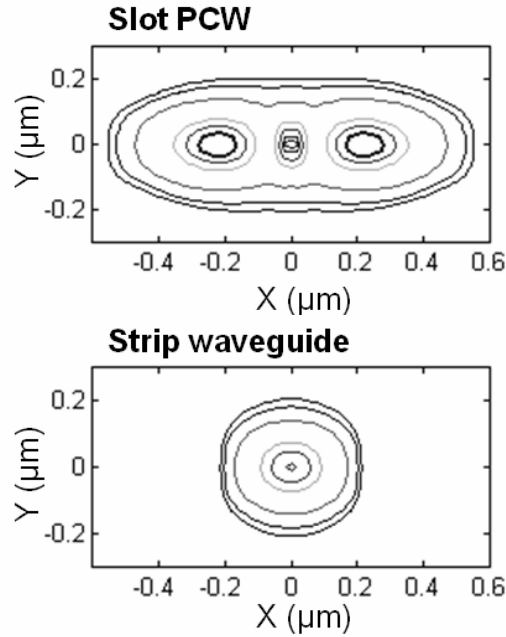


Fig. 5.2.4: Comparison of 2D field amplitude contours between a slot PCW and a single-mode strip waveguide.

A schematic of the multimode interference coupler bridging a strip waveguide and a slot PCW is delineated in the inset of Fig. 5.2.5. The multimode section is designed to support two even (symmetric) modes with  $W_M=1.6W$ . The single-mode input waveguide is centered with respect to the multimode section and therefore excites only the symmetric modes.

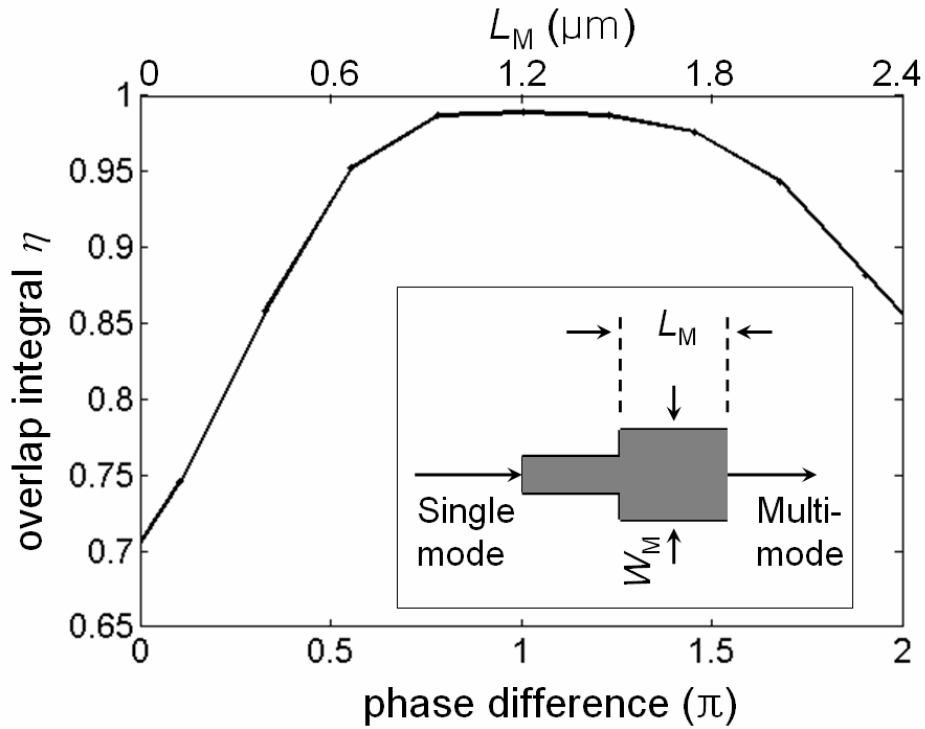


Fig. 5.2.5: Optimization of the mode overlapping integral between the slot PCW and the multimode section. The integral is calculated as a function of the length of the multimode section or the phase difference of the excited even modes.

According to the principle of symmetric modal interference in a multimode waveguide, the input mode excites the fundamental and second-order modes with disparate propagation constants; the total field profile is composed of the fundamental

mode plus the second-order mode shifted by a certain phase difference. The phase difference is given by  $\Delta\Phi=(\beta_0-\beta_2)L_M$ , where  $L_M$  is the length of the multimode section and  $\beta_0$  and  $\beta_2$  are the propagation constants of the fundamental and second-order modes in the multimode waveguide, respectively. We can therefore adjust  $L_M$  to change the phase difference between 0 and  $2\pi$  such that the resultant mode profile can best match the slot PCW. With different  $L_M$  the coupling efficiency  $\eta$  is computed by using the overlap integral between the output field of the multimode section and the guided mode of the slot PCW. As shown in Fig. 5.2.5, the best coupling efficiency is reached when the phase difference of the even modes in the multimode section is close to  $\pi$ .

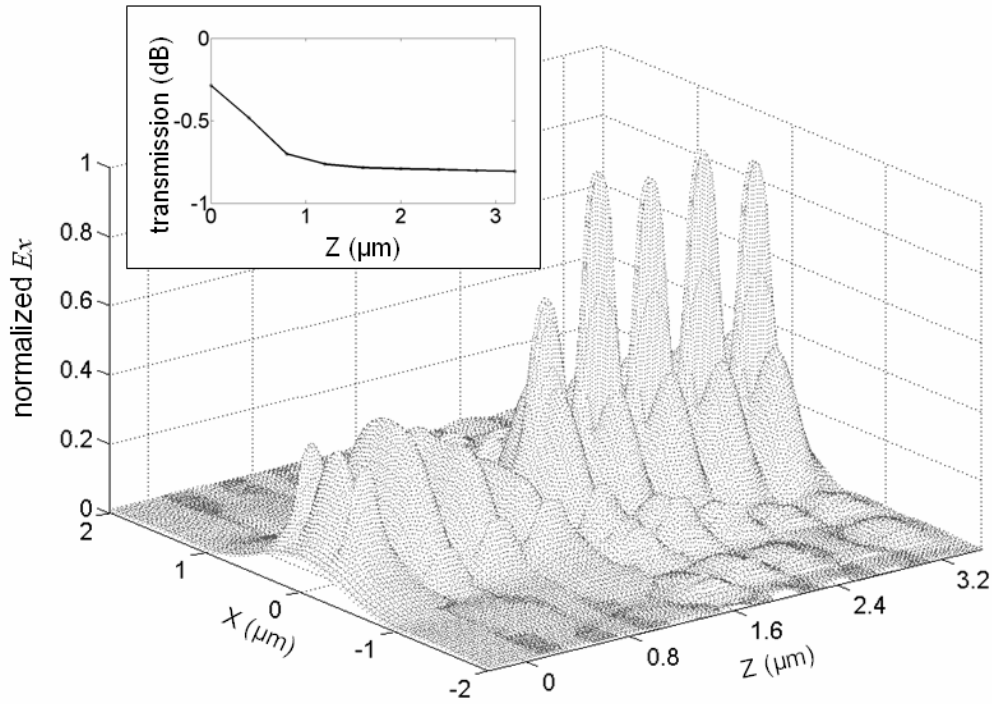


Fig. 5.2.6: FDTD Simulation results: A series of  $|E_x(x,y)|$  profiles on the X-Y plane imaged at different  $Z$  positions. The MMI coupler begins at  $Z=0\mu\text{m}$  and ends at  $Z=1.25\mu\text{m}$ . The inset shows the transmission of the guided quasi-TE mode as a function of the propagation distance.

It has been reported that the coupling efficiency for a PCW also depends on the termination of the photonic crystal waveguide [7]. We simulate the coupling structure with different PCW terminations and the best outcome is obtained when the MMI section interfaces with the slot PCW at the edge of the period which gives termination parameter  $\tau=0$  as also indicated in Fig. 5.2.1. The simulation is based on the 3D FDTD method. Fig. 5.2.6 depicts the evolution of the transverse electric field and optical transmission along the propagation direction. The multimode interference coupler is located between  $Z=0\mu\text{m}$  and  $Z=1.25\mu\text{m}$ . An efficient mode conversion from the conventional silicon strip waveguide to the slot PCW is completed within a  $3\text{-}\mu\text{m}$  distance. The FDTD simulation confirms the total insertion loss induced by mode conversion is less than 1dB.

### **5.3 PASSIVE WAVEGUIDE COMPONENTS: DEVICE FABRICATION AND CHARACTERIZATION**

Slot photonic crystal waveguides with multimode interference couplers are fabricated on a silicon-on-insulator (SOI) wafer with a  $1\text{-}\mu\text{m}$  buried oxide layer and a 250-nm top silicon layer. The slot nanostructures are formed in a hexagonal lattice photonic crystal slab with  $a=380\text{nm}$  and the hole diameter  $d=0.5a$ . The lattice constant is designed to ensure that the guided mode of the waveguide appears around  $1.55\text{ }\mu\text{m}$ . The waveguide slab layer is patterned using electron-beam lithography followed by reactive ion etching (RIE) and piranha cleaning. The air holes and the center trench are then filled with spin-on-glass (SOG). The sample with coated SOG on top is postbaked at  $425^\circ\text{C}$  for 1 hour for decarbonization. The refractive index of SOG after hard baking is  $n_{\text{SOG}}=1.42$ , which is close to the value of low-index EO polymers. Figure 5.3.1 shows a top view of the slot photonic crystal waveguide before filling SOG. The parameters of the waveguide are measured to be  $a=383\text{nm}$ ,  $d=207\text{nm}$ ,  $W_{\text{SLOT}}=97\text{nm}$ ,  $W_{\text{STRIP}}=486\text{nm}$ ,  $W_{\text{M}}=1048\text{nm}$ ,  $L_{\text{M}}=1260\text{nm}$ , and  $h=237\text{nm}$  as indicated in Fig. 5.3.2.

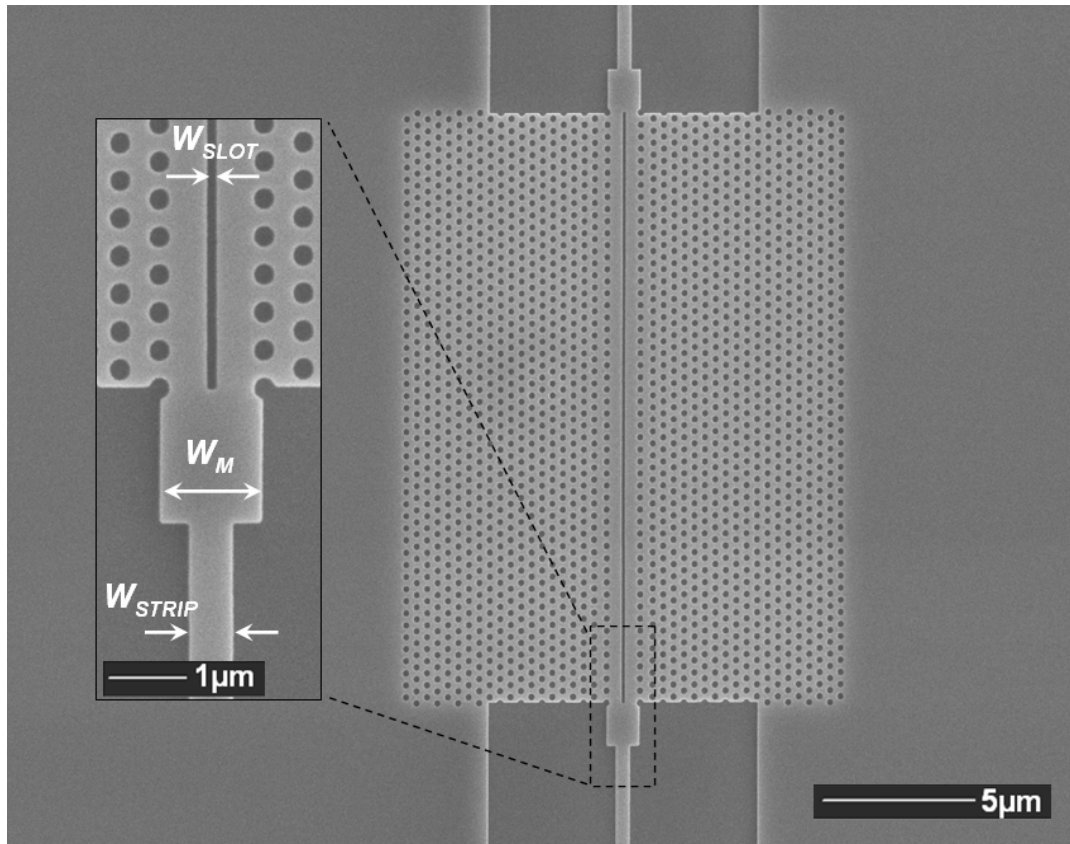


Fig. 5.3.1: Top-view SEM picture of a slot PCW integrated with two multimode interference couplers.

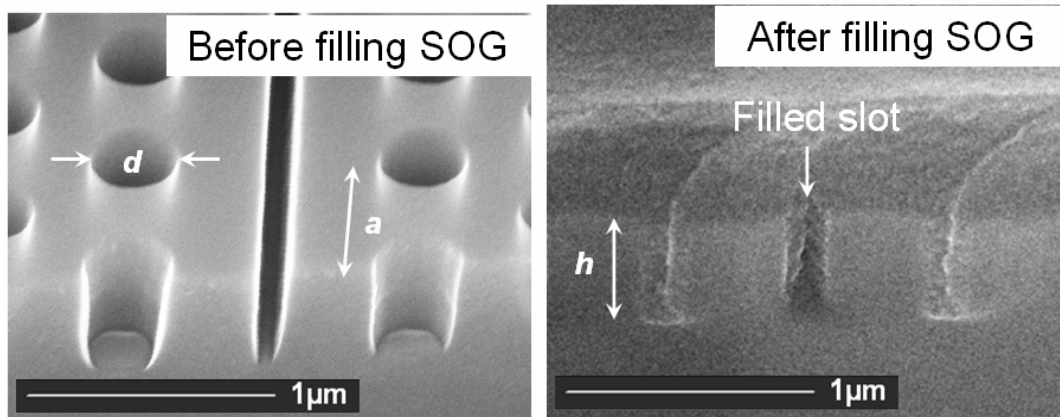


Fig. 5.3.2: Cross-section views of the slot PCW before and after filling SOG.

A cross-section view of the waveguide structure shown in Fig. 5.3.2 confirms that all the void nanostructures in the waveguide slab layer have been filled with SOG. As the last step, an acrylic-based polymer layer that is transparent at  $1.55\ \mu\text{m}$  is coated to reduce the propagation loss due to surface roughness.

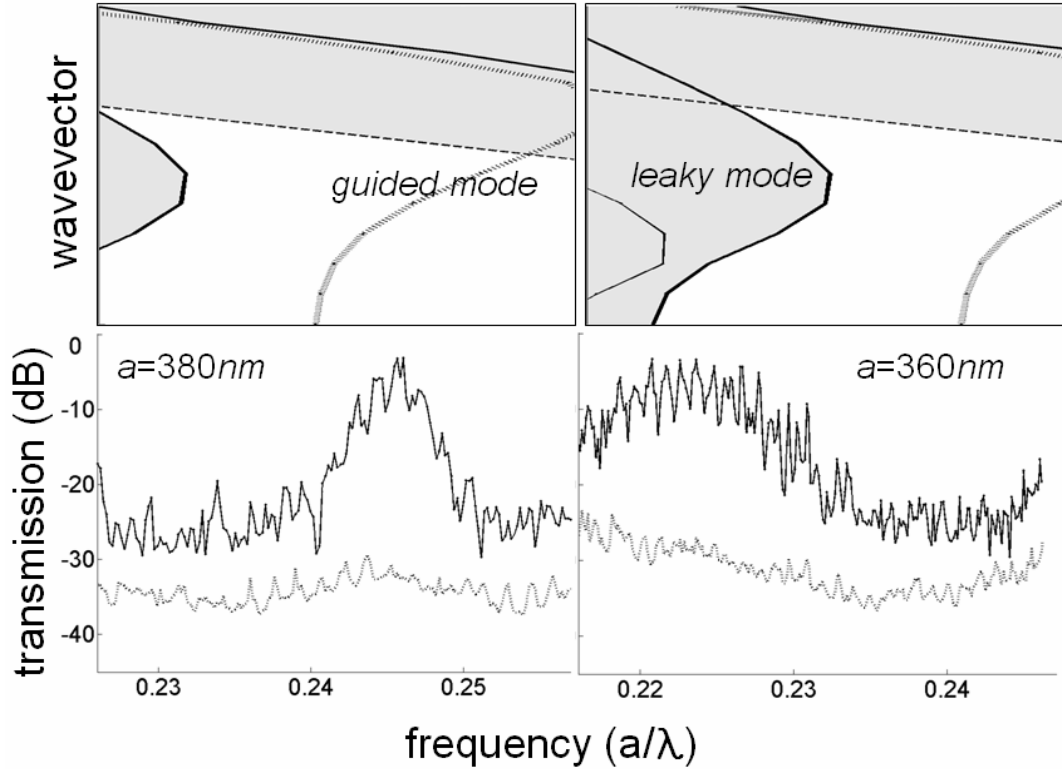


Fig. 5.3.3: Top panel: Enlarged portions of the photonic band structure for both guided and leaky modes. Bottom panel: transmission spectrum of the slot PCW of  $320\mu\text{m}$  length with (solid) and without (dashed) coupling structures. The spectrum is normalized on transmission through a reference optical circuit.

To experimentally measure the insertion loss induced by mode mismatch, we integrate a symmetric  $1\times 2$  power splitter before the slot PCW and introduce a reference arm composed of a strip waveguide to normalize the output of the slot PCW arm. Two



samples are fabricated: one sample has MMI couplers at the ends of the slot PCW, the other has the slot PCW directly coupled to the stripe waveguides. The length of the slot photonic crystal waveguides in both cases is 320 $\mu$ m. The measured optical spectra are shown in Fig. 5.3.3. Compared with direct coupling, one can find a 20dB transmission enhancement over 35nm optical bandwidth when the coupling structure is employed. The insertion loss for the guided mode is less than 5dB at the peak wavelength of 1557nm. The measured band edge appears at a normalized frequency of 0.243 ( $\lambda$ =1576nm). The observed spectral range agrees well with the calculated band diagram for the quasi-TE mode of the slot photonic crystal waveguide. The slight frequency discrepancy can be attributed to the dimension and index difference between the simulated and fabricated waveguide structures.

#### **5.4 ACTIVE WAVEGUIDE COMPONENTS: DEVICE OPTICAL AND ELECTRICAL DESIGN**

Silicon electro-optic (EO) modulators in highly-integrated on-chip systems always require an optimum design with low power consumption for both static and dynamic operations. In conventional silicon modulators based on Mach-Zehnder interferometers (MZI), the power consumption can heat up the local waveguide area and thus induce a positive refractive index perturbation of the active arm due to the silicon thermo-optic (TO) effect. [8] On the other hand, during carrier injection the free carrier EO effect always provides a negative index perturbation in the silicon region, [9] meaning that the modulation efficiency is degraded by the TO effect. The operation power is more critical for PCW-based interference modulators because the slow light effect makes PCW more sensitive to the index perturbation than conventional waveguides. It has been demonstrated that, using an interference based PCW configuration, either EO or TO effect can turn the light off with tens of mw switching power applied. [10,11] Therefore care must be taken to design a PCW-based silicon EO

modulator with lower DC and RF power consumption in order to minimize the adverse impact due to the TO effect.

It has been reported that the minimum bias power achieved for switching the optical transmission from ON to OFF in a p-i-n diode modulator is at the order of 100  $\mu$ W, and that the RF power for gigahertz switching is higher than 5pJ/bit, i.e. 50 mW at 10 GHz, due to the fact that the carriers are injected or extracted more frequently. [12] In contrast, the DC power consumption of a capacitor modulator mainly depends on the leakage current due to the band-to-band direct tunneling or Fowler-Nordheim tunneling. [13] The leakage current density can be controlled well below  $10^{-5} \text{ A/cm}^2$  through an optimized fabrication procedure. Therefore the capacitor modulator is generally considered to have zero power consumption with negligible TO effect induced by DC bias voltage. The RF power required by a capacitor modulator depends on the AC power consumption of a resistor-capacitor series network, which is given by  $P_{AC} = CV^2 / 2 / bit$ , [14] where V is the voltage amplitude of a RF pulse signal. We may design a capacitor modulator with either small capacitance or ultra-low driving voltage in order to minimize the AC power consumption. For highly-integrated interconnect systems, where a large modulator array dominates the total power consumption, small capacitance is more desired because ultra-low voltage operation is more susceptible to the electrical noise coupling by capacitive and inductive mechanisms. [15] Photonic crystal based structures are capable of shrinking the device interaction length to hundreds of microns and the device height to hundreds of nanometers, [16] which scales down the dielectric area of the lateral capacitor in a slotted waveguide and thereby significantly reduces the overall capacitance.

The silicon modulator presented here is a MZI based on lateral capacitor-embedded PCW, as shown in Fig. 5.4.1. The waveguide comprises a p-type doped silicon

photonic crystal slab with a center slot working as the vertical gate oxide. Under accumulation conditions ( $V > 0$ ), the majority carriers in the right silicon region modify the refractive index so that phase shift is induced in the optical mode. Compared with conventional capacitor-embedded silicon rib waveguides, [17] the optical mode is more tightly confined within  $1\ \mu\text{m}$  distance perpendicular to the gate dielectric and thus interacts more strongly with the accumulated charges.

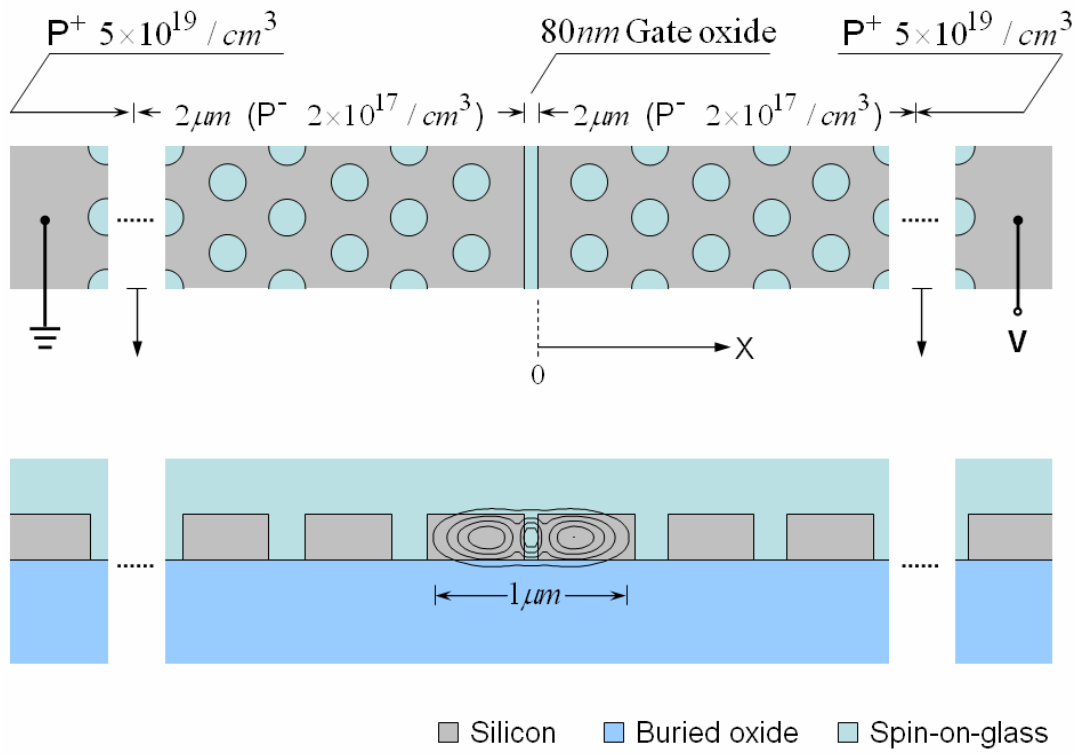


Fig. 5.4.1: Schematic diagrams: top and cross-sectional views of a lateral capacitor-embedded photonic crystal waveguide. The cross-sectional view shows the simulated two-dimensional field amplitude contour.

For accurate understanding of the carrier distribution, which determines the refractive index perturbation in the silicon waveguide, the Poisson equation is solved by applying classical model. [18] The charge distribution is given by, [18]

$$p(x) = N_A \exp\left[-\frac{q\psi(x)}{kT}\right], \quad \psi(x) = -\frac{kT}{q} \ln\left(\sec^2\left\{\cos^{-1}\left[\exp\left(\frac{q\psi_s}{2kT}\right)\right] - \frac{x}{\sqrt{2}L_D}\right\}\right),$$

where  $N_A$  is the p-type doping concentration,  $\psi_s$  is the surface potential at  $x=0$ , and  $L_D$  is the extrinsic Debye length for holes. We further relate  $\psi_s$  with the driving voltage by involving the  $Q_s(\psi_s)$  function, [18] where  $Q_s$  is the total space charge in the silicon region. The voltage drop due to carrier depletion in the left region is also considered when deriving  $\psi_s$ .

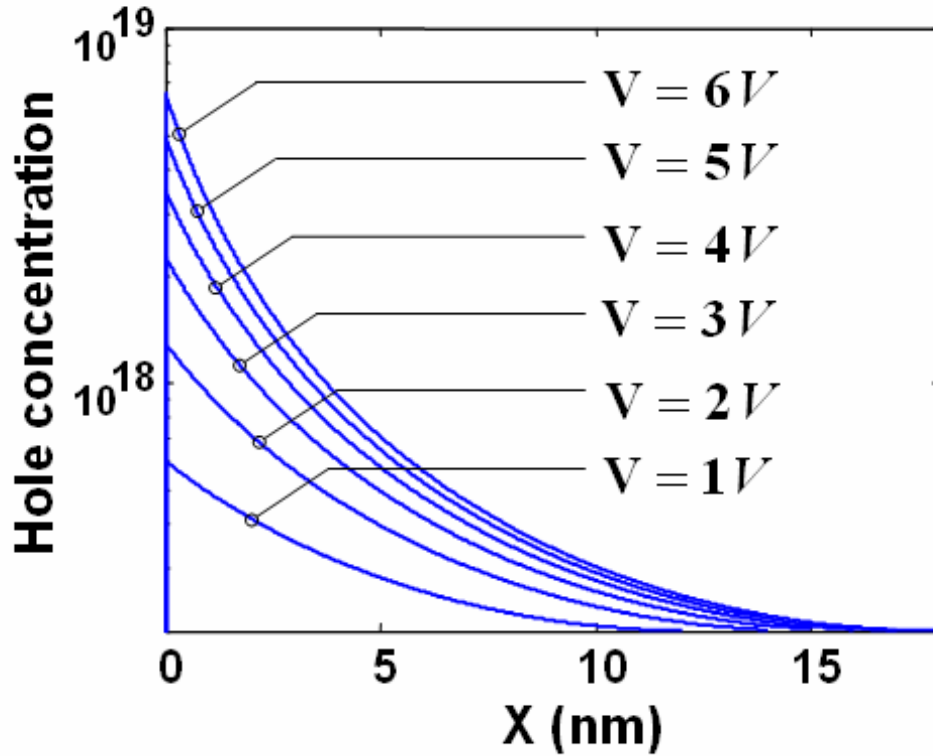


Fig. 5.4.2: Calculated profiles of the hole carriers.

The calculated profile of the hole carriers under different driving voltages is shown in Fig. 5.4.2. Each profile is converted into the index change through an empirical equation  $\Delta n_h = -8.5 \times 10^{-18} (p - p_0)^{0.8}$ , [9] as shown in Fig. 5.4.3. We use the plane-wave expansion method to calculate the dispersion diagram of the slot PCW with different index perturbations and derive the phase shift by  $\Delta\phi_{\text{PC}} = \Delta\omega_0 L / v_g$ , where  $\Delta\omega_0$  is the vertical shift of the dispersion curve. [19] Calculation indicates that the slot PCW-based active arm, designed to give  $v_g = c/100$  with 300  $\mu\text{m}$  interaction length required for inducing  $\pi$  phase shift, composes a compact capacitor-embedded silicon modulator with a  $V_\pi L$  product of 0.18 Vcm.

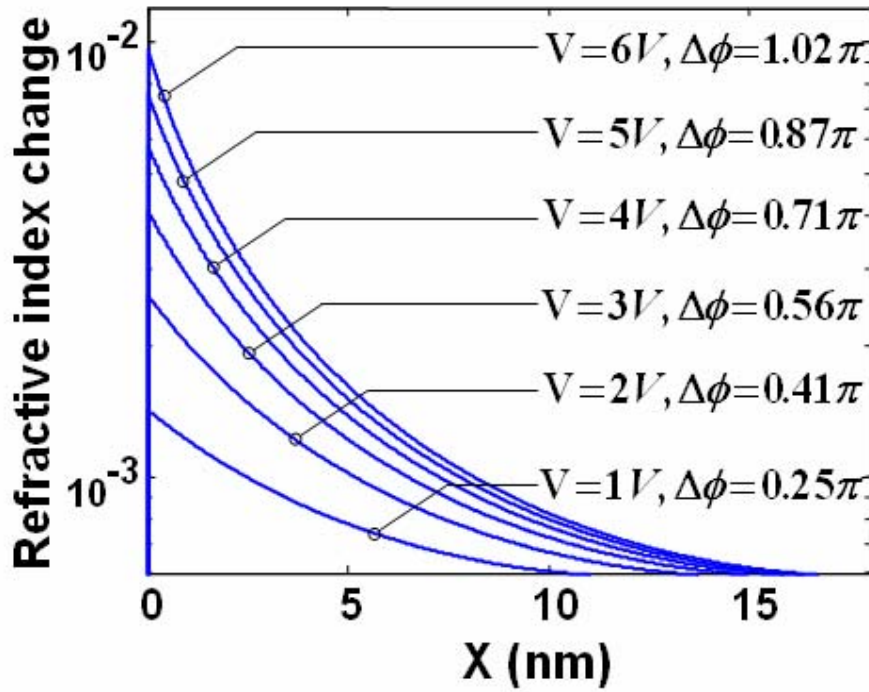


Fig. 5.4.3: Calculated profiles of the refractive index changes under different driving voltages.

## 5.5 ACTIVE WAVEGUIDE COMPONENTS: DEVICE FABRICATION AND CHARACTERIZATION

The capacitor-embedded PCW MZI modulator is fabricated on a silicon-on-insulator wafer with a 250 nm top silicon layer. The slot nanostructures are formed in a hexagonal lattice photonic crystal slab with the lattice constant  $a=400$  nm and the hole diameter  $d=220$  nm. The waveguide slab layer is patterned by electron-beam lithography and reactive ion etching, followed by growing thin thermal oxide up to 10 nm for surface passivation.  $p^-$  and  $p^+$  regions are defined using photolithography and implanted to the concentration  $N_A(p^-)=2\times 10^{17} cm^{-3}$  and  $N_A(p^+)=5\times 10^{19} cm^{-3}$  respectively. The contact windows are opened by a third photolithography process, and aluminum electrodes are formed by a lift-off process. As the last step, we fill the air holes and the center slot with spin-on-glass (SOG), and postbake the sample at 425°C for decarbonization. An image of the resulting device is shown in Fig. 5.5.1. A tapering mode coupler with a skew slot [20] is integrated at both ends of the slot PCW in order to relieve the mode mismatch with the strip waveguide and maintain the electrical isolation between the two regions separated by the slot. A dummy sample without the center slot is also fabricated to measure the equivalent series resistance. The total resistance between adjacent electrodes is about 120  $\Omega$ , dominated by the resistance of the lightly-doped silicon region. The flat-band capacitance of the real device is measured by a HP 4194A impedance analyzer. The compact waveguide design with the lateral capacitor layout, provides significant reduction of the total capacitance from the conventional rib waveguide modulators, [17, 21] pushing it down to 30 fF. Combined with the 120  $\Omega$  series resistance, the RC network has a time constant of 23 ps, which allows for an intrinsic switching bandwidth above 40 GHz.

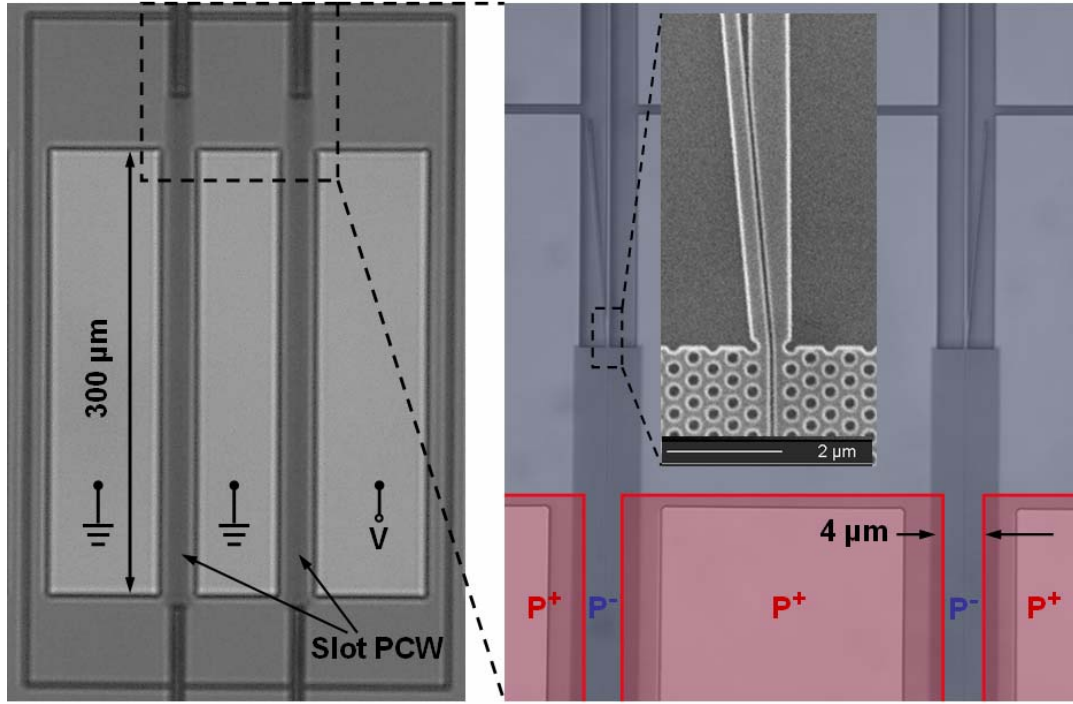


Fig. 5.5.1: Images of the fabricated device. Microscopic image of a capacitor-embedded photonic crystal Mach-Zehnder interferometer, where colored overlays indicate the  $p^-$  and  $p^+$  regions. The inset is a scanning electron microscopy image of one end of the slot photonic crystal waveguide.

The DC characterization of the capacitor-based MZI modulator is performed on a Newport photonic alignment station. The set-up of optical measurement is shown in Fig. 5.5.2. We electrically connect the active device using a high-speed contact probe. Transverse electric polarized light at a wavelength of 1548 nm is used for optical measurement. As shown in Fig. 5.5.3, a maximum modulation depth of 90% is obtained at 6 V DC bias voltage. The leakage current during operation is below 200 pA, which indicates negligible DC power consumption  $P_{DC} = 1.2 \text{ nW}$ .

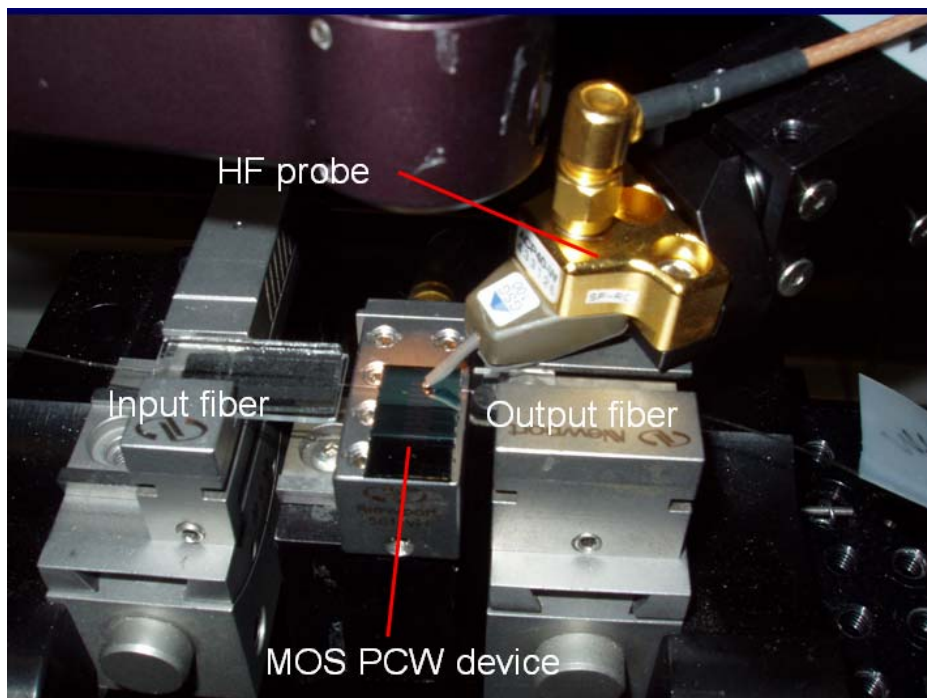


Fig. 5.5.2: The set-up of optical measurements.



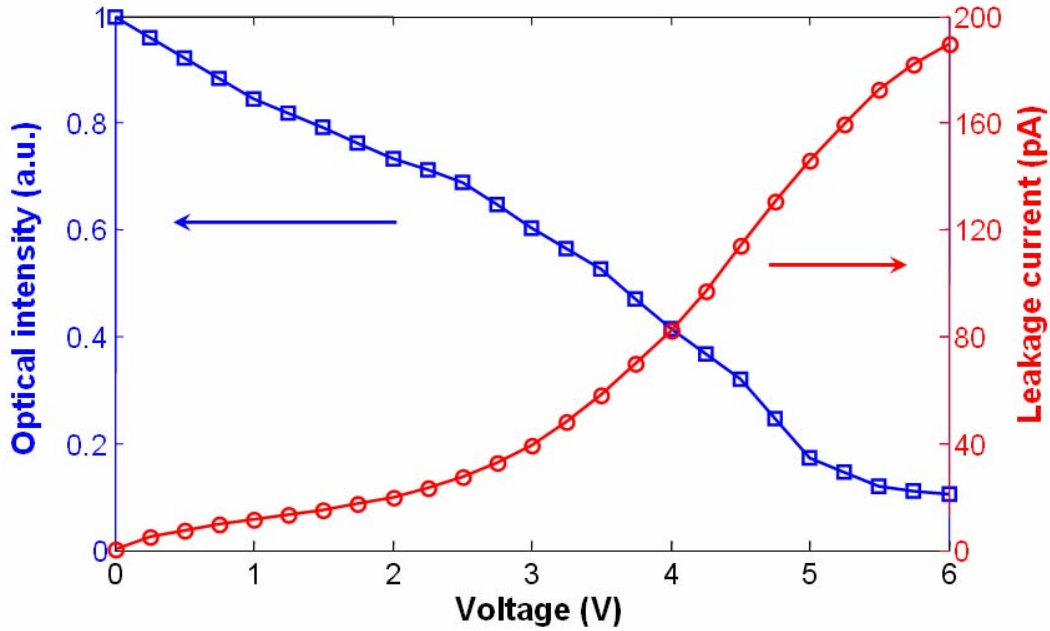


Fig. 5.5.3: The optical intensity at the modulator output and the leakage current as a function of the static driving voltage.

It is measured that total optical insertion loss of the modulator is approximately -40 dB fiber to fiber, dominated by the fiber-to-strip-waveguide coupling (-13~-15 dB/port) and the strip-waveguide-to-PCW coupling (-5 dB/port at  $v_g = c/100$ ). It has been reported that the strip-waveguide-to-PCW coupling efficiency  $T$  is a function of the group velocity  $v_g$  as  $T = 3.22(c/v_g)^{-0.74}$ . [16] We make a trade-off between  $v_g$  and  $T$  in order to obtain higher output intensity so that the high speed photodetector provides gigahertz response. The light wavelength is tuned to 1551 nm to control the group velocity around  $v_g = c/50$ . A square wave electrical signal having a peak-to-peak amplitude of 6 V and a duty cycle of 50% is used for high frequency modulation characterization. The output optical intensity of the modulator at the bit rate of 1.6 Gbit/s is shown in Fig. 5.5.4. As a critical characteristic, the RF power consumption, given by

$P_{AC} = CV^2 / 2/bit$ , is reduced to 0.54 pJ/bit, which is one of the lowest values for any high speed silicon modulator obtained to date. The high frequency modulation depth is limited by reduction of the group velocity and degradation of the detector bandwidth due to low optical intensity. The fiber-to-strip-waveguide coupling can be improved by introducing inverse taper structures, [22] which provides a solution to further reduce the total insertion loss of the modulator.

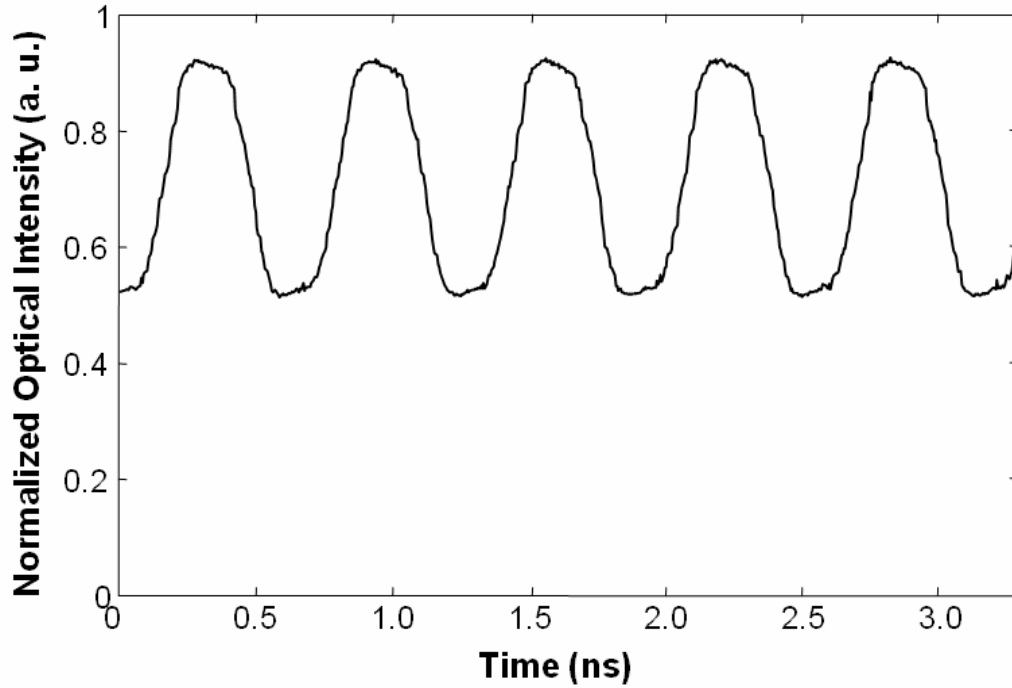


Fig. 5.5.4: The normalized output optical intensities of the modulator working at 1.6 Gbit /s.

## 5.6 SUMMARY

In this chapter, the design, fabrication and characterization of a capacitor-based photonic crystal silicon modulator, which operates in the GHz region, is presented. The

incorporation of photonic crystal waveguides into a Mach-Zehnder interferometer enables a significant reduction in device interaction length. The physical mechanism of such an ultra-compact and high-speed device has been analyzed. Optical simulation using the plane wave expansion method has been performed to study the slow group velocity of the photonic crystal waveguide. To provide a guideline for the geometry design of the embedded capacitor, optical mode profile of the photonic crystal waveguide was simulated. The classical model has been employed to investigate the electrical performance of our devices. The voltage-dependent carrier accumulation of the embedded capacitor was theoretically analyzed. The improvement in device power consumption was experimental confirmed. High-speed optical modulation at 1.6 Gbit/s of the same device has been experimentally demonstrated. We believe the small RF power consumption of 0.54 pJ/bit is one of the lowest values for any high speed silicon modulator obtained to date. Furthermore, the feasibility of demonstrating even higher modulation speed up to 40 GHz in an optimized device has been theoretically proven.

*Reference:*

- [1] M. Notomi, K. Yamada, A. Shinya, J. Takahashi, C. Takahashi, and I. Yokohama, "Extremely Large Group-Velocity Dispersion of Line-defect Waveguides in Photonic Crystal Slabs," *Phys. Rev. Lett.*, 87, pp. 253902-1-253902-4 (2001).
- [2] Y. A. Vlasov, Martin O'Boyle, Hendrik F. Hamann, and S. J. McNab, "Active control of slow light on a chip with photonic crystal waveguides," *Nature*, 438, 65-69 (2005).
- [3] E. Chow, S. Y. Lin, S. G. Johnson, P. R. Villeneuve, J. D. Joannopoulos, J.-R. Wendt, G. A. Vawter, W. Zubrzycki, H. Hou, and A. Alleman, "Three-dimensional control of light in a two-dimensional photonic crystal slab," *Nature (London)* 407, 983 (2000).
- [4] S. G. Jonson, P. R. Villeneuve, S. Fan, and J. D. Joannopoulos, "Linear waveguides in photonic-crystal slabs," *Phys. Rev. B* 62, 8212 (2000).
- [5] Z. Y. Li, L. L. Lin and K. M. Ho, "Light coupling with multimode photonic crystal waveguides," *Appl. Phys. Lett.* 84, 4699 (2004).
- [6] L. B. Soldano and E. C. Pennings, "Optical multimode interference devices based on self-imaging-principles and applications," *J. Lightwave Technol.* 13, 615 (1995).
- [7] Y. A. Vlasov, S. J. McNab, "Coupling into the slow light mode in slab-type photonic crystal waveguides," *Opt. Lett.* 31, 50 (2006).
- [8] G. Cocorullo, F. G. Della Corte, and I. Rendina, "Temperature dependence of the thermo-optic coefficient in crystalline silicon between room temperature and 550 K at the wavelength of 1523 nm," *Appl. Phys. Lett.* 74, 3338 (1999).
- [9] R. A. Soref and B. R. Bennett, "Electrooptical effects in silicon," *IEEE J. Quantum Electron.* 23, 123 (1987).
- [10] Q. Xu, S. Manipatruni, B. Schmidt, J. Shakya, and M. Lipson, "12.5 Gbit/s carrier-injection-based silicon micro-ring silicon modulators," *Opt. Express* 15, 430 (2007).
- [11] L. Gu, W. Jiang, X. Chen, and R. T. Chen, "Thermooptically Tuned Photonic Crystal Waveguide Silicon-on-Insulator Mach-Zehnder Interferometers," *IEEE Photonics Technol. Lett.* 19, 342 (2007).
- [12] William M. J. Green, Michael J. Rooks, Lidija Sekaric, and Yurii A. Vlasov, "Optical modulation using anti-crossing between paired amplitude and phase resonators," *Opt. Express* 15, 17107, (2007).

- [13] B. G. Streetman and S. Banerjee, Solid State Electronic Devices (Prentice-Hall, Upper Saddle River, NJ, 2000), p. 291.
- [14] A. Agarwal and J. H. Lang, Foundations of Analog and Digital Electronic Circuits, 1st ed. (Morgan Kaufmann, 2005), p. 596.
- [15] S. H. Choi and K. Roy, "Noise analysis under capacitive and inductive coupling for high speed circuits," Proceedings of the 1st IEEE International Workshop on Electronic Design, Test and Applications (DELTA'02), p. 365.
- [16] Y. A. Vlasov, M. O'Boyle, H. F. Hamann, and S. J. McNab, "Active control of slow light on a chip with photonic crystal waveguides," Nature (London) 438, 65 (2005).
- [17] L. Liao, D. Samara-Rubio, M. Morse, A. Liu, D. Hodge, D. Rubin, U. D. Keil, and T. Franck, "High speed silicon Mach-Zehnder modulator," Opt. Express 13, 3129 (2005).
- [18] S. M. Sze and K. K. Ng, Physics of Semiconductor Devices, 3rd ed. (Wiley, New York, 2007), p. 233.
- [19] Y. Jiang, W. Jiang, L. Gu, X. Chen, and R. T. Chen, "80-micron interaction length silicon photonic crystal waveguide modulator," Appl. Phys. Lett. 87, 221105 (2005).
- [20] J. Blasco and C.A. Barrios, "Compact slot-waveguide/channel-waveguide mode-converter," Proceedings of the CLEO Europe'05, p. 607.
- [21] A. Liu, R. Jones, L. Liao, D. Samara-Rubio, D. Rubin, O. Cohen, R. Nicolaescu, and M. Paniccia, "A high-speed silicon optical modulator based on a metal-oxide-semiconductor capacitor," Nature (London) 427, 615 (2004).
- [22] T. Shoji, T. Tsuchizawa, T. Watanabe, K. Yamada, and H. Morita, "Low loss mode size converter from 0.3  $\mu\text{m}^2$  Si wire waveguides to singlemode fibres," Electron. Lett. 38, 1669, (2002).

## Chapter 6: *Potential applications*

### 6.1 INTRODUCTION

The application of silicon based photonics technology measuring the interaction between photon and specific chemical and biochemical species is increasingly important for a myriad of applications. [1-7] Silicon based photonic sensors have the advantage of a compact structure combined with the potential for monolithic integration with optical-to-electrical detection and advanced electronic circuits. [8] In particular, the slotted waveguide devices recently reported [9] that are able to confine light in a nano-scale low refractive index region are becoming crucial for sensor applications due to the fact that they provide an ideal platform for mode field concentration creating much stronger signature for the analytes under consideration in the active interaction region. However, one of the major challenges for photonic sensors is to improve and calibrate the conventional index-guided waveguide sensitivity. [10] Sensing application using microring resonators [3-5] is a mature solution where the analyte concentration change affects the propagation constants of modes propagating around the microring and thus, the relevant microring resonance wavelength. This resonance wavelength change can be detected with extremely high sensitivity by optimizing the detection scheme. A microring resonator is usually designed with high-quality-factor resonant modes in order to achieve 0.1-nm full-width at half-maximum, [4] which however seriously limits the range of the operation optical bandwidth. Another unique approach is by slowing down the light in defect-engineered photonic crystal waveguides (PCW) to a fraction of its original speed in vacuum and thereby improving the interaction between the optical field and the analyte material by increasing the interaction time through slow light effect. [7, 11, 12] PCW offer slow group velocity and thereby moderately high sensitivity within a continuous

spectrum such that the range of the working wavelength extends to 10 nm scale [13], which can be two orders of magnitude wider than a microring resonator. However, high index region usually dominating the guiding mode in silicon PCW with low-index holes is a major drawback for sensor applications where the interaction with the analytes is weak. [14] It is therefore an attractive design in this paper to merge the benefits of the slotted PCW which provide dual enhancements including better optical field confinement in space and longer interaction in time. In 2007, we reported embedding the slot nanostructure in photonic crystals, and demonstrated a slot PCW configuration with a quasi-transverse-electric mode over 35nm optical bandwidth. [15] Slow light operation in such slot PCW is further investigated experimentally having a slow group index over 100 as an evidence of the specific dispersion control. [14] In this chapter, we present a universal approach based on phase-shift measurement in order to characterize the dual enhancements of the slot PCW suitable for sensor applications. We also implement numerical methods to simulate the effective index variation of the propagating modes and thus justify the approach of device characterization.

## 6.2 SLOTTED STRUCTURE-BASED OPTICAL SENSORS

A schematic of the dual enhanced slot PCW structure for phase-shift measurement is depicted in Fig. 6.2.1. We integrate the slot PCW in a Mach-Zehnder interferometer in order to measure the phase shift  $\Delta\phi$  of the active arm from the output intensity, which is given by  $I_{out} = [I_{in} + I_{in} \cos(\Delta\phi)]/2$ . We can further derive the effective index change  $\Delta n_{eff}$  of the waveguide mode using a linear equation  $\Delta\phi = (2\pi/\lambda)\Delta n_{eff}L$ , where  $L$  is the active length of the phase shifter, and  $\lambda$  is the light wavelength in the free space. The definition of the waveguide sensitivity is given by  $S = \Delta n_{eff} / \Delta n_c$ , [3] where  $\Delta n_c$  is the refractive index change of the waveguide material.

For convenience, we always characterize the sensitivity enhancement in our approach by comparing  $\Delta n_{eff}$  with the same  $\Delta n_c$  profile applied for different waveguide structures.

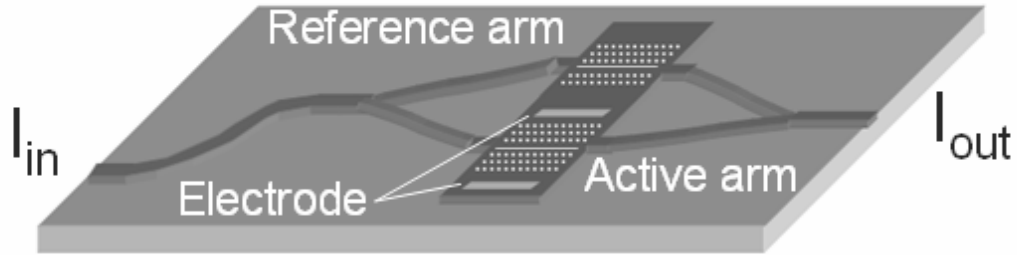


Fig. 6.2.1: Schematic diagram of a Mach-Zehnder interferometer with slot PCWs working as the active and reference arms.

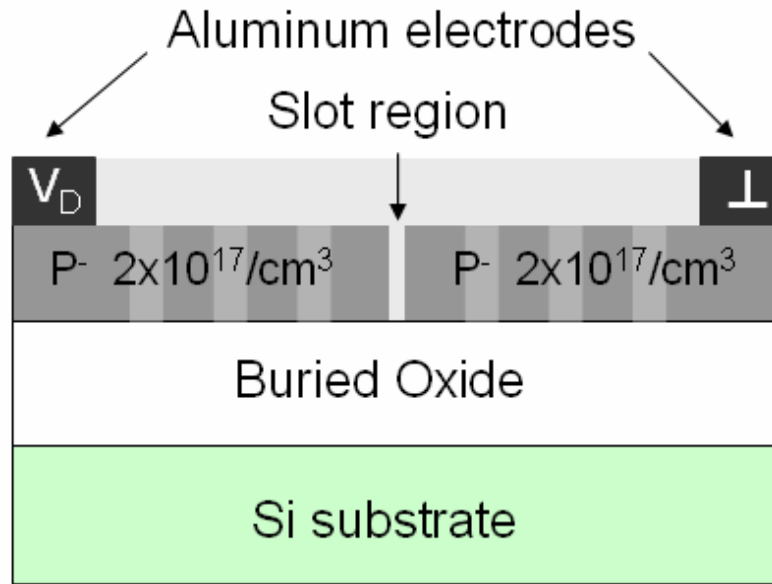


Fig. 6.2.2: Schematic diagram of cross-sectional view of the active arm.



A cross-section diagram of the active arm is depicted in Fig. 6.2.2. For sensor applications, we can fill either gas- or liquid-phase analyte materials into the center slot region and monitor the refractive index change of the analyte material through the output intensity variation of the Mach-Zehnder interferometer. The application of the slot PCW can also be expanded to other sensing configurations. These include Raman sensors, [16] infrared absorption sensors, [7] and fluorescence sensors. [17] In principle, most optical sensors can be applied using the approach presented herein due to the combination of slow light effect and the enhancement of light interaction due to the better confinement of optical guided wave in the slotted PCW. The refractive index change is generated through free carrier dispersion effect, [18, 19] and therefore is controlled by the carrier concentration profile. We design the silicon slab layer with a uniform doping profile in order to simplify the device fabrication procedure. The center trench can be refilled with any low-index analyte material and works as the capacitor dielectric layer. As shown in Fig. 6.2.3, we may control the driving voltage  $V_D$  in order to switch the left silicon region of the lateral capacitor between flat band and accumulation state. When a positive driving voltage is applied to the device, a thin charge layer is accumulated to the left side of the slot while the other side is depleted. The average charge density change  $\Delta N$  on the left side is related with the driving voltage by  $V_D = V_{FB} + q\Delta N t_{ox} t_{eff} / \epsilon_{ox} + q(\Delta N t_{eff})^2 / (2\epsilon_s N_A)$ , [20] where the flat-band voltage  $V_{FB} = 0$  V for a symmetric doping profile,  $t_{ox}$  is the slot width,  $t_{eff}$  is the effective charge layer width,  $\epsilon_{ox}$  and  $\epsilon_s$  are the permittivity of the oxide and silicon regions respectively, and  $N_A$  is the p-type doping concentration of the silicon layer. We can calculate the refractive index change of the accumulation region through an empirical equation  $\Delta n_c = -8.5 \times 10^{-18} (\Delta N)^{0.8}$ . [21]

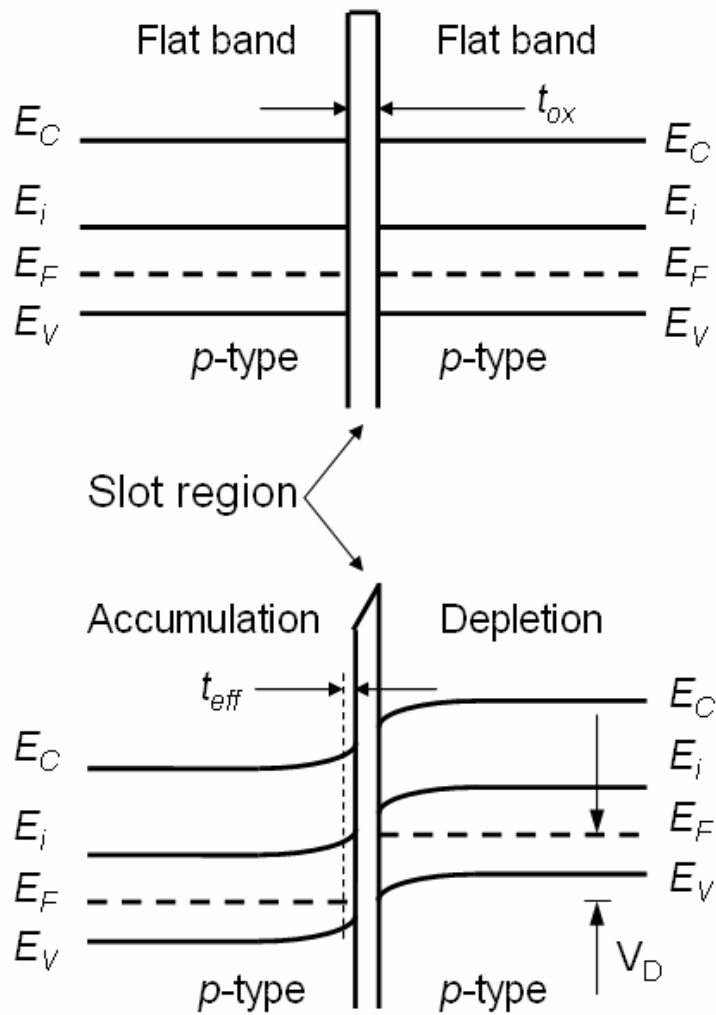


Fig. 6.2.3: Energy band diagram of the capacitor-embedded silicon slab layer. The driving voltage  $V_D$  switches the left region from flat band to accumulation state.

### 6.3 FABRICATION OF SLOT PHOTONIC CRYSTAL WAVEGUIDE-BASED OPTICAL SENSORS

The capacitor-embedded PCW Mach-Zehnder interferometer is fabricated on a silicon-on-insulator wafer with p-type background doping at  $2 \times 10^{17} / \text{cm}^3$ . We grow a 40 nm thermal oxide layer at 950 °C as a hard mask. Then we pattern the oxide mask layer using the E-Beam lithography technique followed by a standard dry etch pattern transfer. The hexagonal lattice pattern of the slot PCW, which provides the largest band gap among all PCW design for quasi-2D PCW, is well optimized to provide slow light effect around  $\lambda = 1.55 \text{ } \mu\text{m}$ . We also employ another thermal oxidation in order to smoothen the surface roughness from the reactive ion etch. Experimental result shows that one can reduce the PCW waveguide propagation loss by 2~3 dB through this procedure. Then the contact windows are opened alongside the slot PCWs by a follow up lift-off process, and the aluminum electrodes are formed afterwards. As the last step, the air holes and the center trench are refilled with spin on glass (SOG) followed by 425 °C decarbonization for 1 hour. Figure 6.3.1 shows a top view of the resulting device with an air slot. We compose a slotted tapering structure in order to achieve better insulation between both sides of the center oxide trench. A similar tapering structure has been proposed to realize efficient mode coupling between a conventional strip waveguide and a slot waveguide. [22] The propagating mode in the strip waveguide is delocalized by the tapering structure and funneled into the slot PCW through the tilted strip structure. A reverse coupling mechanism is applied at the end of the slot PCW. As shown in Fig. 6.3.2, we perform a local milling analysis by the focused-ion-beam technique after filling SOG into the air holes and the center narrow trench, and confirm that the holes and the trench have been fully filled with no void formation.

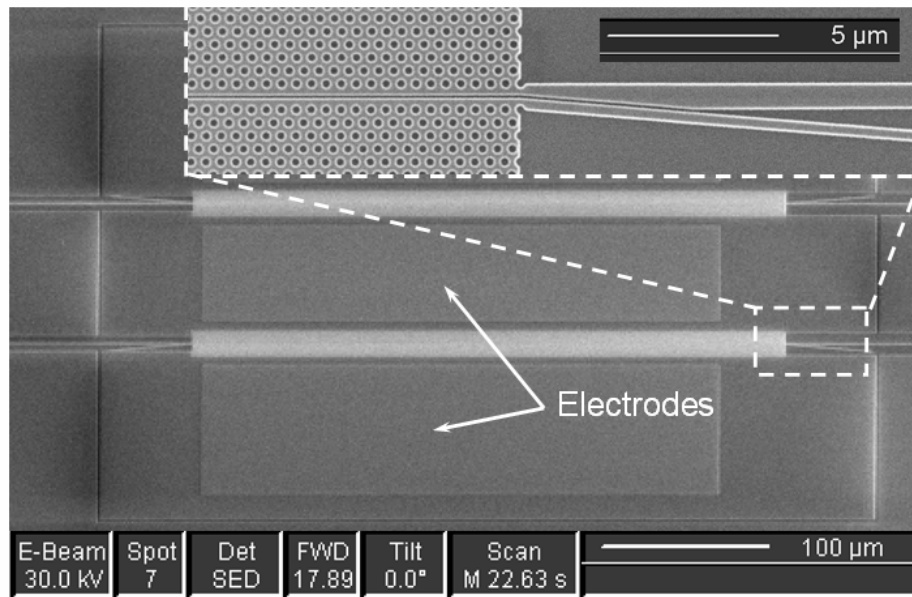


Fig. 6.3.1: Scanning electron microscopy top view of the active region integrated with tapering mode couplers. The tapering structure is enlarged in the inset.

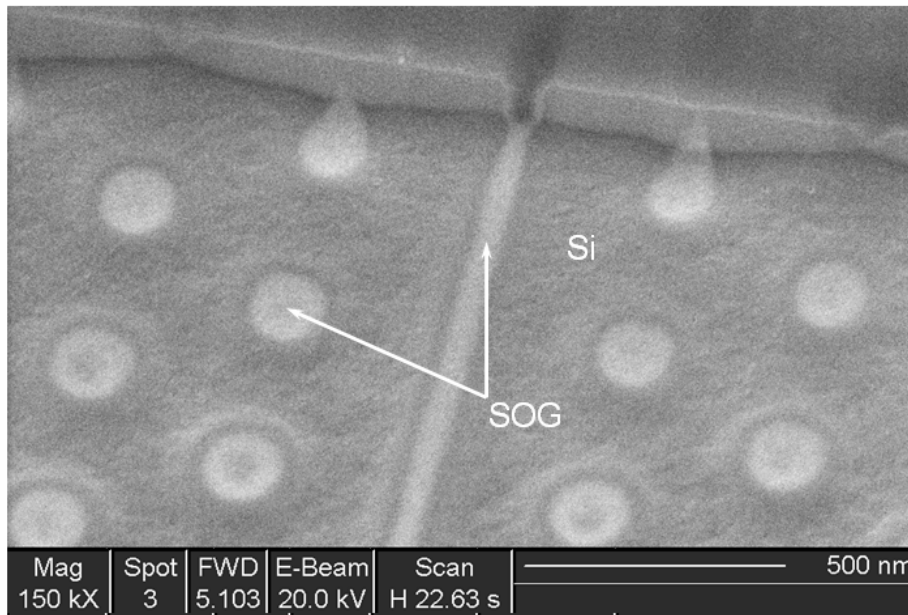


Fig. 6.3.2: Top view of the SOG-filled slot PCW after focused-ion-beam milling.

#### 6.4 SIMULATION AND CHARACTERIZATION OF WAVEGUIDE SENSITIVITY OF SLOT PHOTONIC CRYSTAL WAVEGUIDE

We simulate the band diagram of the slot PCW using plane wave expansion algorithm and calculate the variation of the propagation constant as a function of the driving voltage. The optical property of the slot PCW based Mach-Zehnder interferometer is characterized using a Newport photonics alignment station. Transverse electric (TE) polarized light at a wavelength of 1553 nm is used for optical measurements. We use polarization maintaining fibers with lensed taper ends to couple the light into and out of the interferometer device.

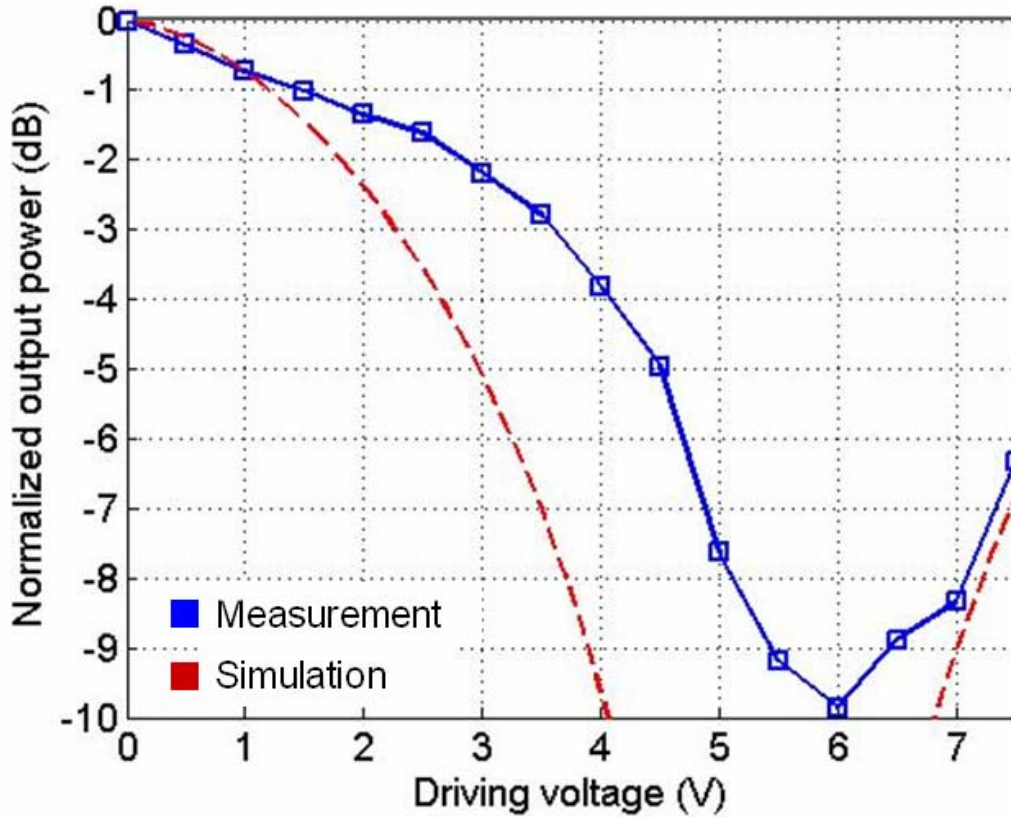


Fig. 6.4.1: The optical intensity at the output of the slot PCW-embedded interferometer as a function of the static driving voltage.

Figure 6.4.1 shows both measured and simulated optical intensity as a function of the static driving voltage. The corresponding band diagram with the operating point is shown in Fig. 6.4.2. The measurement data show reasonable agreement with the simulation result. The intensity difference at high driving voltage is due to the fact that the mode interference is not perfect at the output junction of the interferometer. The contact resistance also induces a positive  $V_\pi$  shift, which can be minimized through additional heavy doping processes. In order to characterize the sensitivity enhancement of slot PCW for sensor applications, we perform similar simulation on a slotted strip waveguide and derive the effective index change of the waveguide mode from the optical intensity curve.

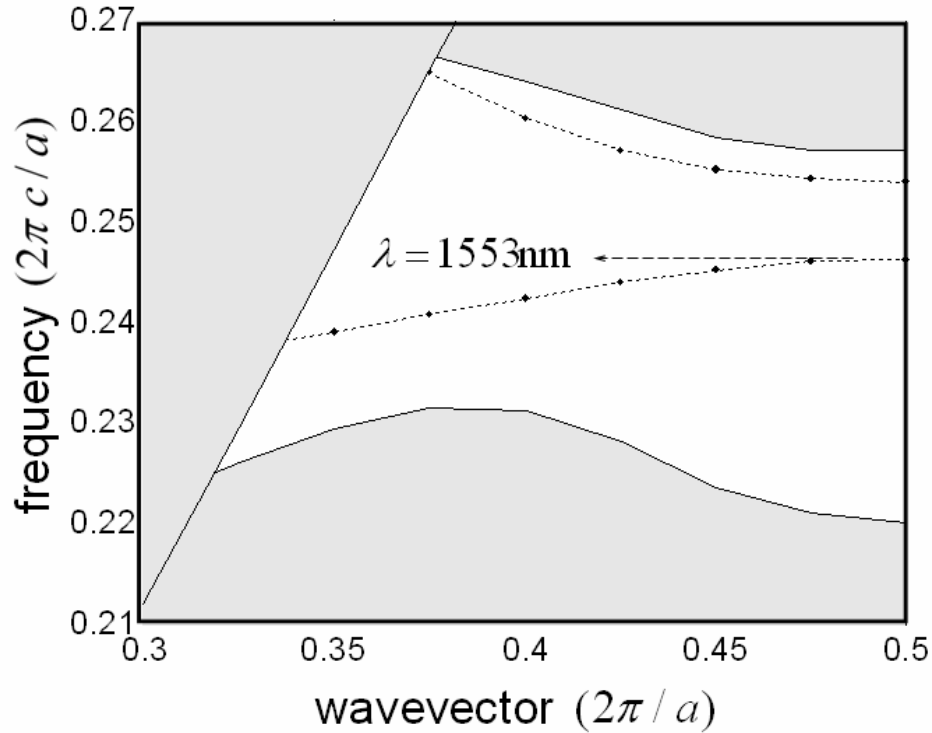


Fig. 6.4.2: The band diagram for a slot photonic crystal waveguide. The solid line is the light line. The gray regions represent the continuum of extended modes. The dotted curves indicate the defect modes.

As indicated in Fig. 6.4.3, the slot PCW always provides 30 times effective index change compared with silicon slot waveguide. Finite-difference time-domain simulation shows that the slot PCW confines 48% mode energy within the center narrow slot of 80 nm in width, which indicates double enhancement in energy confinement compared to conventional silicon strip waveguide [23]. In contrast with slotted strip waveguide, slot PCW slows down the propagation mode and therefore provides significant enhancement of light interaction with a moderate reduction of the optical bandwidth.

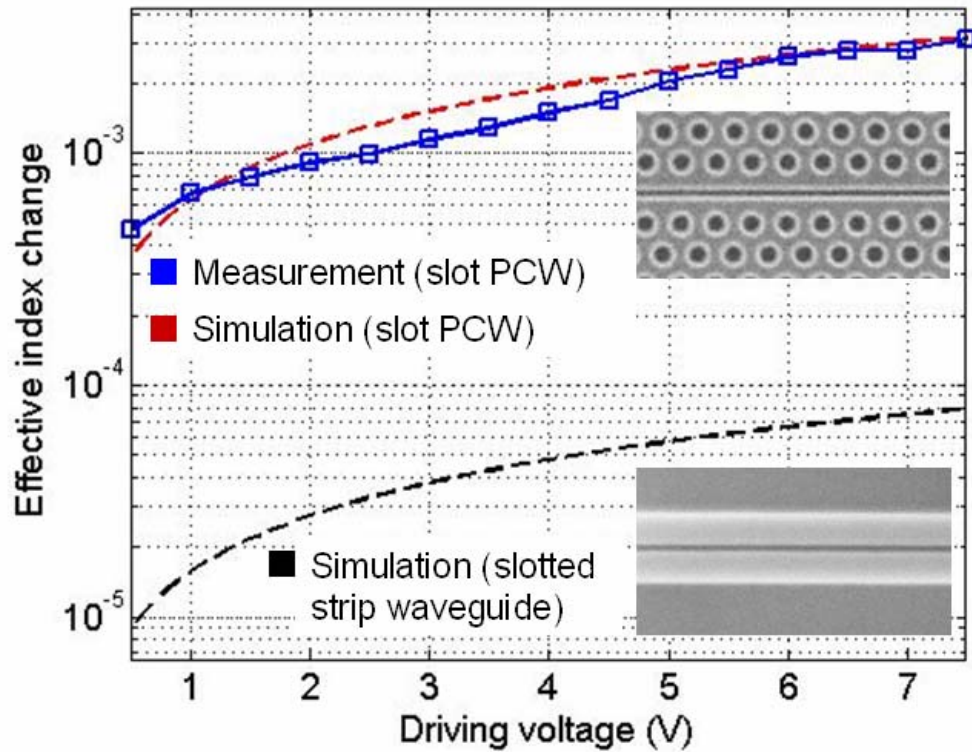


Fig. 6.4.3: Comparison of effective index change between silicon slot PCW and slotted strip waveguide. The measurement data is derived from the optical intensity curve. The insets show the top-view images of slot PCW and slotted strip waveguide respectively.

## 6.5 SUMMARY

In this chapter, we present a slot PCW-based interferometer configuration suitable for optical sensor applications with a universal approach to characterize the sensitivity enhancement compared with silicon slot waveguide. We generate a localized refractive index change through carrier accumulation at the slot boundary. A lateral capacitor model is introduced to simulate the average charge density change as a function of the driving voltage. Both simulation and measurement data demonstrate that the slot PCW-based optical sensor exhibits 30-time sensitivity enhancement than the silicon slot waveguide that benefits from the slow light effect at the band edge. Further comparison of the defect modes between the slotted PCW and the conventional strip waveguide indicates a double enhancement in energy confinement of the narrow defect region.



*Reference:*

- [1] R. G. Heideman, R. P. H. Kooyman, and J. Greve, "Performance of a highly sensitive optical waveguide Mach-Zehnder interferometer immunosensor," *Sens. Actuators B* 10, 209 (1993).
- [2] B. J. Luff, R. D. Harris, and J. S. Wilkinson, "Integrated-optical directional coupler biosensor," *Opt. Lett.* 21, 618 (1996).
- [3] H. Sohlström and M. Öberg, "Refractive index measurement using integrated ring resonators," in *Proceedings of the 8th European Conference on Integrated Optics (EICO'97)* (Royal Institute of Technology, 1997), p. 322.
- [4] A. Yalçın, K. C. Popat, J. C. Aldridge, T. A. Desai, J. Hryniewicz, N. Chbouki, B. E. Little, O. King, V. Van, S. Chu, D. Gill, M. Anthes-Washburn, M. S. Ünlü, and B. B. Goldberg, "Optical sensing of biomolecules using microring resonators," *IEEE J. Sel. Top. Quantum Electron.* 12, 148 (2006).
- [5] K. De Vos, I. Bartolozzi, E. Schacht, P. Bienstman, and R. Baets, "Silicon-on-insulator microring resonator for sensitive and label-free biosensing," *Opt. Express* 15, 7610 (2007).
- [6] A. Schweinsberg, S. Hocdé, N. N. Lepeshkin, R. W. Boyd, C. Chase, and J. E. Fajardo, "An environmental sensor based on an integrated optical whispering gallery mode disk resonator," *Sens. Actuators B* 123, 727 (2007).
- [7] N. A. Mortensen and S. Xiao, "Slow-light enhancement of Beer-Lambert-Bouguer absorption," *Appl. Phys. Lett.* 90, 141108 (2007).
- [8] B. Jalali and S. Fathpour, "Silicon photonics," *J. Lightwave Technol.* 24, 4600 (2006).
- [9] C. A. Barrios, K. B. Gylfason, B. Sanchez, A. Griol, H. Sohlström, M. Holgado, and R. Casquel, "Slot-waveguide biochemical sensor," *Opt. Lett.* 32, 3080 (2007).
- [10] O. Parriaux and G. J. Veldhuis, "Normalized analysis for the sensitivity optimization of integrated optical evanescent-wave sensors," *J. Lightwave Technol.* 16, 573 (1998).
- [11] Y. Jiang, W. Jiang, L. Gu, X. Chen, and R. T. Chen, "80-micron interaction length silicon photonic crystal waveguide modulator," *Appl. Phys. Lett.* 87, 221105 (2005).
- [12] L. Gu, W. Jiang, X. Chen, L. Wang, and R. T. Chen, "High-speed silicon photonic crystal waveguide modulator for low-voltage operation," *Appl. Phys. Lett.* 90, 071105 (2007).

- [13] Y. A. Vlasov, M. O'Boyle, H. F. Hamann, and S. J. McNab, "Active control of slow light on a chip with photonic crystal waveguides," *Nature (London)* 438, 65 (2005).
- [14] A. Di Falco, L. O'Faolain, and T. F. Krauss, "Dispersion control and slow light in slotted photonic crystal waveguides," *Appl. Phys. Lett.* 92, 083501 (2008)
- [15] X. Chen, W. Jiang, L. Gu, and R. T. Chen, "20dB-enhanced coupling to slot photonic crystal waveguide using multimode interference coupler," *Appl. Phys. Lett.* 91, 091111 (2007).
- [16] P. Measor, L. Seballos, D. Yin, J. Z. Zhang, E. J. Lunt, A. R. Hawkins, and H. Schmidt, "On-chip surface-enhanced raman scattering (SERS) detection using integrated liquid-core waveguides," *Appl. Phys. Lett.* 90, 211107 (2007).
- [17] R. Bernini, N. Cennamo, A. Minardo, and L. Zeni, "Planar Waveguides for Fluorescence-Based Biosensing: Optimization and Analysis," *IEEE Sens. J.* 6, 1218 (2006).
- [18] R. A. Soref, and P. J. Lorenzo, "All-silicon active and passive guided-wave components for  $\lambda=1.3$  and  $1.6\ \mu\text{m}$ ," *IEEE J. Quant. Electron.* 22, 873 (1986).
- [19] R. A. Soref, and B. R. Bennett, "Electrooptical effects in silicon," *IEEE J. Quant. Electron.* 23, 123 (1987).
- [20] B. G. Streetman and S. Banerjee, *Solid State Electronic Devices* (Prentice-Hall, Upper Saddle River, NJ, 2000), p. 295.
- [21] R. A. Soref, and B. R. Bennett, "Kramers-Kronig analysis of E-O switching in silicon," *Proc. SPIE* 704, 32 (1986).
- [22] J. Blasco and C.A. Barrios, "Compact slot-waveguide/channel-waveguide mode-converter," *Proceedings of the CLEO Europe'05*, p. 607.
- [23] A. Densmore, D.-X. Xu, P. Waldron, S. Janz, P. Cheben, J. Lapointe, A. Del  ge, B. Lamontagne, J. H. Schmid, and E. Post, "A silicon-on-insulator photonic wire based evanescent field sensor," *IEEE Photonics Technol. Lett.* 18, 2520 (2006).

## Chapter 7: *Summary*

This doctoral research focused on the investigation of periodic-structure-based optical devices, extending from volume-grating-based true-time-delay devices to photonic-crystal based silicon Mach-Zehnder interferometer (MZI) modulators.

A rigorous theory for solving general three-dimensional photonic crystal refraction problems is developed. The power flow direction and transmission intensity of each mode refracted at a periodic surface are rigorously analyzed and determined from matrix equations. We further illustrate how to apply our method to design a low-index-contrast 3D superprism structure that exhibits efficient transmission over a wide angular scanning range at wavelengths near 1550nm.

A miniaturized, delay-enhanced, continuous true-time delay module based on the holographic dispersion has been designed, fabricated and demonstrated to provide squint-free beam steering for K-, Ku- and X-band (8-26.5 GHz) phased-array antenna systems. A novel symmetric structure is employed in the system to achieve large delays and high packaging density. The delay modules operating in the 1550-nm region provide 130 ps of continuously tunable time delay. Far-field radiation patterns measured at 18GHz and 22GHz have experimentally verified the K-band beam-scanning coverage from  $-45^\circ$  to  $+45^\circ$ .

A novel slot photonic crystal structure is experimentally demonstrated for guiding light in a sub-100-nm-wide low-index region. A multimode interference-based coupling structure is introduced to couple light into such a narrow slot photonic crystal waveguide. A coupler of  $1.26\mu\text{m}$  long enhances the coupling efficiency by 20dB for the quasi-TE (transverse electric) mode over 35nm optical bandwidth centered at 1562nm. The measured transmission spectra are in good agreement with the simulated band diagram.

A high speed compact silicon modulator based on the lateral capacitor configuration is experimentally demonstrated with low power consumption of 0.54 pJ/bit and 3 dB modulation depth. The capacitor layout is introduced to scale down the total modulator capacitance to  $30 \times 10^{-15}$  F, which effectively enhances the theoretical intrinsic bandwidth to 40 GHz. Exploiting the slow group velocity of light in the slot photonic crystal waveguides, the device reported herein exhibits higher modulation efficiency than conventional capacitor modulator and provides a  $V_{\pi}L$  figure of merit of 0.18 Vcm at the wavelength of 1548 nm.

A compact silicon photonic sensor based on slot photonic crystal waveguide is experimentally demonstrated. The waveguide sensitivity is characterized in a Mach-Zehnder interferometer configuration. A universal approach is introduced to derive the sensitivity enhancement through local refractive index variation at the slot boundary. Exploiting the slow group velocity of light in photonic crystal waveguides, we demonstrate that the sensitivity is enhanced by 15 dB compared to slotted strip waveguides.

## Bibliography

1. A. A. Barrios, V. R. Almeida, M. Lipson, Low-power-consumption short-length and high-modulation-depth silicon electrooptic modulator. *J Lightwave Technol* 2003,21,1089-1098.
2. A. Agarwal and J. H. Lang, *Foundations of Analog and Digital Electronic Circuits*, 1st ed. (Morgan Kaufmann, 2005), p. 596.
3. A. Cutolo, M. Iodice, A. Irace, P. Spirito, L. Zeni,. An electrically controlled Bragg reflector integrated in a rib silicon on insulator waveguide. *Appl Phys Lett* 1997, 71,199-201.
4. A. Densmore, D.-X. Xu, P. Waldron, S. Janz, P. Cheben, J. Lapointe, A. Del  ge, B. Lamontagne, J. H. Schmid, and E. Post, "A silicon-on-insulator photonic wire based evanescent field sensor," *IEEE Photonics Technol. Lett.* 18, 2520 (2006).
5. A. Di Falco, L. O'Faolain, and T. F. Krauss, "Dispersion control and slow light in slotted photonic crystal waveguides," *Appl. Phys. Lett.* 92, 083501 (2008)
6. A. Irace, G. Breglio, A. Cutolo, All-silicon optoelectronic modulator with 1 GHz switching capability. *Electron Lett*, 2003,39,232.
7. A. Liu, L. Liao, D. Rubin, H. Nguyen, B. Ciftcioglul, Y. Chetrit, N. Izhaky, M. Paniccia. High-speed optical modulation based on carrier depletion in a silicon waveguide. *Opt Express*, 2007, Vol. 15, Issue 2, pp. 660-668.
8. A. Liu, R. Jones, L. Liao, D. Samara-Rubio, D. Rubin, O. Cohen, R. Nicolaescu, and M. Paniccia, "A high-speed silicon optical modulator based on a metal-oxide-semiconductor capacitor," *Nature (London)* 427, 615 (2004).
9. A. Liu, R. Jones, L. Liao, D. Samara-Rubio, D. Rubin, O. Cohen, R. Nicolaescu, M. Paniccia, A high-speed silicon optical modulator based on a metal-oxide-semiconductor capacitor. *Nature* 2004,427,615-618.
10. A. M. Weber, W. K. Smothers, T. J. Trout, and D. J. Mickish, "Hologram recording in Du Pont's new photopolymer materials," *Practical Holography IV*, SPIE OE, Laser Conference Proceedings, 1212-04 (1990).
11. A. Schweinsberg, S. Hocd  , N. N. Lepeshkin, R. W. Boyd, C. Chase, and J. E. Fajardo, "An environmental sensor based on an integrated optical whispering gallery mode disk resonator," *Sens. Actuators B* 123, 727 (2007).

12. A. Sciuto, S. Libertino, S. Coffa, G. Coppola, Miniaturizable Si-based electro-optical modulator working at 1.5  $\mu\text{m}$ . *Appl Phys Lett* 2005,86,201115.
13. A. Yalçın, K. C. Papat, J. C. Aldridge, T. A Desai, J. Hryniewicz, N. Chbouki, B. E. Little, O. King, V. Van, S. Chu, D. Gill, M. Anthes-Washburn, M. S. Ünlü, and B. B. Goldberg, "Optical sensing of biomolecules using microring resonators," *IEEE J. Sel. Top. Quantum Electron.* 12, 148 (2006).
14. B. G. Streetman and S. Banerjee, *Solid State Electronic Devices* (Prentice-Hall, Upper Saddle River, NJ, 2000), p. 291.
15. B. J. Luff, R. D. Harris, and J. S. Wilkinson, "Integrated-optical directional coupler biosensor," *Opt. Lett.* 21, 618 (1996).
16. B. Jalali and S. Fathpour, "Silicon photonics," *J. Lightwave Technol.* 24, 4600 (2006).
17. B. R. Hemenway, O. Solgaard, D. M. Bloom, All-silicon integrated optical modulator for 1.3  $\mu\text{m}$  fiber-optic interconnects. *Appl Phys Lett* 1989,55,349-350.
18. C. A. Barrios, K. B. Gylfason, B. Sanchez, A. Griol, H. Sohlström, M. Holgado, and R. Casquel, "Slot-waveguide biochemical sensor," *Opt. Lett.* 32, 3080 (2007).
19. C. A. Barrios, V. R. Almeida, R. R. Panepucci and M. Lipson, Electro-optic modulation of silicon-on-insulator submicron-size waveguide devices *IEEE J Lightwave Technol* 2003,21,2332.
20. C. K. Tang, G. T. Reed, Highly efficient optical phase modulator in SOI waveguides. *Electron Lett* 1995,31,451–452.
21. C. T. Chan, K. M. Ho and C. M. Soukoulis, "Photonic band gaps in experimentally realizable periodic dielectric structures", *Europhys. Lett.* 16, 563 (1991).
22. C. Z. Zhao, G. Z. Li, E. K. Liu, Y. Gao, X. D. Liu, Silicon on insulator Mach-Zehnder waveguide interferometers operating at 1.3  $\mu\text{m}$ . *Appl Phys Lett* 1995,67,2448-2450.
23. D. Dolfi, J.P. Huignard, and M. Baril, "Optically controlled true time delays for phased array antenna," *Proc. SPIE*, vol. 1102, pp. 152-161, 1989.
24. E. A. Camargo, and H. M. H. Chong, "2D photonic crystal thermo-optic switch based on AlGaAs/GaAs epitaxial structure", *Opt Express*, 12, 588, (2004).
25. E. Chow, S. Y. Lin, S. G. Johnson, P. R. Villeneuve, J. D. Joannopoulos, J.-R. Wendt, G. A. Vawter, W. Zubrzycki, H. Hou, and A. Alleman, "Three-

- dimensional control of light in a two-dimensional photonic crystal slab,” *Nature* (London) 407, 983 (2000).
26. E. Yablonovitch, T. J. Gmitter, and K. M. Lung, “Photonic band structure: The face-centered-cubic case employing nonspherical atoms”, *Phys. Rev. Lett.* 67, 2295 (1991).
  27. E. Yablonovitch, “Inhibited Spontaneous Emission in Solid-State Physics and Electronics”, *Phys. Rev. Lett.*, 58, 2059 (1987).
  28. F. Gan, F. X. Kartner, High-speed silicon electrooptic modulator design. *IEEE Photon Technol Lett* 2005,17,1007-1009.
  29. G. Cocorullo, F. G. Della Corte, and I. Rendina, “Temperature dependence of the thermo-optic coefficient in crystalline silicon between room temperature and 550 K at the wavelength of 1523 nm,” *Appl. Phys. Lett.* 74, 3338 (1999).
  30. G. T. Reed, A. P. Knights, *Silicon photonics, an introduction*. Chichester, John Wiley, 2004.
  31. G. V. Treyz, P. G. May, J. Halbout, Silicon Mach-Zehnder waveguide interferometers based on the plasma dispersion effect. *Appl Phys Lett* 1991, 59,771-3.
  32. H. Benisty, J. M. Lourtioz, A. Chelnokov, S. Combrie, X. Checoury, “Recent advances toward optical devices in semiconductor-based photonic crystals”, *Proceedings of the IEEE*, 94, 5, 997 (2006).
  33. H. G. Park, S. H. Kim, S. H. Kwon, Y. G. Ju, J. K. Yang, J. H. Baek, et al. “Electrically driven single-cell photonic crystal laser”, *Science*, 305, 1444–7, (2004).
  34. H. Gersen, T. J. Karle, R. J. P. Engelen, W. Bogaerts, J. P. Korterik, N. F. Van, et al. “Real-space observation of ultraslow light in photonic crystal waveguides”, *Phys Rev Lett*, 94, 073903, (2005).
  35. H. Kogelnik, “Coupled wave theory for thick hologram gratings,” *Bell Syst. Tech. J.*, vol. 48, pp. 2909-2947, 1969.
  36. H. Kosaka, T. Kawashima, A. Tomita, M. Notomi, T. Tamamura, T. Sato, and S. Kawakami, “Superprism phenomena in photonic crystals,” *Phys. Rev. B, Condens. Matter*, vol. 58, no. 16, pp. R10096–R10099, Oct. 1998.
  37. H. Kosaka, T. Kawashima, A. Tomita, M. Notomi, T. Tamamura, T. Sato, and S. Kawakami, “Superprism phenomena in photonic crystals: toward microscale lightwave circuits”, *IEEE J. Lightwave Tech.*, 17, 11, 2032 (1999).

38. H. Kosaka, T. Kawashima, A. Tomita, M. Notomi, T. Tamamura, T. Sato, and S. Kawakami, "Superprism phenomena in photonic crystals:", *Phys. Rev. B* 58, 16, R10096 (1998).
39. H. Kosaka, T. Kawashima, A. Tomita, M. Notomi, T. Tamamura, T. Sato, and S. Kawakami, "Self-collimating phenomena in photonic crystals", *Appl. Physics. Lett.*, 74, 9, 1212 (1999).
40. H. S. Sozuer and J. W. Haus, "Photonic bands – simple-cubic lattice," *J. Opt. Soc. Am. B*, vol. 10, no. 2, pp. 296-302, Feb. 1993.
41. H. Sohlström and M. Öberg, "Refractive index measurement using integrated ring resonators," in *Proceedings of the 8th European Conference on Integrated Optics (EICO'97)* (Royal Institute of Technology, 1997), p. 322.
42. J. Blasco and C.A. Barrios, "Compact slot-waveguide/channel-waveguide mode-converter," *Proceedings of the CLEO Europe'05*, p. 607.
43. J. Chen, W. Jiang, X. Chen, L. Wang, S. Zhang, and R. T. Chen, "Holographic three-dimensional polymeric photonic crystals operating in the 1550 nm window," *Appl. Phys. Lett.*, vol. 90, p. 093 102, Feb. 2007.
44. J. D. Joannopoulos, R.D. Meade, J.N. Winn, *Photonic Crystals*, Princeton University Press, (1995) .
45. J. P. Lorenzo, R. A. Soref, 1.3 mm electro-optic silicon switch. *Appl Phys Lett* 1987, 51, 6-8.
46. J. Shin and S. Fan, "Conditions for self-collimation in three-dimensional photonic crystals," *Opt. Lett.*, vol. 30, no. 18, pp. 2397-2399 Sep. 2005.
47. K. De Vos, I. Bartolozzi, E. Schacht, P. Bienstman, and R. Baets, "Silicon-on-insulator microring resonator for sensitive and label-free biosensing," *Opt. Express* 15, 7610 (2007).
48. K. Inoue and K. Ohtaka, *Photonic Crystals: Physics, Fabrication and Applications*, Springer-Verlag, New York, 2004
49. K. M. Ho, C. T. Chan, and C. M. Soukoulis, "Existence of a photonic gap in periodic dielectric structures", *Phys. Rev. Lett.* 65, 3152 (1990).
50. K. M. Ho, C. T. Chan, C. M. Soukoulis, R. Biswas, and M. Sigalas, "Photonic band gaps in three dimensions: New layer-by-layer periodic structures", *Solid State Communications*, 89, 5, 413 (1994).



51. L. B. Soldano and E. C. Pennings, "Optical multimode interference devices based on self-imaging-principles and applications," *J. Lightwave Technol.* 13, 615 (1995).
52. L. Gu, W. Jiang, X. Chen, and R. T. Chen, "Thermooptically Tuned Photonic Crystal Waveguide Silicon-on-Insulator Mach-Zehnder Interferometers," *IEEE Photonics Technol. Lett.* 19, 342 (2007).
53. L. Gu, W. Jiang, X. Chen, L. Wang, and R. T. Chen, "High speed silicon photonic crystal waveguide modulator for low voltage operation," *Appl. Phys. Lett.*, vol. 90, no. 7, p. 071 105, Feb. 2007.
54. L. Gu, W. Jiang, X. Chen, L. Wang, and R. T. Chen, "High-speed silicon photonic crystal waveguide modulator for low-voltage operation," *Appl. Phys. Lett.* 90, 071105 (2007).
55. L. Gu, W. Jiang, X. Chen, R. T. Chen, "Photonic crystal waveguide based silicon-on-insulator thermo-optic Mach Zehnder interferometers", *IEEE Photon Technol Lett*, 19, 342, (2007).
56. L. Gu, X. Chen, W. Jiang, and R. T. Chen, "A solution to the fringing-field effect in liquid crystal based high-resolution switchable gratings," *Appl. Phys. Lett.* 87, 201106 (2005).
57. L. Gu, X. Chen, Z. Shi, B. Howley, J. Liu, and R. T. Chen, "Bandwidth-enhanced volume grating for dense wavelength-division multiplexer using a phasecompensation scheme," *Appl. Phys. Lett.* 86, 181103 (2005).
58. L. Gu, Y. Jiang, W. Jiang, X. Chen, R. T. Chen, "Silicon-on-insulatorbased photonic-crystal Mach-Zehnder interferometers", *Proc SPIE*, 6128, 261–8, (2006).
59. L. Li, "Formulation and comparison of two recursive matrix algorithms for modeling layered diffraction gratings," *J. Opt. Soc. Am. A* 13, 1024–1035 (1996).
60. L. Li, "Multilayer modal method for diffraction gratings of arbitrary profile, depth, and permittivity," *J. Opt. Soc. Am. A* 10, 2581–2591 (1993).
61. L. Liao, D. Samara-Rubio, M. Morse, A. Liu, D. Hodge, D. Rubin, U. D. Keil, and T. Franck, "High speed silicon Mach-Zehnder modulator," *Opt. Express* 13, 3129 (2005).
62. L. Pavesi, D. J. Lockwood, editors. *Silicon photonics*. Berlin, Springer, 2004.
63. L. Pavesi, S. Gaponenko, editors. *Towards the first silicon laser (NATO Science Series)*. Dordrecht, Kluwer, 2003.

64. M. Charlton, J. Lincoln, G. Flinn, "Planar photonic crystals move toward wider use", *Laser Focus World* June, 2005.
65. M. G. Moharam and T. K. Gaylord, "Diffraction analysis of dielectric surface-relief gratings," *J. Opt. Soc. Am.* 72, 1385–1392 (1982).
66. M. G. Moharam, D. A. Pommet, E. B. Grann, and T. K. Gaylord, "Stable implementation of the rigorous coupledwave analysis for surface-relief gratings: enhanced transmittance matrix approach," *J. Opt. Soc. Am. A* 12, 1077–1086 (1995).
67. M. H. Shih, W. J. Kim, W. Kuang, J. R. Cao, H. Yukawa, S. J. Choi, et al. "Two-dimensional photonic crystal Mach-Zehnder interferometers", *Appl Phys Lett*, 84, 460, (2004).
68. M. Notomi, A. Shinya, S. Mitsugi, E. Kuramochi, H. Y. Ryu, "Waveguides, resonators and their coupled elements in photonic crystal slabs", *Opt Express*, 12, 1551–61, (2004).
69. M. Notomi, K. Yamada, A. Shinya, J. Takahashi, C. Takahashi, I. Yokohama, "Extremely large group-velocity dispersion of linedefect waveguides in photonic crystal slabs", *Phys Rev Lett*, 87, 253902, (2001).
70. M. R. Wang, G. J. Sonek, R. T. Chen, and T. Jansson, "Large fanout optical interconnects using thick holographic gratings and substrate wave propagation," *Appl. Opt.* 31, 236–249 (1992).
71. M. Soljacic, S. G. Johnson, S. Fan, M. Ibanescu, E. Ippen, J. D. Joannopoulos, "Photonic-crystal slow-light enhancement of nonlinear phase sensitivity". *J Opt Soc Am B*, 19, 2052–9, (2002).
72. N. A. Mortensen and S. Xiao, "Slow-light enhancement of Beer-Lambert-Bouguer absorption," *Appl. Phys. Lett.* 90, 141108 (2007).
73. N. Chateau and J. P. Hugonin, "Algorithm for the rigorous coupled-wave analysis of grating diffraction," *J. Opt. Soc. Am. A* 11, 1321–1331 (1994).
74. O. Parriaux and G. J. Veldhuis, "Normalized analysis for the sensitivity optimization of integrated optical evanescent-wave sensors," *J. Lightwave Technol.* 16, 573 (1998).
75. P. Dainesi, A. Kung, M. Chabloz, A. Lagos, P. Fluckiger, A. Ionescu, P. Fazan, M. Declerq, P. Renaud, P. Robert, CMOS compatible fully integrated Mach-Zehnder Interferometer in SOI Technology. *IEEE Photon Technol Lett* 2000,12,660-662.

76. P. Measor, L. Seballos, D. Yin, J. Z. Zhang, E. J. Lunt, A. R. Hawkins, and H. Schmidt, "On-chip surface-enhanced raman scattering (SERS) detection using integrated liquid-core waveguides," *Appl. Phys. Lett.* 90, 211107 (2007).
77. Q. Xu, B. Schmidt, S. Pradhan, M. Lipson, Micrometre-scale silicon electro-optic modulator. *Nature* 2005,435,325-327.
78. Q. Xu, S. Manipatruni, B. Schmidt, J. Shakya, and M. Lipson, "12.5 Gbit/s carrier-injection-based silicon micro-ring silicon modulators," *Opt. Express* 15, 430 (2007).
79. R. A. Soref, and B. R. Bennett, "Electrooptical effects in silicon," *IEEE J. Quant. Electron.* 23, 123 (1987).
80. R. A. Soref, and B. R. Bennett, "Kramers-Kronig analysis of E-O switching in silicon," *Proc. SPIE* 704, 32 (1986).
81. R. A. Soref, and P. J. Lorenzo, "All-silicon active and passive guided-wave components for  $\lambda=1.3$  and  $1.6\ \mu\text{m}$ ," *IEEE J. Quant. Electron.* 22, 873 (1986).
82. R. A. Soref, B. R. Bennett, Electrooptical effects in silicon. *IEEE J Quantum Electron* 1987,23,123-129.
83. R. B. Wehrspohn, "Applications of silicon-based photonic crystals", 2nd IEEE International Conference on Group IV Photonics, 39 (2005).
84. R. Bernini, N. Cennamo, A. Minardo, and L. Zeni, "Planar Waveguides for Fluorescence-Based Biosensing: Optimization and Analysis," *IEEE Sens. J.* 6, 1218 (2006).
85. R. G. Heideman, R. P. H. Kooyman, and J. Greve, "Performance of a highly sensitive optical waveguide Mach-Zehnder interferometer immunosensor," *Sens. Actuators B* 10, 209 (1993).
86. R. T. Chen, H. Lu, D. Robinson, and T. Jannson, "Highly multiplexed graded-index polymer waveguide hologram for near-infrared eight-channel wavelength division demultiplexing," *Appl. Phys. Lett.* 59, 1144–1146 (1991).
87. S. G. Johnson and J. D. Joannopoulos, "Block-iterative frequency-domain methods for Maxwell's equations in a planewave basis," *Opt. Express* vol. 8, no. 3, pp. 173-190, Jan. 2001.
88. S. G. Johnson, J. D. Joannopoulos, *Photonic crystals: road from theory to practice*, Kluwer Academic Publishers, (2002).

89. S. G. Jonson, P. R. Villeneuve, S. Fan, and J. D. Joannopoulos, "Linear waveguides in photonic-crystal slabs," *Phys. Rev. B* 62, 8212 (2000).
90. S. H. Choi and K. Roy, "Noise analysis under capacitive and inductive coupling for high speed circuits," *Proceedings of the 1st IEEE International Workshop on Electronic Design, Test and Applications (DELTA'02)*, p. 365.
91. S. John, "Strong localization of photons in certain disordered dielectric superlattices", *Phys. Rev. Lett.* 58, 2486 (1987).
92. S. M. Sze and K. K. Ng, *Physics of Semiconductor Devices*, 3rd ed. (Wiley, New York, 2007), p. 233.
93. S. M. Weiss, H. Ouyang, J. Zhang, P. M. Fauchet, "Electrical and thermal modulation of silicon photonic bandgap microcavities containing liquid crystals", *Opt Express*, 13 (4), 1090, (2005).
94. S. Ogawa, M. Imada, S. Yoshimoto, M. Okano, S. Noda, *Science* 305, 227, (2004).
95. S. Y. Lin, V. M. Hietala, L. Wang, and E. D. Jones, "Highly dispersive photonic band-gap prism", *Opt. Lett.* 21 1771 (1996).
96. T. Chu, H. Yamada, S. Ishida, Y. Arakawa, "Thermooptic switch based on photonic-crystal line-defect waveguides", *IEEE Photon Technol Lett*, 17 (10), 2083–5, (2005).
97. T. Minami, H. Ajiki, K. Cho, "Branching ratio of light incident on a photonic crystal in a multibranch dispersion region," *Physica E-low-dimensional systems & nanostructures*, vol. 13, no. 2-4, pp. 432-436, Mar. 2002.
98. T. Prasad, V. Colvin, and D. Mittleman, "Superprism phenomenon in three-dimensional macroporous polymer photonic crystals," *Phys. Rev. B*, vol. 67, no. 16, p. 165 103, Apr. 2003.
99. T. Shoji, T. Tsuchizawa, T. Watanabe, K. Yamada, and H. Morita, "Low loss mode size converter from 0.3  $\mu\text{m}^2$  Si wire waveguides to singlemode fibres," *Electron. Lett.* 38, 1669, (2002).
100. V. Mizeikis, K. K. Seet, S. Juodkazis, and H. Misawa, "Three-dimensional woodpile photonic crystal templates for the infrared spectral range," *Opt. Lett.*, vol. 29, no. 17, pp. 2061–2063, Sep. 2004.
101. W. Jiang, R. T. Chen, X. Lu, "Theory of light refraction at the surface of a photonic crystal", *Phys Rev B* 71, 245115, (2005).

102. W. J. Gambogi, W. A. Gerstadt, S. R. Mackara and A. M. Weber, "Holographic transmission elements using improved photopolymer films," SPIE Computer and Optically Generated Holographic Optics, 1555, 256-267 (1991).
103. W. Jiang and C. Gong, "Two mechanisms, three stages of the localization of light in a disordered dielectric structure with photonic band gaps," Phys. Rev. B, vol. 60, no. 17, p. 12015, Nov. 1999.
104. W. Jiang, L. Gu, X. Chen, and R. T. Chen, Photonic Crystal Waveguide Modulators for Silicon Photonics: Device Physics and Some Recent Progress, Solid State Electronics, vol. 51, pp. 1278-1286, 2007.
105. W. Jiang, R. T. Chen "Multichannel optical add-drop process in symmetrical waveguide-resonator systems", Phys Rev Lett 91, 213901, (2003).
106. W. Jiang, R. T. Chen and X. Lu, "Theory of light refraction at the surface of a photonic crystal," Phys. Rev. B, vol. 71, no. 24, p. 245 115, Jun. 2005.
107. W. M. J. Green, M. J. Rooks, L. Sekaric, and Y. A. Vlasov, "Optical modulation using anti-crossing between paired amplitude and phase resonators," Opt. Express 15, 17107, (2007).
108. W. Ng, A. A. Walston, G. L. Tangonan, J. J. Lee, I. L. Newberg, and N. Bernstein, "The first demonstration of an optically steered microwave phased array antenna using true time-delay," J. Lightwave Technol., vol. 9, pp. 1124-1131, Sept. 1991.
109. X. Chen, W. Jiang, J. Chen, and R. T. Chen, "Theoretical Study of Light Refraction in Three-Dimensional Photonic Crystals," IEEE/OSA Journal of Lightwave Technology, vol. 25, no. 9, pp. 2469-2474, Sept. 2007.
110. X. Chen, W. Jiang, L. Gu, and R. T. Chen, "20dB-enhanced coupling to slot photonic crystal waveguide using multimode interference coupler," Appl. Phys. Lett. 91, 091111 (2007).
111. X. Chen, Z. Shi, L. Gu, B. Howley, Y. Jiang, and R. T. Chen, Miniaturized delay-time-enhanced photopolymer waveguide hologram module for phased-array antenna, IEEE Photonics Technology Letters, vol. 17, no. 10, 2182-2184 (2005).
112. Y. A. Vlasov, M. O'Boyle, H. F. Hamann, and S. J. McNab, "Active control of slow light on a chip with photonic crystal waveguides," Nature (London) 438, 65 (2005).
113. Y. A. Vlasov, M. O'Boyle, H. F. Hamann, S. J. McNab, "Active control of slow light on a chip with photonic crystal waveguides", Nature, 438, 65–9, (2005).

- 114.Y. A. Vlasov, S. J. McNab, "Coupling into the slow light mode in slab-type photonic crystal waveguides," *Opt. Lett.* 31, 50 (2006).
- 115.Y. A. Vlasov, X.-Z. Bo, J. C. Sturm, and D. J. Norris, "On-chip natural assembly of silicon photonic bandgap crystals," *Nature* vol. 414, no. 6861, pp. 289-293 Nov. 2001.
- 116.Y. H. Kuo, Y. K. Lee, K. Ge, S. Ren, J. E. Roth, T. I. Kamins, D. A. B. Miller, J. S. Harris, Strong quantum-confined Stark effect in germanium quantum-well structures on silicon. *Nature* 2005,437,1334-1336.
- 117.Y. Jiang, W. Jiang, L. Gu, X. Chen, and R. T. Chen, "80-micron interaction length silicon photonic crystal waveguide modulator," *Appl. Phys. Lett.* 87, 221105 (2005).
- 118.Z. Li and K. Ho, "Application of structural symmetries in the plane-wave-based transfer-matrix method for three-dimensional photonic crystal waveguides," *Phys. Rev. B*, vol. 68, no. 24, p. 155 101, Dec. 2003.
- 119.Z. Lu, J. A. Murakowski, C. A. Schuetz, S. Shi, G. J. Schneider, and D. W. Prather, "Three-dimensional subwavelength imaging by a photonic-crystal flat lens using negative refraction at microwave frequencies," *Phys. Rev. Lett.*, vol. 95, no.15, p. 153 901, Oct. 2005.
- 120.Z. Shi, L. Gu, B. Howley, Y. Jiang, Q. Zhou, R. T. Chen, H. R. Fetterman, C. Lee, and G. Brost, "True-time-delay modules based on single tunable laser in conjunction with waveguide-hologram for phased array antenna application," *Optical Engineering*, (in press).
- 121.Z. Y. Li, L. L. Lin and K. M. Ho, "Light coupling with multimode photonic crystal waveguides," *Appl. Phys. Lett.* 84, 4699 (2004).

## VITA

Xiaonan Chen was born in Harbin, Heilongjiang Province, P. R. China, on March 27<sup>th</sup>, 1980, the son of Kun Chen and Lijiang Liu. After completing his study at Harbin No. 3 High School, Harbin, Heilongjiang Province, P.R. China, in 1998, he entered Tsinghua University, Beijing, P.R. China. He received the degree of Bachelor of Science from Department of Precision Instruments and Mechanology in 2002. He attended the University of Texas at Austin, Austin, Texas, in 2003 and obtained the degree of Master of Science in Electrical and Computer Engineering in 2006.

## Publications

- 06/08 **Xiaonan Chen**, Yun-Sheng Chen, Yang Zhao, Wei Jiang, and Ray T. Chen, *0.54 pJ/bit Capacitor-Embedded Silicon Slot Photonic Crystal Waveguide Modulator*, (to be submitted, 2008).
- 06/08 **Xiaonan Chen**, and Ray T. Chen, *Dual Enhancements for Signal Detection using Silicon Slot Photonic Crystal Waveguides*, (to be submitted, 2008).
- 09/07 **Xiaonan Chen**, Wei Jiang, Jiaqi Chen, and Ray T. Chen, *Theoretical Study of Light Refraction in Three-Dimensional Photonic Crystals*, IEEE/OSA Journal of Lightwave Technology, vol. 25, no. 9, pp. 2469-2474, Sept. 2007.
- 08/07 **Xiaonan Chen**, Wei Jiang, Jiaqi Chen, Lanlan Gu, and Ray T. Chen, *20dB-enhanced coupling to slot photonic crystal waveguide using multimode interference coupler*, Applied Physics Letters, vol. 91, no. 091111, Aug. 2007.
- 08/07 **Xiaonan Chen**, Lanlan Gu, and Ray T. Chen, *Efficient transmission control based on carrier accumulation in silicon slot photonic-crystal waveguide as an*

- embedded layer for board level optical interconnects*, Proc. SPIE Annual meeting on Active Nanophotonic Crystals 2007, San Diego, CA (Invited).
- 06/07 **Xiaonan Chen**, Wei Jiang, Jiaqi Chen, Lanlan Gu, and Ray T. Chen, *High bandwidth silicon photonic-crystal modulator based on vertical MOS capacitor*, The OSA Topical Conference On Nanophotonics (NANO) 2007, Hangzhou, China.
- 05/07 **Xiaonan Chen**, Jiaqi Chen, Lanlan Gu, Wei Jiang, and Ray T. Chen, *Silicon photonic crystal modulation device based on horizontally activated MOS capacitor*, 2007 4th IEEE International Conference on Group IV Photonics, Tokyo, Japan.
- 02/07 **Xiaonan Chen**, Lanlan Gu, Wei Jiang, and Ray T. Chen, *Active transmission control based on photonic-crystal MOS capacitor*, Proc. SPIE Photonic West 2007, San Jose, CA.
- 10/05 **Xiaonan Chen**, Zhong Shi, Lanlan Gu, Brie Howley, Yongqiang Jiang, and Ray T. Chen, *Miniaturized delay-time-enhanced photopolymer waveguide hologram module for phased-array antenna*, IEEE Photonics Technology Letters, vol. 17, no. 10, pp. 2182-2184, Oct. 2005.
- 06/04 **Xiaonan Chen**, Zhong Shi, and Ray T. Chen, *Miniaturized delay-enhanced substrate-guided wave based holograms for continuous tuning of delay times*, IEEE LEOS Summer Topicals 2004, San Diego, CA.
- 01/06 Yongqiang Jiang, **Xiaonan Chen**, Brie Howley, Maggie Y. Chen, and Ray T. Chen, *Effects of temperature fluctuation on highly dispersive photonic crystal fibers*, Applied Physics Letters, vol. 88, no. 011108, Jan. 2006.
- 11/05 Lanlan Gu, **Xiaonan Chen**, Wei Jiang, Brie Howley, and Ray T. Chen, *Fringing-field minimization in liquid-crystal-based high-resolution switchable gratings*, Applied Physics Letters, vol. 87, no. 201106, Nov. 2005.
- 05/05 Lanlan Gu, **Xiaonan Chen**, Zhong Shi, Brie Howley, Jian Liu, and Ray T. Chen, *Bandwidth-enhanced volume grating for dense wavelength-division multiplexer using a phase-compensation scheme*, Applied Physics Letters, vol. 86, no. 181103, May 2005.
- 04/05 Lanlan Gu, **Xiaonan Chen**, Yongqiang Jiang, Jian Liu, and Ray T. Chen, *High-spatial-frequency liquid crystal phase gratings with double-sided striped electrodes*, Proc. SPIE Photonic West 2005, San Jose, CA.
- 09/07 Wei Jiang, Lanlan Gu, **Xiaonan Chen**, and Ray T. Chen, *Photonic Crystal Waveguide Modulators for Silicon Photonics: Device Physics and Some Recent Progress*, Solid State Electronics, vol. 51, pp. 1278-1286, Sept. 2007.



- 06/07 Li Wang, Wei Jiang, **Xiaonan Chen**, Lanlan Gu, Jiaqi Chen, and Ray T. Chen, *Fabrication of polymer photonic crystal superprism structures using polydimethylsiloxane soft molds*, Journal of Applied Physics, vol. 101, no. 114316, Jun. 2007.
- 06/07 Jiaqi Chen, Wei Jiang, **Xiaonan Chen**, Li Wang, Sasa Zhang, and Ray T. Chen, *3D Nano-photonic Crystal structures for superprism application*, The OSA Topical Conference On Nanophotonics (NANO) 2007, Hangzhou, China.
- 04/07 Lanlan Gu, Wei Jiang, **Xiaonan Chen**, and Ray T. Chen, *Thermooptically tuned photonic crystal waveguide silicon-on-insulator Mach-Zehnder interferometers*, IEEE Photonics Technology Letters, vol. 19, no. 5-8, pp. 342-344, Apr. 2007.
- 02/07 Lanlan Gu, Wei Jiang, **Xiaonan Chen**, Li Wang, and Ray T. Chen, *High-speed electro-optical silicon modulators based on photonic crystal waveguides*, Proc. SPIE Photonic West 2007, San Jose, CA.
- 02/07 Jiaqi Chen, Wei Jiang, **Xiaonan Chen**, Li Wang, Sasa Zhang, and Ray T. Chen, *Holographic three-dimensional polymeric photonic crystals operating in the 1550 nm window*, Applied Physics Letters, vol. 90, no. 093102, Feb. 2007.
- 02/07 Li Wang, Wei Jiang, **Xiaonan Chen**, Jiaqi Chen, Sasa Zhang, and Ray Chen, *Superprism phenomena in 2D low index contrast polymer photonic crystal*, Proc. SPIE Photonic West 2007, San Jose, CA.
- 02/07 Lanlan Gu, Wei Jiang, **Xiaonan Chen**, Li Wang, and Ray T. Chen, *High speed silicon photonic crystal waveguide modulator for low voltage operation*, Applied Physics Letters, vol. 90, no. 071105, Feb. 2007.
- 02/07 Jiaqi Chen, Wei Jiang, **Xiaonan Chen**, Li Wang, Sasa Zhang, and Ray T. Chen, *3D holographic polymer photonic crystal for superprism application*, Proc. SPIE Photonic West 2007, San Jose, CA.
- 02/07 Jiaqi Chen, Wei Jiang, **Xiaonan Chen**, Li Wang, Sasa Zhang, and Ray T. Chen, *3D Nanophotonic Crystal structures for Laser Beam Switching and Steering*, The 4th U.S. Air Force/Taiwan Nanoscience and Nanotechnology workshop, Feb. 2007.
- 10/06 Hai Bi, Xuliang Han, **Xiaonan Chen**, Wei Jiang, Jinho Choi, and Ray T. Chen, *15Gb/s Bit-Interleaved Optical Backplane Bus using Volume Photo-polymer Holograms*, IEEE Photonics Technology Letters, vol. 18, no. 17-20, pp. 2165-2167, Oct. 2006.
- 09/06 Lanlan Gu, Wei Jiang, **Xiaonan Chen**, and Ray T. Chen, *Silicon Photonic Crystal Waveguide Modulators*, International Conference on Group IV Photonics 2006, Ottawa, Canada (invited).

- 04/06 Wei Jiang, Li Wang, **Xiaonan Chen**, Yongqiang Jiang, Lanlan Gu, and Ray T. Chen, *Superprism effect: physics, modelling, and device fabrication*, Integrated Photonics Research and Applications (IPRA) Topical Meeting/ Nanophotonics (NANO) Topical Meeting 2006, Uncasville, CT.
- 05/05 Yongqiang Jiang, Wei Jiang, **Xiaonan Chen**, Lanlan Gu, Brie Howley, and Ray T. Chen, *Slow photon generation on silicon nano-photonic crystal waveguides and applications*, IEEE International Workshop on VLSI Design and Video Technology, May 2005 (invited).
- 04/05 Yongqiang Jiang, Wei Jiang, **Xiaonan Chen**, Lanlan Gu, Brie Howley, and Ray T. Chen, *Nano-photonic crystal waveguides for ultra-compact tunable true time delay lines*, Proc. SPIE Photonic West 2005, San Jose, CA.
- 10/06 Yongqiang Jiang, Wei Jiang, Lanlan Gu, **Xiaonan Chen**, and Chen, R. T., *80-micron Interaction Length Silicon Nano-Photonic Crystal Waveguide Modulator*, Asia Optical Fiber Communication & Optoelectronic Exposition (AOE) Conference 2006, Shenzhen, China.
- 10/06 Lanlan Gu, Wei Jiang, Yongqiang Jiang, **Xiaonan Chen**, Jinha Kim, and Ray T. Chen, *Silicon modulators Based on Photonic-Crystal Waveguides*, Asian-Pacific Communication (APOC) Conference 2006, GwangJu, Korea (invited).
- 04/06 Lanlan Gu, Wei Jiang, Yongqiang Jiang, **Xiaonan Chen**, and Ray T. Chen, *Photonic-crystal-waveguide based Si Mach-Zehnder modulator*, Integrated Photonics Research and Applications (IPRA) Topical Meeting/ Nanophotonics (NANO) Topical Meeting 2006, Uncasville, CT.
- 03/06 Lanlan Gu, Yongqiang Jiang, Wei Jiang, **Xiaonan Chen**, and Ray T. Chen, *Silicon-on-insulator-based photonic-crystal Mach-Zehnder interferometers*, Proc. SPIE Photonic West 2006, San Jose, CA.
- 12/05 Yongqiang Jiang, Zhong Shi, Brie Howley, **Xiaonan Chen**, Maggie Y. Chen, and Ray T. Chen, *Delay-time-enhanced photonic crystal fiber array for wireless communications using two-dimensional X-band phased-array antennas*, Optical Engineering, vol. 44, no. 125001, Dec. 2005.
- 11/05 Yongqiang Jiang, Wei Jiang, Lanlan Gu, **Xiaonan Chen**, and Ray T. Chen, *80-micron interaction length silicon photonic crystal waveguide modulator*, Applied Physics Letters, vol. 87, no. 221105, Nov. 2005.
- 10/05 Wei Jiang, Yongqiang Jiang, Lanlan Gu, **Xiaonan Chen**, and Ray T. Chen, *Photonic crystal devices for wavelength division multiplexing and optical modulation*, Proc. SPIE Photonic East 2005, Boston, MA (invited).

- 03/06 Wei Jiang, Yongqiang Jiang, Lanlan Gu, Li Wang, **Xiaonan Chen**, and Ray T. Chen, *Silicon and polymer nanophotonic devices based on photonic crystals*, Proc. SPIE Photonic West 2006, San Jose, CA (invited).
- 03/06 Yongqiang Jiang, Tao Ling, Lanlan Gu, Wei Jiang, **Xiaonan Chen**, and Ray T. Chen, *Highly dispersive photonic crystal waveguides and their applications in optical modulators and true-time delay lines*, Proc. SPIE Photonic West 2006, San Jose, CA.

Permanent Address: Bldg.39 Unit.7 Rm.502  
Shijingshan Dist. Laoshanxili  
Beijing, China  
100039

This dissertation was typed by the author.